UNIVERSITY OF CALIFORNIA

Los Angeles

Foreshock Transients: Their Characteristics and Effects on Particle Acceleration

A dissertation submitted in partial satisfaction of the requirements for the degree Doctor of Philosophy in Geophysics and Space Physics

by

Zixu Liu

2018

ABSTRACT OF THE DISSERTATION

Foreshock Transients: Their Characteristics

and Effects on Particle Acceleration

by

Zixu Liu
Doctor of Philosophy in Geophysics and Space Physics
University of California, Los Angeles, 2018
Professor Vassilis Angelopoulos, Chair

Earth's foreshock is filled with particles that have been reflected at the bow shock and are streaming away from it. Interaction of these particles with solar wind particles and discontinuities within this region can cause foreshock transients to form. Two types of foreshock transients, foreshock bubbles (FBs) and hot flow anomalies (HFAs), are especially important because they encompass a sizeable (one to several earth radii) core of hot ions which briefly repel the solar wind and can cause intense disturbances in the magnetosphere-ionosphere system. In the highly dynamic environment they create, particles can be potentially accelerated to high energies. In this thesis I investigate the formation, properties, and potential for acceleration of these two types of foreshock transients. As foreshock bubbles have only recently been discovered and their generation mechanism has not been fully explored I first examine their drivers. I demonstrate that in addition to solar wind rotational discontinuities, tangential discontinuities can also drive foreshock bubbles; therefore, the conditions for their formation are more common than previously thought. I show that fast solar wind and weak interplanetary magnetic field conditions statistically favor formation of foreshock bubbles and hot flow anomalies. Next, using multi-point observations I elucidate the spatial structure and evolution of FBs. I also provide definitive evidence that FBs can form their own foreshock, when their sunward expansion speed is fast enough, creating the conditions for further particle acceleration there. To investigate the role of

the two most important types of foreshock transients (FBs and HFAs) for particle acceleration, I first employ statistical studies. I show that these types of foreshock transients almost always accelerate electrons, and often also accelerate ions. The solar wind speed is positively correlated with all measures of particle acceleration, thus plays an important role. To further understand the nature of this acceleration, I use case studies along with test particle simulations and hybrid simulations. I show that Fermi acceleration and betatron acceleration are two important acceleration mechanisms for electrons. Ions, on the other hand, can be accelerated by reflection at the earthward-moving boundary of the foreshock transients and can leak into the ambient foreshock region upstream due to their large gyroradii, thus obscuring detection of ion energization in the core when compared to its surroundings. Foreshock transients therefore play an important role in particle acceleration in shock environments. They accelerate particles in their cores, and provide an energetic particle source for parent shock acceleration, thereby increasing the acceleration efficiency of quasi-parallel shocks.

The dissertation of Zixu Liu is approved.

Christopher T. Russell

Marco CM. Velli

Lawrence R. Lyons

Heli Johanna Hietala

Vassilis Angelopoulos, Committee Chair

University of California, Los Angeles

2018

Contents

Supplementary Material

Movie S1. Movie of our 3-D hybrid simulation of a foreshock bubble driven by a rotational discontinuity in the XY plane (at Z = 0 R_E) and XZ plane (at Y = 8 R_E). Color indicates normalized density. The rotational discontinuity is indicated by a vertical line.

Movie S2. 1-D cut at Y = 8 R_E and Z = 0 R_E in our hybrid simulation. From top to bottom: magnetic field, electric field, ion velocity, ion density, and ion temperature.

Movie S3. The movie of field line tracing in our 3-D hybrid simulation in the XY plane.

Movie S4. The movie of particle tracing in our 3-D hybrid simulation. The format of left panel is similar to Figure 6.4b. Blue dot is the traced ion. The right panel indicates the energy of traced ion as a function of time. (a) and (b) correspond to ion-1 and ion-2 in Figure 6.6, respectively. Note that this movie is a different run with smaller solar wind speed than Movie S1 – S3.

Preface

I thank the THEMIS software team and NASA's Coordinated Data Analysis Web (http://cdaweb.gsfc.nasa.gov/) for their analysis tools and data access. The THEMIS data and THEMIS software (SPEDAS) are available at http://themis.ssl.berkeley.edu. The work leading to this thesis was supported by NASA contract NAS5-02099.

I am deeply grateful to my supervisor, Prof. Vassilis Angelopoulos, who recruited me into the THEMIS group and has guided me for five years. He taught me many skills, including data analysis, paper writing, presentation, and more importantly, how to do research. I also thank Dr. Drew Turner and Dr. Heli Hietala for leading me to my specific research area, foreshock transients and shocks.

I thank my co-authors for their contributions to my thesis, especially Dr. San Lu, who also taught me much about simulations. I appreciate the help and support from our THEMIS group members. I thank Dr. Hairong Lai and Dr. Xin An for the inspired discussions. I thank Judith Hohl for editing my thesis.

Last but not least, I thank my family who emotionally and financially supported my study at the University of California, Los Angeles.

VITA

Education

Department of Earth, Planetary, and Space Sciences, University of California, Los Angeles

PHD candidate 09/2013-present

School of Earth and Space Sciences, Peking University

B.S in Space Science and Technology 09/2009-07/2013

Awards and Honors

Harold and Mayla Sullwold Scholarship at EPSS, UCLA in 2017

Outstanding Poster Award at the international Geospace Environment Modeling conference in 2017

Outstanding Student Paper Award at American Geophysical Union Fall Meeting in 2016

Eugene B. Waggoner Scholarship at EPSS, UCLA in 2016

Outstanding Poster Award at the international Geospace Environment Modeling conference in 2016

Publications

Liu, T. Z., Lu, S., Angelopoulos, V., Lin, Y., & Wang, X. Y. (2018). Ion acceleration inside foreshock transients. Journal of Geophysical Research: Space Physics, 122. https://doi.org/10.1002/2017JA024838

Liu, T. Z., S. Lu, V. Angelopoulos, H. Hietala, and L. B. Wilson III (2017), Fermi acceleration of electrons inside foreshock transient cores, J. Geophys. Res. Space Physics, 122, doi:10.1002/2017JA024480.

Liu, T. Z., V. Angelopoulos, and H. Hietala (2017), Energetic ion leakage from foreshock transient cores, J. Geophys. Res. Space Physics, 122, doi:10.1002/2017JA024257.

Liu, T. Z., V. Angelopoulos, H. Hietala, and L. B. Wilson III (2017), Statistical study of particle acceleration in the core of foreshock transients, J. Geophys. Res. Space Physics, 122, doi:10.1002/2017JA024043. **Editor's Highlight**

Wang, C.-P., R. Thorne, **T. Z. Liu**, et al. (2017), A multispacecraft event study of Pc5 ultralow-frequency waves in the magnetosphere and their external drivers, J. Geophys. Res. Space Physics, 122, 5132–5147, doi:10.1002/2016JA023610.

Liu, T. Z., D. L. Turner, V. Angelopoulos, and N. Omidi (2016), Multipoint observations of the structure and evolution of foreshock bubbles and their relation to hot flow anomalies, J. Geophys. Res. Space Physics, 121, doi:10.1002/2016JA022461.

Liu, T. Z., H. Hietala, V. Angelopoulos, and D. L. Turner (2016), Observations of a new foreshock region upstream of a foreshock bubble's shock, Geophys. Res. Lett., 43, doi:10.1002/2016GL068984. **Geophys. Res. Lett. Cover Image**

Liu, Z., D. L. Turner, V. Angelopoulos, and N. Omidi (2015), THEMIS observations of tangential discontinuity-driven foreshock bubbles, Geophys. Res. Lett., 42, doi:10.1002/2015GL065842.

Liu, Z.-X., J.-S. He, and L.-M. Yan (2014), Observations of counter-propagating Alfvénic and compressive fluctuations in the chromosphere, Res. Astron. Astrophys. 14, 3, doi: 10.1088/1674-4527/14/3/004

Invited Presentations

European Geosciences Union General Assembly **04/2018**

Properties and evolution of foreshock bubbles

Fundamental Physical Processes in Solar-Terrestrial Research and Their Relevance to Planetary Physics **01/2018**

Fermi acceleration of electrons inside foreshock transient cores

A. Introduction

When the supersonic solar wind encounters Earth's magnetic field, it cannot penetrate this barrier, but instead has to slow down and move around it. Thus, the Earth's bow shock forms to decelerate the solar wind from supersonic to subsonic speeds. Behind it, the solar wind density, temperature, and field strength increase and the solar wind plasma manages to flow around the magnetospheric obstacle. Because the bow shock is curved, the angle between the upstream interplanetary magnetic field (IMF) and the bow shock normal, θ_{BN}, varies. This angle controls the nature of solar wind interaction with the shock itself, as the foreshock region is formed on upstream field lines that are pointed straight into the shock. The bow shock can thus be separated into two regions: quasi-parallel (θ_{BN}< 45°) and quasi-perpendicular (θ_{BN}> 45°). Because of the foreshock upstream of it, the quasi-parallel region is much more dynamic than the quasi-perpendicular region. The foreshock is filled with backstreaming particles [e.g., Eastwood et al., 2005] that could originate from magnetospheric leakage or solar wind reflection [e.g., Burgess et al., 2012]. Foreshock ions are reflected by two mechanisms: specular reflection and adiabatic reflection. Specular reflection, a reversal of the normal component of the incident beam velocity in the shock rest frame, can result in gyrophase-bunched distributions, as previously observed [e.g., Gosling et al., 1982; Fuselier, 1995]. Adiabatic reflection, a reversal of the field-aligned beam velocity in the de Hoffmann-Teller frame conserving the first adiabatic invariant [Sonnerup, 1969], can result in beam speed increase through shock drift acceleration, as also observed [e.g., Meziane et al., 1999].

In shock drift acceleration, magnetic drift caused by a field strength increase across the shock has the same direction as the convection electric field (in the normal incidence frame)

[e.g., Burgess, 1987]. A larger θ_{Bn} causes a higher reflected beam speed, so quasi-perpendicular shocks can accelerate particles more effectively than quasi-parallel shocks. In another shock acceleration mechanism, diffusive shock acceleration [e.g., Krymsky, 1977; Forman and Morfill, 1979], spatial diffusion allows particles to pass through the shock repeatedly and experience systematic acceleration due to converging flow; diffusion in momentum space can also give rise to stochastic acceleration [e.g., Lee et al., 2012].

Shock acceleration is ubiquitous and important, as it is thought to be the main source of energetic particles in the universe [e.g., Lee et al., 2012; Raymond et al., 2012]. High Mach number shocks related to supernova remnants are considered to be the main source of cosmic rays [Hess, 1912; Helder et al., 2012]. In our own solar system, gradual solar energetic particle events could be caused by diffusive shock acceleration [Lee et al., 2012]. As quasi-perpendicular shocks have a higher acceleration rate, energetic particles are generally observed in the quasi-perpendicular region of Earth's bow shock and of coronal mass ejection (CME)-driven shocks [Burgess et al., 2012; Lee et al., 2012]. In practice, however, very few particles can be emplaced (injected) into the diffusive acceleration region to undergo further acceleration, especially at quasi-perpendicular shocks, because the minimum particle energy required for this process to take hold is quite large, and ambient particle fluxes at such energies are very low [Lee et al., 2012]. The source of particles participating in quasi-perpendicular shock acceleration is still unknown (it is called the "injection problem" [Jokipii, 1987]). In addition, recent observations at Saturn by Masters et al. [2013] show that at high Mach numbers (similar to those at young supernova remnant shocks), quasi-parallel shocks accelerate particles more effectively than quasi-perpendicular ones, which is inconsistent with shock acceleration theory. To solve such shock acceleration problems, more detailed understanding of what happens upstream of shocks,

which cannot be gained from afar, is required.

Upstream of planetary shocks, foreshock ions can interact with solar wind ions and generate low-frequency waves through multiple processes [e.g., Wilson, 2016]. When a foreshock ion beam is cold, tenuous, and fast, it can generate whistler mode waves through the right-hand resonant instability [Winske and Leroy, 1984]. When it is hot and slow, it can generate Alfvenic waves through the left-hand resonant instability [e.g., Gary, 1991]. These waves can further steepen and interact with each other, resulting in dynamic structures referred to as foreshock transients, such as short large-amplitude magnetic structures (SLAMS) [e.g., Schwartz et al., 1992] and foreshock cavitons [e.g., Blanco-Cano et al., 2011].

Short large-amplitude magnetic structures are magnetic pulsations with a duration 5 – 20 s and an amplitude a factor of 2 – 3 or more above the ambient background field [e.g., Schwartz et al., 1992]. In observations, short large-amplitude magnetic structures have all the polarization characteristics of ULF waves, and have plasma interior to them moderately heated and deflected [e.g., Schwartz et al., 1992]. The formation mechanism of short large-amplitude magnetic structures, however, is still not fully resolved (see review by Wilson [2016]).

Foreshock cavitons, another type of foreshock transients, are characterized by a core with large depletion in density and field strength surrounded by compressional boundaries with enhanced density and field strength [e.g., Blanco-Cano et al., 2011]. The scale of foreshock cavitons are ~ 1 R_E. Foreshock cavitons are always surrounded by large amplitude ULF waves. Two types of waves, the weakly compressive waves and oblique propagating linearly polarized waves, are responsible for the formation of foreshock cavitons [e.g., Blanco-Cano et al., 2011].

Foreshock transients can also form from kinetic effects of foreshock ions. For example, foreshock cavities [e.g., Sibeck et al., 2002], another type of foreshock transients, form when a local foreshock region is bounded by field lines that are not connected to the bow shock. Higher thermal pressure from foreshock ions results in expansion of the hot foreshock region to the surrounding pristine solar wind, forming a hot, tenuous core with two compressional boundaries. Thus, different to foreshock cavitons, foreshock cavities are not associated with ULF waves and have suprathermal ions inside their cores.

Additionally, when solar wind discontinuities interact with foreshock ions, two classes of large foreshock transients, hot flow anomalies (HFAs) [e.g., Schwartz et al., 1985] and foreshock bubbles (FBs) [Omidi et al., 2010; Turner et al., 2013], can form. As introduced later, because they have larger scales and are more associated with the kinetic effects of foreshock ions than short large-amplitude magnetic structures, foreshock cavitons, and foreshock cavities, they can disturb the magnetosphere more significantly and potentially accelerate particles. Therefore, in this thesis I will mainly study foreshock bubbles and hot flow anomalies.

Hot flow anomalies have been studied for more than 30 years [e.g., Schwartz et al., 1985; Zhang et al., 2010]. They form when a tangential discontinuity (TD) slowly crosses the surface of the quasi-parallel bow shock with the convection electric field pointing towards the tangential discontinuity on one or on both sides of it, such that it can trap foreshock ions around it [Schwartz et al., 2000]. Characterized by a hot, tenuous core and plasma deflection surrounded by one or two compressional boundaries, hot flow anomalies move along the bow shock surface together with the intersection of that surface with the driver tangential discontinuity. During that motion they typically expand to 1 – 3 R_E [e.g., Facskó et al., 2009]. Spontaneous hot flow anomalies (SHFAs) [Omidi et al., 2013; Zhang et al., 2013] have similar characteristics except

that they form spontaneously (in the absence of a driver solar wind discontinuity) when foreshock cavitons emerging in the foreshock interact with the bow shock.

The other significant type of foreshock transients, foreshock bubbles, were identified in hybrid simulations by Omidi et al. [2010] and were first observed by Turner et al. [2013]. In simulations, a foreshock bubble forms when foreshock ions pass through a solar wind rotational discontinuity (RD). The foreshock ion backstreaming motions are interrupted by the rotational discontinuity; this enhances the thermal pressure locally and pushes the surrounding cold solar wind plasma and field lines back towards the Sun. Because the sunward expansion is typically faster than the local fast wave, a shock (the "foreshock bubble shock") can form upstream of a hot, tenuous core, and a sharp plasma deflection can accompany it. Foreshock bubbles can grow to 5 – 10 R_E in linear dimension due to their very fast expansion [Omidi et al., 2010; Turner et al., 2013]. The major differences between foreshock bubbles and hot flow anomalies are that foreshock bubbles form only upstream of a discontinuity and expand very fast only in the sunward direction, resulting in very large scale and a shock, whereas hot flow anomalies typically expand slowly in two directions resulting in smaller scale (1 – 3 R_E in linear dimension) and two compressional boundaries (not necessarily shocks, due to their slow expansion) on both sides of their core. In extreme cases, however, the two phenomena are difficult to distinguish based on their local observational characteristics alone. Future studies are needed to distinguish them based on their formation mechanisms, their upstream conditions, and their temporal evolution.

Foreshock cavities, foreshock cavitons, hot flow anomalies, spontaneous hot flow anomalies, and foreshock bubbles have a similar characteristic – a low-density, low field-strength core that can result in dynamic pressure perturbations. When these foreshock transients

connect to the bow shock, they disturb the bow shock surface and the magnetosheath. Such disturbances then propagate into the magnetosphere, causing ULF waves [e.g., Sibeck et al., 1999; Turner et al., 2011]. Foreshock bubbles, hot flow anomalies, and spontaneous hot flow anomalies cause especially significant effects, because the solar wind is deflected inside their cores, resulting in stronger dynamic pressure perturbations [e.g., Archer et al., 2014; Archer et al., 2015]. Because of their large size (5 – 10 R_E), foreshock bubbles can disturb the bow shock and magnetosphere more globally [Archer et al., 2015].

In addition to their perturbations on the magnetosphere, foreshock bubbles can generate energetic particles, indicating that they have the potential for particle acceleration [Turner et al., 2013]. Simulations by Omidi et al. [2010] also suggest that foreshock bubbles could accelerate particles through Fermi acceleration. This implies that foreshock bubbles might provide a particle source for parent shock acceleration and increase the particle acceleration efficiency at quasi-parallel shocks. Although foreshock bubbles can globally disturb the magnetosphere and could help resolve open questions regarding shock acceleration, only a few studies have explored their properties because of their very recent identification. With its multiple spacecraft frequently straddling Earth's foreshock and pristine solar wind and its comprehensive instrumentation, NASA's Time History of Events and Macroscale Interactions During Substorms (THEMIS) mission, which was launched in 2007, provides a very good opportunity to observe these phenomena. We use THEMIS observations to further investigate foreshock bubbles and other foreshock transients to understand their characteristics and potential contributions to particle acceleration.

We start by exploring their formation process. In simulations [Omidi et al., 2010], foreshock bubbles form from the interaction between a rotational discontinuity and foreshock

ions. Using THEMIS observations, I will show that foreshock bubble formation is not caused only by rotational discontinuities but that tangential discontinuities can also interact with foreshock ions to form foreshock bubbles. I will also present a model to explain this formation process. Then, using a statistical study, I will reveal the solar wind conditions that favor formation of foreshock transients (mainly foreshock bubbles, hot flow anomalies, and spontaneous hot flow anomalies), which share similar characteristics: a hot, tenuous core with plasma deflection surrounded by one or two compressional boundaries (Chapter 1).

Previous observations of foreshock bubbles [Turner et al., 2013] made by single spacecraft provided limited information on spatial structure and especially evolution. In 2007, all five THEMIS spacecraft, which were in a string-of-pearls configuration, visited the foreshock repeatedly, observing foreshock bubbles from five nearby vantage points at spatial separations of a few Earth radii, commensurate with foreshock bubble sizes. Using such five-point observations, I will describe the curved shape of foreshock bubbles and how they evolve, including their expansion and plasma parameter variations. I will show that our observational results are consistent with those from hybrid simulations (Chapter 2).

In simulations [Omidi et al., 2010], a foreshock bubble shock can reflect solar wind particles and form a new foreshock, but observational evidence is needed. Using THEMIS observations, I will present definitive evidence of the formation of such a new foreshock. I will show that particles in the new foreshock are accelerated at the foreshock bubble shock through shock drift acceleration and then convect with the foreshock bubble towards the bow shock. This implies that foreshock bubbles could play an important role in shock acceleration, such as providing a particle source for diffusive shock acceleration at the parent shock (Chapter 3).

Because foreshock bubbles can accelerate particles and could affect acceleration at their parent shock, it is important to learn whether other foreshock transients with similar characteristics (e.g., hot flow anomalies and spontaneous hot flow anomalies) can also accelerate particles and play a role in shock acceleration. Thus, I will present a statistical study to reveal whether these foreshock transients can accelerate particles inside their cores and, if so, how common this acceleration is. As we will see from these statistics, foreshock transients can indeed efficiently accelerate both electrons and ions inside their cores. I will also present that solar wind speed is critical to the particle acceleration energy (Chapter 4) in an effort to understand the acceleration mechanism.

To further explore the particle acceleration mechanism at and around foreshock transients, I will use THEMIS observations hand-in-hand with test particle simulations and hybrid simulations. Constructing simple observationally-motivated acceleration models, which are then tested by simulations and further checked against the data, I will reveal two electron acceleration mechanisms, Fermi acceleration and betatron acceleration (Chapter 5). Using a similar approach, I will also show a potential ion acceleration mechanism, one bounce between the converging foreshock transient boundary and the bow shock (Chapter 6). Based on these results, I will discuss the possible role of foreshock transients in the shock acceleration process in the Discussion section.

B. Part I. Formation, properties, and impacts of FBs

Although foreshock bubbles can globally disturb the magnetosphere and potentially accelerate particles, very little is known about them. In Part I, we will focus on understanding foreshock bubbles, including their formation, properties, and impacts. In Chapter 1, I will present a new type of driver discontinuity of foreshock bubbles. I will also use statistical study to reveal conditions that favor formation of foreshock transients, mainly foreshock bubbles, hot flow anomalies, and spontaneous hot flow anomalies. In Chapter 2, I will use multi-spacecraft observations to reveal the spatial structure and evolution of foreshock bubbles. In Chapter 3, from case study I will show that foreshock bubbles can accelerate particles at foreshock bubble shocks, implying that foreshock bubbles not only disturb the bow shock surface but also play an important role in shock acceleration.

Chapter 1. Formation of FBs

In simulations [Omidi et al., 2010], a foreshock bubble forms when foreshock ions pass through a rotational discontinuity and are trapped locally. As tangential discontinuities are also common in the solar wind [e.g., Neugebauer et al., 1984], it is necessary to examine whether they could also drive foreshock bubbles. Tangential discontinuities have not previously been considered as foreshock bubble drivers because without a magnetic normal component, foreshock ions cannot directly pass through a tangential discontinuity along field lines. However, given that suprathermal foreshock ions have gyroradii larger than the width of tangential discontinuities, they may gyrate through a tangential discontinuity and generate a foreshock bubble. Therefore, in this chapter I will use THEMIS observations to confirm that a tangential discontinuity can indeed drive a foreshock bubble. In Section 1.1, I will show a sample

observation in detail (another example can be found in Chapter 2). In Section 1.2, I will discuss the possible process whereby solar wind discontinuities trap foreshock ions and form foreshock bubbles; I will compare that to the process leading to the formation of hot flow anomalies. In Section 1.3, using a statistical study I will reveal that faster solar wind speed and lower IMF field strength favor foreshock transient formation. In our statistical study (see event list in Appendix d), ~31% of 247 events are likely foreshock bubbles and the remainder are hot flow anomalies, spontaneous hot flow anomalies, and foreshock cavities. These four types of foreshock transients have very similar characteristics: a hot, tenuous core with plasma deflection surrounded by one or two compressional boundaries.

1.1 Observational example of a TD-driven FB

To identify a tangential discontinuity-driven foreshock bubble, we use TH-C near the bow shock to observe a foreshock bubble (see event list in Appendix d) and TH-B upstream of it to monitor the driver discontinuity (e.g., Figure 1.1d). Using ACE, Wind, and TH-B, we then determine whether the driver discontinuity is a tangential discontinuity. In this section, a detailed example is demonstrated (another example can be found in Chapter 2).

On 19 August 2008 at around 00:20 UT, a discontinuity was observed by ACE (Figure 1.1a, dashed lines). Fifty minutes later, at around 01:11 UT, TH-B observed what was interpreted to be the same discontinuity at X_{GSM}=29.5 R_E (Figure 1.1b, dashed lines). Both observations show that inside the discontinuity, B_x and B_y approached zero. Both components retained the same sign across the discontinuity, and B_z changed from negative to positive. At ACE, there was a small decrease in magnetic field strength across the discontinuity (~0.2 nT, whereas the standard deviation of field strength is ~0.1 nT). After the discontinuity was observed, a temporary ion

thermal pressure increase and an additional temporary magnetic field strength decrease inside a transient structure (B_y decreased and B_x and B_z increased temporarily; see horizontal bar in Figure 1.1a) were observed between 00:21 and 00:22 UT. At TH-B (see its position in Figure 1.1d), the magnetic field strength also decreased across what we interpret as the same discontinuity (vertical dashed lines in Figure 1.1b). Immediately after the discontinuity was observed at around 01:12 UT, another temporary decrease in magnetic field strength was observed, along with a decrease in electron thermal pressure and B_y and an increase in B_x and B_z, corresponding to what we interpret as the transient structure previously observed by ACE (see horizontal bar in Figure 1.1b). The discontinuity normal from the three-spacecraft timing method (ACE, Wind, and TH-B, see Appendix a) using solar wind speed was [0.54, 0.82, -0.15]. In Figures 1.1a and 1.1b, the magnetic field component in the normal direction, B_n, crosses zero within one sigma of magnetic field strength fluctuation and the normal component of velocity, V_n, is almost constant. The normal calculated using the cross-product method at ACE and TH-B assuming a tangential discontinuity indicates directions similar to the normal calculated using the three-spacecraft timing method. The discontinuity cannot be a rotational discontinuity because the magnetic field strength decreases. It cannot be a shock because of the consistency of the normal from time delay analysis with the normal from the cross-product method (note that the normal from the coplanarity method is perpendicular to that from the cross-product method). Because this discontinuity is consistent with tangential discontinuity properties, we identified it as a tangential discontinuity. The thickness of the tangential discontinuity (product of time interval between two dashed lines and V_n) was ~1900 and 2000 km at ACE and TH-B, respectively. At TH-B, the gyroradii of 10 keV foreshock ions with 30° pitch angles were ~2400 km, larger than the tangential discontinuity thickness.

At around 01:14 UT, TH-C, near the bow shock (Figure 1.1d), observed a transient phenomenon with a tenuous, hot core accompanied by significantly deflected plasma flow (Figure 1.1c). No compressional boundary was evident on the downstream side. Some extreme hot flow anomalies have only one boundary on the upstream side. According to the coupled model by Thomsen et al. [1988], however, this situation requires that the ratio of bow shock-reflected ion partial density to incident solar wind partial density be larger than 0.66 (in this case, the earthward expansion is slower than the sunward ion bulk velocity in the solar wind frame). In this event the ratio was around 0.2, so if the event were a hot flow anomaly, it should have two boundaries. On the upstream side of the event, there was a shock with a strong sunward component. The size of the transient phenomenon was around 6.0 R_E along the normal direction of the upstream shock, much larger than the expected hot flow anomaly size [Facsko et al., 2009]. Therefore, this phenomenon is consistent with a foreshock bubble, a giant plasma bubble (5 – 10 R_E) with fast expansion only in the sunward direction, resulting in a shock upstream of its hot, tenuous core.

At the foreshock bubble's downstream boundary, observed at around 01:14:30 UT and represented by dashed line in Figure 1.1c, the three magnetic field components approached zero at a clear discontinuity in the field. On both sides of the discontinuity, B_x and B_y retained their sign, and B_z changed from negative to positive, as in the tangential discontinuity observed by ACE and TH-B. The time delay analysis between ACE and TH-C and between TH-B and TH-C was consistent with the calculated orientation of the tangential discontinuity. Thus, the magnetic field structure at the downstream boundary of the foreshock bubble was very likely the tangential discontinuity observed by ACE and TH-B. There was a quasi-parallel foreshock on both sides of tangential discontinuity at TH-C. If this event were a hot flow anomaly, it should be symmetric

with the tangential discontinuity inside the core [Omidi and Sibeck, 2007], but it only developed on the upstream side of the tangential discontinuity. This again proves that this event cannot be a hot flow anomaly. Therefore, we conclude that this was a foreshock bubble driven by a tangential discontinuity. In the next section, we will discuss the formation mechanism of tangential discontinuity-driven foreshock bubbles inspired by the potential formation mechanism of rotational discontinuity-driven foreshock bubbles.

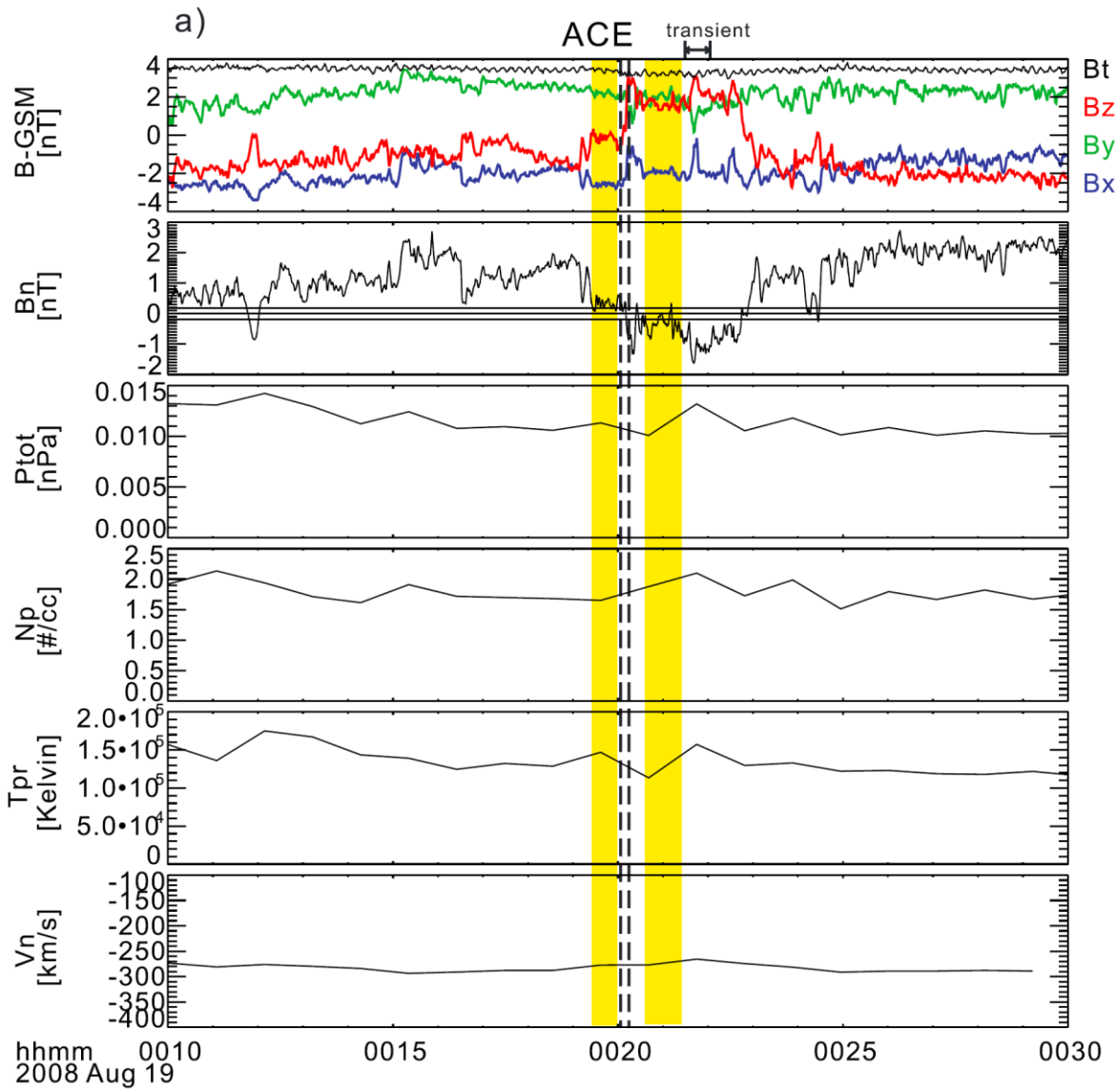

Figure 1.1. *(a) ACE observations of discontinuity. From top to bottom: magnetic field components in GSM coordinates (XYZ in blue, green, and red, respectively); magnetic field normal component (the two horizontal lines above and below zero are error bars corresponding to one standard deviation); total pressure (assuming electron temperature is proportional to ion temperature); ion density; ion temperature; and normal component of velocity. Between two*

dashed lines is the estimated time interval of discontinuity. The time interval used to calculate the cross product is in yellow. The transient is labeled with a horizontal bar.

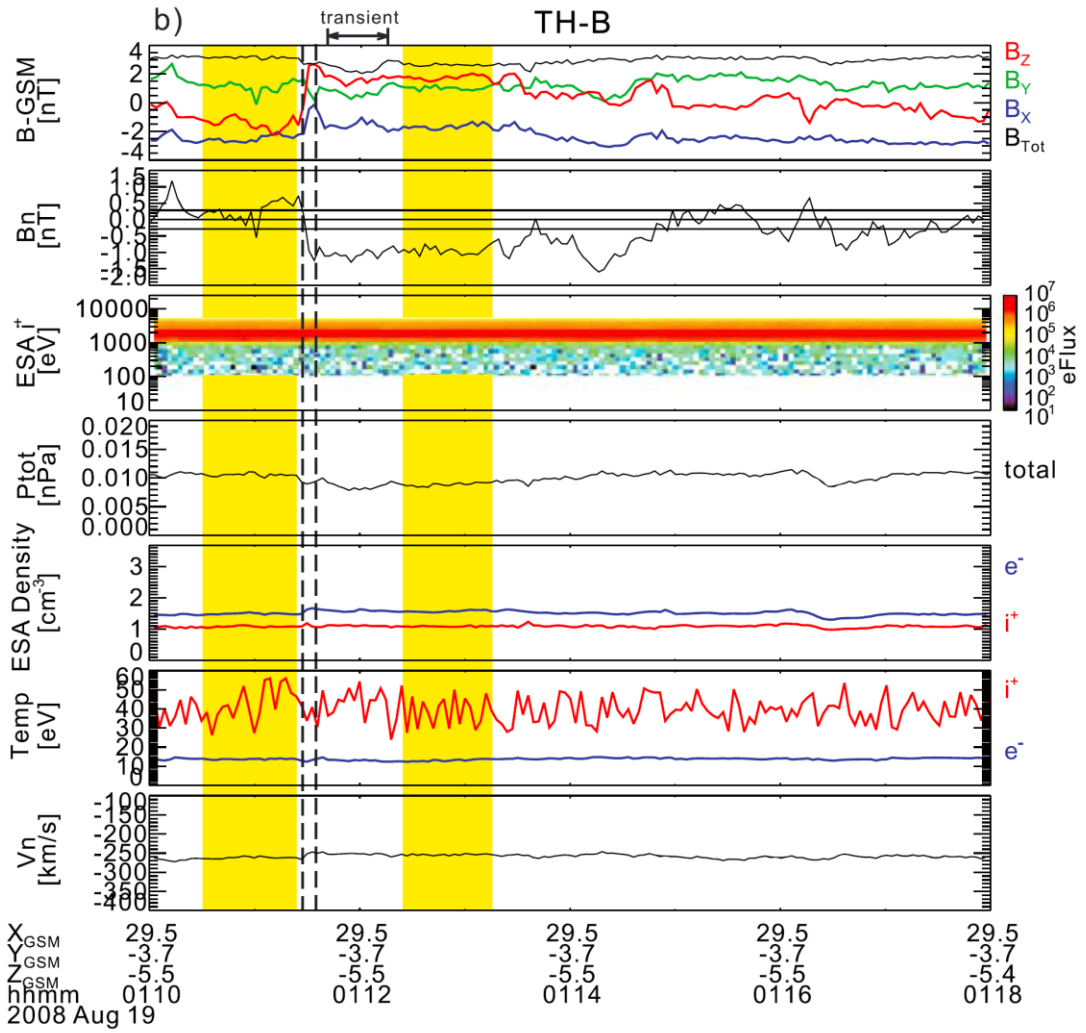

Figure 1.1. *(b) TH-B observations of discontinuity. From top to bottom: magnetic field components in GSM coordinates (XYZ in blue, green, and red, respectively); magnetic field normal component (two horizontal lines above and below zero are error bars); ion energy flux; total pressure (assuming ion temperature is proportional to electron temperature); ion (red) and electron (blue) density; ion (red) and electron (blue) temperature; and normal component of velocity. Between two dashed lines is the estimated time interval of discontinuity. The time interval used to calculate the cross product is in yellow. The transient is labeled with a horizontal bar.*

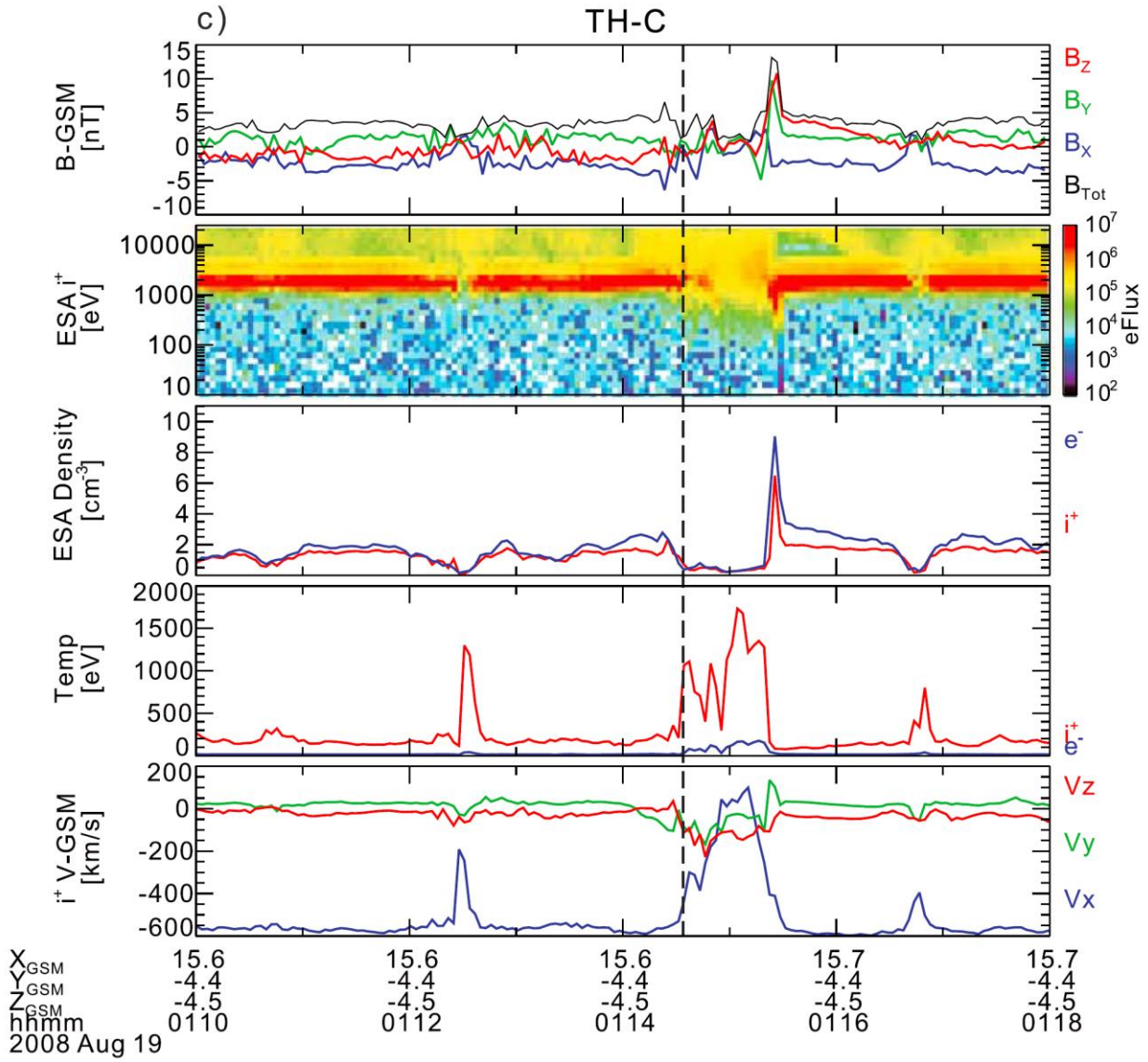

Figure 1.1. *(c) TH-C observations of transient event. From top to bottom: magnetic field components in GSM (XYZ in blue, green, and red, respectively); ion energy flux; ion (red) and electron (blue) density; ion (red) and electron (blue) temperature; and ion velocity components in GSM (XYZ in blue, green, and red, respectively). The dashed line represents discontinuity.*

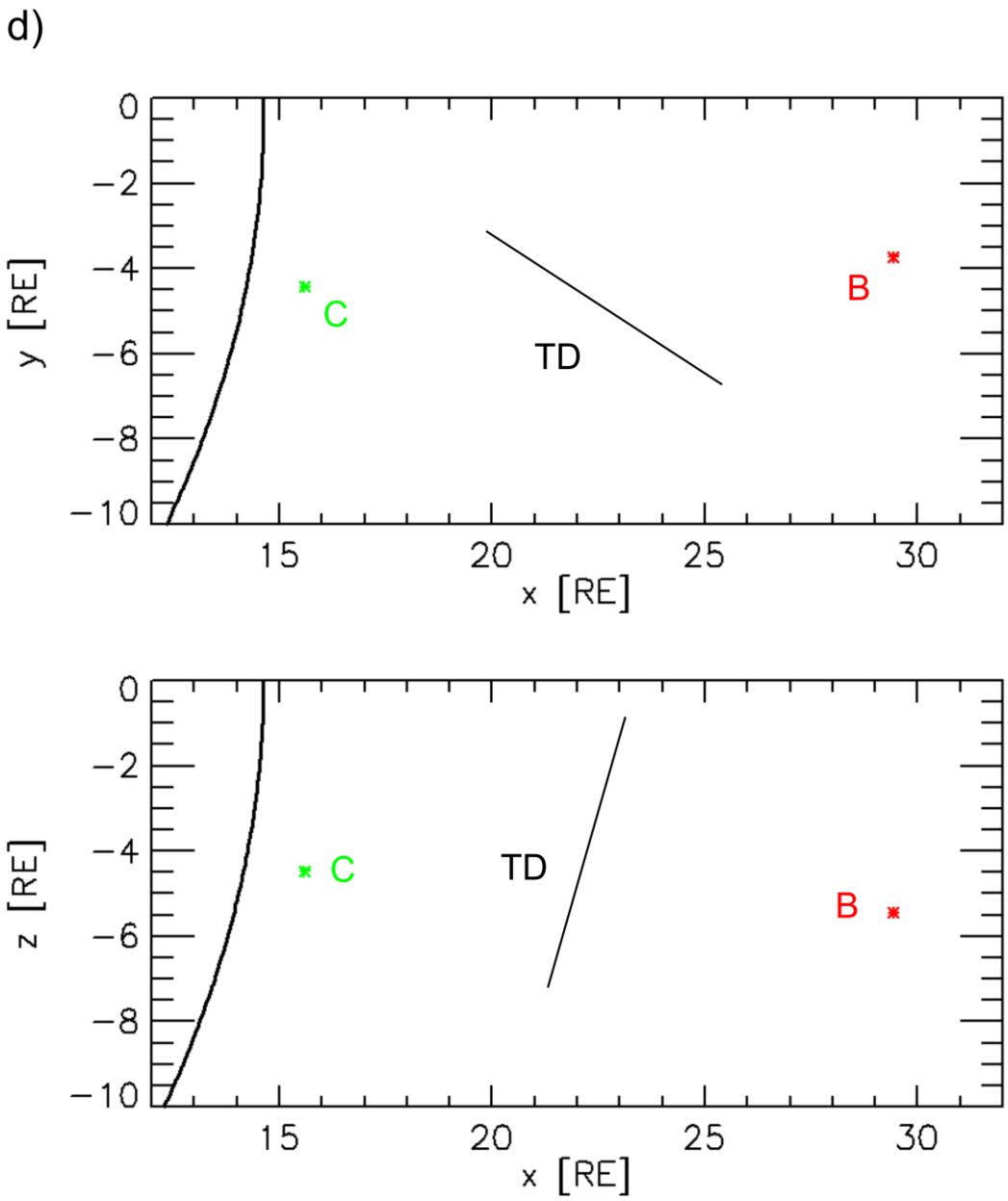

Figure 1.1. *(d) Projection of the TH-B (red) and TH-C (green) positions in the GSM-XY and XZ planes. The orientation of the tangential discontinuity is indicated by solid lines. The curved lines represent the approximate position of the bow shock using the Merka et al. [2005] model.*

1.2 Possible formation mechanism

Although simulations and observations [Omidi et al., 2010; Turner et al., 2013; Liu et al., 2015] show that foreshock bubbles can be driven by either rotational discontinuities or tangential discontinuities, how a discontinuity interacts with foreshock ions to form a foreshock bubble has not been identified. In this section, I will present a possible mechanism for formation of rotational discontinuity-driven foreshock bubbles proposed by Archer et al. [2015]. Inspired by their model, I will discuss a possible mechanism for formation of tangential discontinuity-driven foreshock bubbles.

Archer et al. [2015] discussed the possible process by which a rotational discontinuity concentrates and thermalizes foreshock ions. In the rest frame of a rotational discontinuity where the convection electric field is zero, foreshock ions move along the field lines towards the discontinuity. When these ions cross it, foreshock ion parallel speed should project onto a new magnetic field direction resulting in decreases. As the electric field is zero, foreshock ion energy is conserved. The decreases in parallel speed cause increases in perpendicular speed, meaning that kinetic energy is converted to thermal energy. The decreases in parallel speed can also result in decreases in the speed normal to the rotational discontinuity. As flux is conserved, the decreases in normal speed cause increases in density. Both density and thermal energy increases give increases in thermal pressure that result in expansion and formation of a foreshock bubble.

Now we discuss how a tangential discontinuity traps and thermalizes foreshock ions. The most probable width of a solar wind tangential discontinuity is around 4-8 thermal ion gyroradii [Vasquez et al. 2007]. Because of their thickness and because they do not have a normal

magnetic field component, tangential discontinuities cannot in theory be crossed by thermal ions. In addition, they do not comply with the standard model of foreshock bubble generation, which requires that foreshock ions streaming away from the bow shock along a nearly Sun-Earth aligned IMF interact with a solar wind discontinuity far upstream. Because both sides of tangential discontinuities are parallel to the magnetic field, tangential discontinuities are not expected to intercept upstream particles. Instead, the tangential discontinuity plane is expected to be parallel to the particles' motion.

Suprathermal foreshock ions that are involved in foreshock bubble generation, however, have gyroradii wider than the most probable tangential discontinuity thickness (10 keV foreshock ions with 30° pitch angles have ~10 thermal ion gyroradii). As sketched in Figure 1.2, when a tangential discontinuity intersects a bow shock immediately downstream of and quasi-parallel to it, foreshock ions move along field lines parallel to the plane of the discontinuity and some gyrate through it due to their finite gyroradius (Figure 1.2a, 1.2b). When the upstream IMF has a component along the downstream IMF and a component pointing into the figure (negative Z direction in the coordinate system in Figure 1.2), foreshock ions will be concentrated because both the Lorenz force and the convection electric field force point towards the tangential discontinuity (Figure 1.2b). In the solar wind frame where the convection electric field is zero, with such an IMF configuration (two situations shown in Figure 1.2d, 1.2e), foreshock ions tend to continue their parallel motion and gyromotion while moving to the upstream side. Because of the upstream IMF's negative Z component, part of the original parallel velocity contributes to the gyrovelocity. At the same time, the original (downstream) gyrovelocity vector contributes negative parallel velocity and positive gyrovelocity. Thus, when foreshock ions gyrate through the tangential discontinuity, parallel velocity should decrease, and because of energy

conservation, gyrovelocity should increase. These changes convert some of the ion beam's parallel energy into perpendicular (thermal) energy, resulting in temperature and thermal pressure increases. The hot concentrated foreshock ions will expand and evolve into a foreshock bubble (Figure 1.2c).

Such a formation process of tangential discontinuity-driven foreshock bubbles could also be applicable to hot flow anomalies, but the difference between foreshock bubble and hot flow anomaly formation is unknown. Based on our case studies [Liu et al., 2016b], we found that under similar solar wind conditions, a thinner tangential discontinuity generates a foreshock bubble and a thicker tangential discontinuity generates a hot flow anomaly. Here I discuss the potential role of tangential discontinuity thickness in foreshock bubble formation. Because foreshock bubbles are typically expanding faster than hot flow anomalies, more concentrated and thermalized foreshock ions are required to provide stronger thermal pressure enhancement for foreshock bubble formation. If a tangential discontinuity is thin, more foreshock ions can gyrate through it. Additionally, a thinner tangential discontinuity can also result in larger IMF direction changes within one foreshock ion gyroradius, so more kinetic energy is converted to thermal energy. Thus, a thinner tangential discontinuity could result in more foreshock ions being more thermalized. Future hybrid simulations can be applied to further investigate foreshock bubble and hot flow anomaly formation.

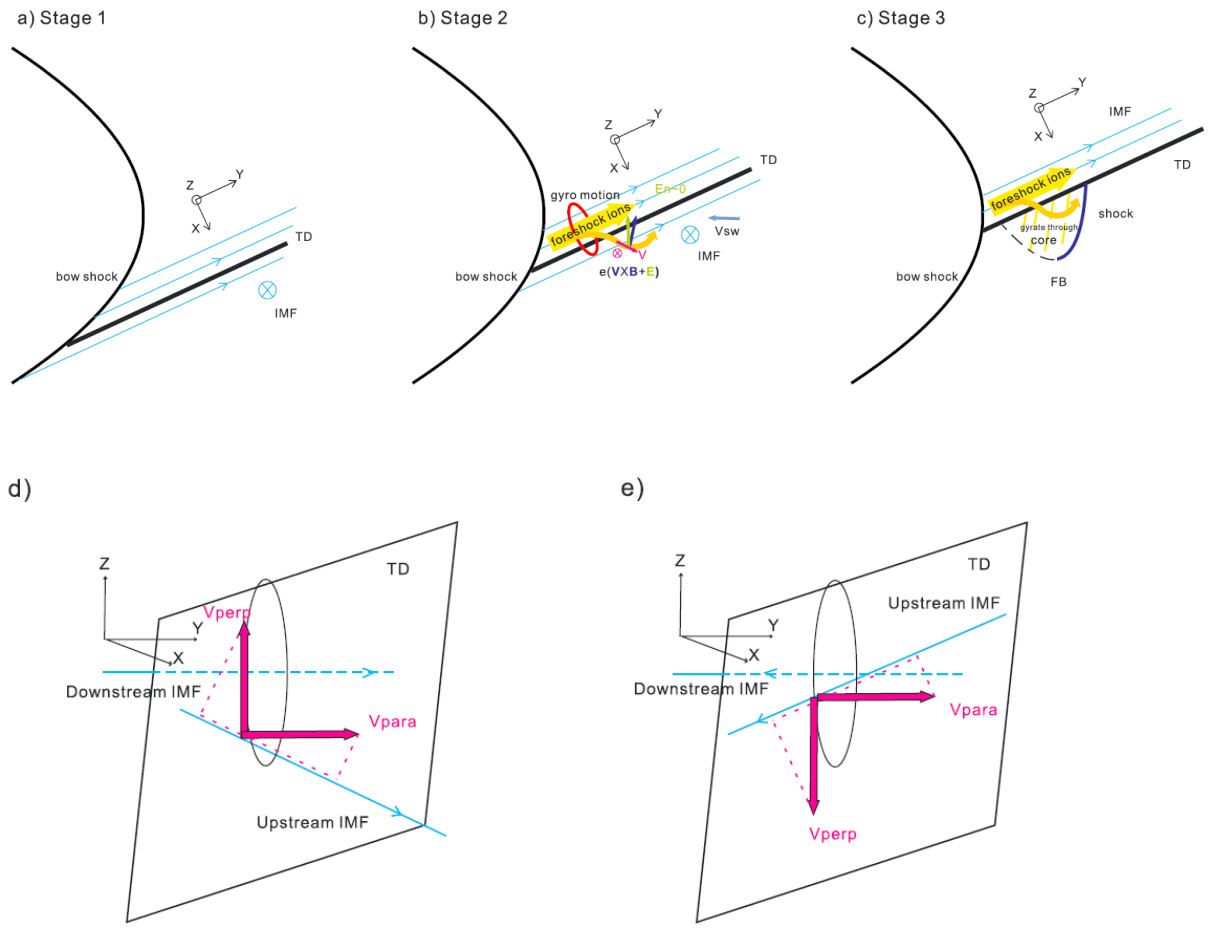

Figure 1.2. *(a)-(c) Our hypothesis of TD-driven foreshock bubble formations. Forces acting on foreshock ions on the upstream side are shown in (b). In this coordinate system, X is normal to the TD and Y is parallel to the downstream IMF in the direction away from Earth. (d) and (e): Changes in parallel velocity and gyro-velocity when foreshock ions pass through TD under two specific IMF configurations (same coordinate system as (a)-(c)): IMF sunward component positive (d) and negative (e). In both cases, foreshock ions are implied to originate in the downstream environment with a sunward component of their parallel velocity and enter the upstream regions. Gyration of the ions in the downstream field (prior to emergence on the upstream side, but at the instant of emergence) is shown in black. For clarity, their parallel (along field) component motion is not depicted.*

1.3 Solar wind conditions

In this section, we determine which solar wind conditions favor foreshock transient formation. By examining TH-B and TH-C observations upstream of the bow shock, we assembled an event list (Appendix d) of 247 foreshock transients with a core associated with foreshock ions to apply a statistical study. From this statistical study, I conclude that lower IMF strength and faster solar wind speed favor formation of foreshock transients. These foreshock transients form due to the kinetic effects of foreshock ions. Faster solar wind speed can result in higher kinetic energy of foreshock ions. Lower IMF strength can likely amplify the kinetic effects.

Our selection criteria were as follows: the density inside the core should drop by more than 30% from that of the background or the pristine solar wind; the event should last longer than 10 s; and plasma deflection (of more than 5%) should be observed. Thus, our events mainly include hot flow anomalies, spontaneous hot flow anomalies, and foreshock bubbles. Some foreshock cavities that have a finite flow deflection may also be included.

We obtain the ambient solar wind characteristics by using 10 min OMNI data from 2008-06-16 to 2008-11-08 and from 2009-06-27 to 2009-09-05, the entire time interval of our database. By comparing Figure 1.3a with 1.3b, and 1.3c with 1.3d, we determine that the relationship between solar wind density and temperature against solar wind speed in our events is almost identical to that in the generic solar wind from the entire database. However, the solar wind magnetic field strength in our events (Figure 1.3e) is almost along the lower bound of the solar wind magnetic field strength measured in the entire time interval of our database (Figure 1.3f). Thus, weak magnetic field strength favors formation of foreshock transients, probably because

foreshock transients can expand more easily and be more dynamic with weaker solar wind field strength.

Looking at the distribution of solar wind speeds (Figure 1.4), we notice that in the ambient solar wind ensemble, 55% of the data are in the slow solar wind category (slower than 400 km/s), and the relative portion of the distribution decreases with increasing solar wind speed (Figure 1.4a). However, the solar wind speed distribution of foreshock transient events shows that only 26% are in the slow solar wind category (Figure 1.4b). If we calculate the ratio of the two distributions (Figure 1.4c), we can see that the probability of foreshock transient formation increases with solar wind speed. We interpret this as evidence that higher solar wind speed can provide more energy for formation of foreshock transients. Therefore, fast solar wind speed is another condition that favors formation of foreshock transients. This result is consistent with findings that hot flow anomalies are favored by fast solar wind [Chu et al., 2017].

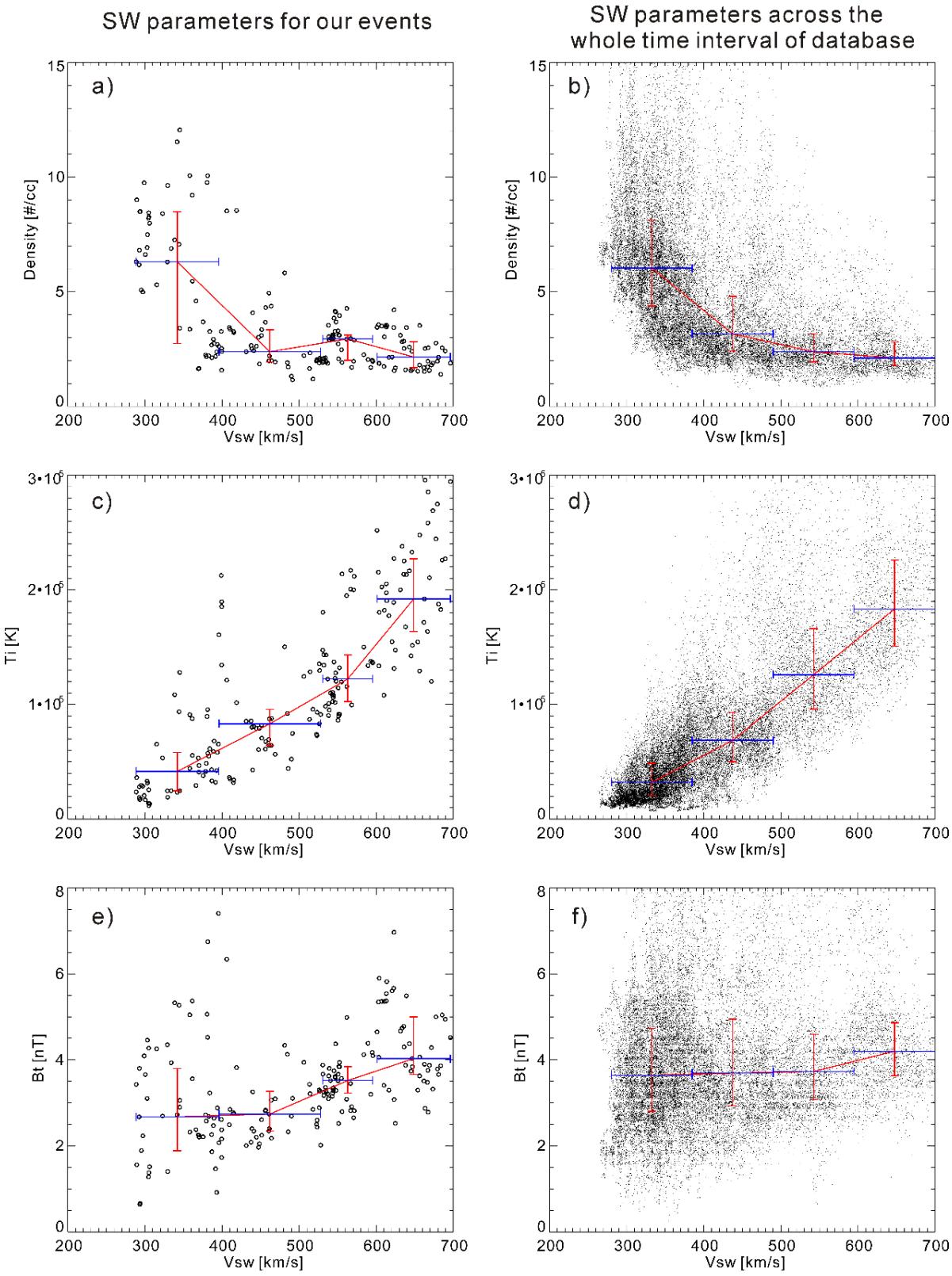
SW parameters for our events
SW parameters across the whole time interval of database
a)
b)
c)
d)
e)
f)
Density [#/cc]
Ti [K]
Bt [nT]
Vsw [km/s]
0
5
10
15
1•10^5
2•10^5
3•10^5
2
4
6
8
200
300
400
500
600
700

Figure 1.3. *Solar wind density, temperature, and field strength versus solar wind speed for events (left column) and in the ambient solar wind in the time period encompassing our database. Red lines are medians, and error bars correspond to quartiles (25% and 75%). Dark blue horizontal bars indicate the data bins in which median and error bars are calculated (for events, each data bin contains an equal number of data; for ambient solar wind, each data bin contains equal solar wind speed interval). The relationships between solar wind density and solar wind speed and between solar wind temperature and solar wind speed in our events are similar to those from the entire time period of the database. But the solar wind magnetic field strength in our events (e) is almost along the lower bound of the solar wind magnetic field from the entire time period of the database (f).*

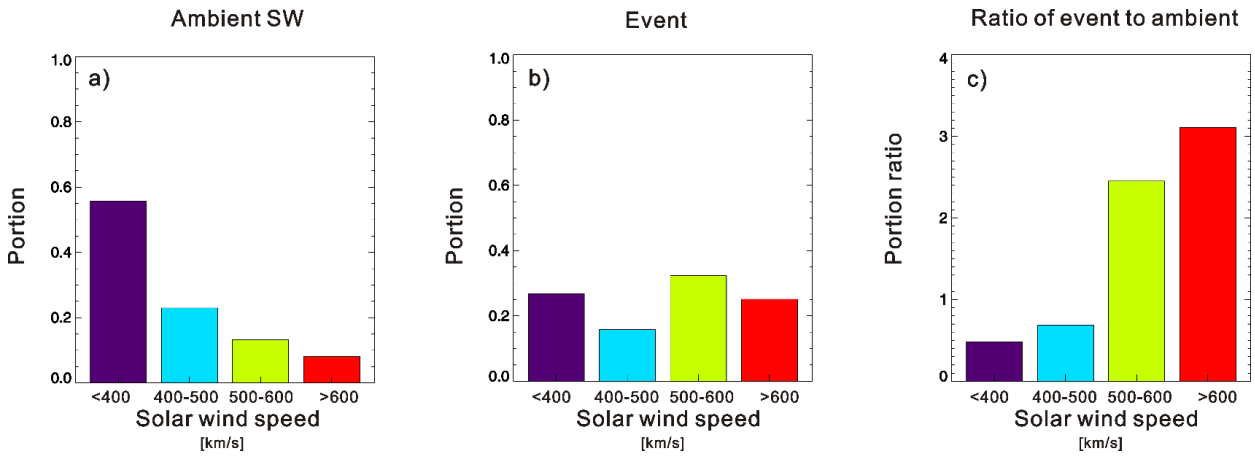

Figure 1.4. *Solar wind speed probability distribution for the ambient solar wind encompassing our database (a) and in our events (b). The distribution ratio for our events to that for the entire database is also shown to facilitate direct comparison (c). The probability of foreshock transient formation increases with solar wind speed.*

1.4 Summary

I presented evidence that tangential discontinuities can and do drive foreshock bubble formation: First, a tangential discontinuity with thickness smaller than the foreshock ion gyroradii interacts with the bow shock under a certain IMF configuration satisfying that the Lorentz force of sunward foreshock ions is pointing towards the discontinuity (Stage 1). Next, when the tangential discontinuity enters the foreshock, foreshock ions start to move along the discontinuity; when the IMF configuration is favorable, some ions can gyrate to the upstream side and be concentrated. These foreshock ions can then start to develop an early-stage foreshock bubble (Stage 2). When enough foreshock ions are in the upstream region, a foreshock bubble can form as observed by TH-C (Stage 3).

I have presented a scenario of tangential discontinuity-driven foreshock bubble formation and supported it with observations (15 events identified, one shown in detail here). The events show that foreshock bubbles can form from interaction between foreshock ions and tangential discontinuities in the solar wind. Future work may further support or modify the proposed model. For example, using global hybrid simulations with driving conditions similar to those in the observations could validate the premise and the physical process of foreshock bubble formation by tangential discontinuities and suggest potential model improvements based on more detailed comparisons between data and theory. Because foreshock bubbles cause global disturbances in Earth's magnetosphere-ionosphere system [Archer et al., 2015] and could occur at astrophysical shocks elsewhere in the universe, it is important to better understand their nature.

I also present a statistical study to investigate the solar wind conditions that favor formation of foreshock bubbles, hot flow anomalies, and spontaneous hot flow anomalies, which have

similar characteristics and could result in similar impacts. We found that faster solar wind speed and lower field strength favor formation of these foreshock transients. Our statistical results do not show clear difference if we only include foreshock bubble-like events (~31% of 247 events).

Chapter 2. Properties of FBs

In previous observations [e.g., Turner et al., 2013; Liu et al., 2015], foreshock bubbles were only observed by single spacecraft, which made it difficult to determine their spatial structure and evolution. These foreshock bubble properties, however, are critical for particle acceleration as, for example, foreshock bubble boundaries could reflect particles and trap them within an evolving foreshock bubble core, thus subjecting them to Fermi or betatron acceleration (which will be discussed later in Chapters 5 and 6). These properties are also important for understanding how foreshock bubbles disturb the bow shock, magnetosheath, and magnetosphere. Therefore, it is important to apply multi-point observations to resolve the spatial structure and evolution of foreshock bubbles.

Observations from the multi-spacecraft mission THEMIS from June to October 2007 can be applied to achieve this goal. During the early "coast phase" period, THEMIS spacecraft were coasting in their orbits without incurring any differential precession, as they were being prepared for their journeys to their final placement for prime mission observations after most of their instruments had been commissioned [Frey et al., 2008]. They were in a "string-of-pearls" configuration at ~15.4 R_E apogee with separations 1 – 5 R_E that allowed them to reside simultaneously in the solar wind for prolonged periods in their orbits.

Thus, all five THEMIS spacecraft had a good opportunity to observe foreshock bubbles from multiple vantage points and thus to be able to establish their scale-size and evolution (see event list in Appendix d, 12 out of 35 events are identified as foreshock bubbles). In this chapter, I will present events observed by all five spacecraft to resolve foreshock bubbles' spatial structure and evolution. In Section 2.1, I will present an overview and identification of one event,

event 1. In Section 2.2, I will show a foreshock bubble's spatial structure and calculate its expansion speed using multiple methods. Then I will reveal the evolution of density and temperature inside its core. In Section 2.3, I will show a second event, event 2, which has similar characteristics to event 1. Last, I will show that the observed spatial structure and evolution are consistent with our hybrid simulation results.

2.1 Overview of event 1

Figure 2.1 shows TH-B observations of a transient phenomenon that we interpret as a foreshock bubble. Figure 2.2a is a pictorial representation of the event with the bow shock and spacecraft locations at the time indicated at the top. Figure 2.2c shows the satellite projections in the XY (Z=0) and XZ (Y=0) planes along with the cross sections of the directional discontinuity (DD) and foreshock bubble shock ("shock") that form in the solar wind and will be discussed later in this section. As evident from these plots, during the period of interest, the five THEMIS spacecraft were on the dayside near the bow shock. Four of them (TH-B, TH-C, TH-D, and TH-E) were very close to each other; TH-A was ~1 R_E behind along their common orbit. The first and last spacecraft to observe the event were TH-B and TH-A, respectively.

The driver discontinuity for this event was observed by Geotail and ACE, which were in the pristine solar wind. The cone-angle and clock-angle changes in the IMF across the driver discontinuity at Geotail, ACE, and TH-B are very similar, as shown in Figure 2.1. The discontinuity normal calculated using three-spacecraft (ACE, Geotail, and TH-B) timing was [0.60, 0.47, -0.64], with uncertainty <10°. Because B_n crossed zero and the change in field strength was 22% (Geotail) and 13% (ACE), this discontinuity could be a tangential discontinuity. Indeed, the normals calculated using the cross-product method at Geotail, ACE,

and TH-B ([0.67, 0.69, -0.24], [0.52, 0.67, -0.53] and [0.42, 0.72, -0.55], respectively) are consistent with the three-spacecraft timing method result. The discontinuity transit time past the THEMIS spacecraft was also coincident with the downstream boundary of the foreshock transient at ~ 05:39 UT to within an ~10% timing uncertainty, suggesting that the driver discontinuity was at the downstream boundary of the foreshock transient observed by THEMIS. By comparing the IMF angles between Geotail, ACE, and TH-B, the direction changes that occurred at the discontinuity in the pristine solar wind also seem to occur at the downstream boundary of this foreshock transient, again supporting the notion that the driver discontinuity was located at the downstream boundary of the foreshock transient.

On the downstream side of the foreshock transient, no compressional boundary was observed. A shock was clearly observed at its upstream boundary, however. At the time, the maximum estimated density ratio of foreshock ions to solar wind ions was less than 0.6. (We calculated the approximate solar wind ion density within the earthward angle range and limited energy range, 1-1.8 keV, of ESA and assumed all remaining density to be reflected ion density.) According to the Thomsen et al. [1988] model, this foreshock transient cannot be a single-boundary hot flow anomaly because that model requires the aforementioned density ratio to be larger than 0.66. The normal of the upstream shock calculated using MVA and the coplanarity method shows a strong x component. The foreshock transient expanded from ~2.3 R_E (TH-B) to ~4.5 R_E (TH-A) along the upstream shock normal direction, larger than the typical size of hot flow anomalies. The region upstream of the discontinuity leading to this foreshock transient was consistent with quasi-perpendicular shock conditions at THEMIS (bow shock θ_{Bn}~55°; the model bow shock in this study is from Merka et al. [2005]), and, indeed, foreshock ions were not observed there. The region downstream, on the other hand, was in the foreshock (bow shock

θ_{Bn}~45°). Because the discontinuity was observed at the downstream boundary of the foreshock transient (~05:39 UT), the foreshock transient formed in the quasi-perpendicular shock region. This is inconsistent with the characteristics of hot flow anomalies (which form in the quasi-parallel region). In summary, this foreshock transient has all the characteristics of a foreshock bubble driven by a tangential discontinuity as described in Chapter 1.

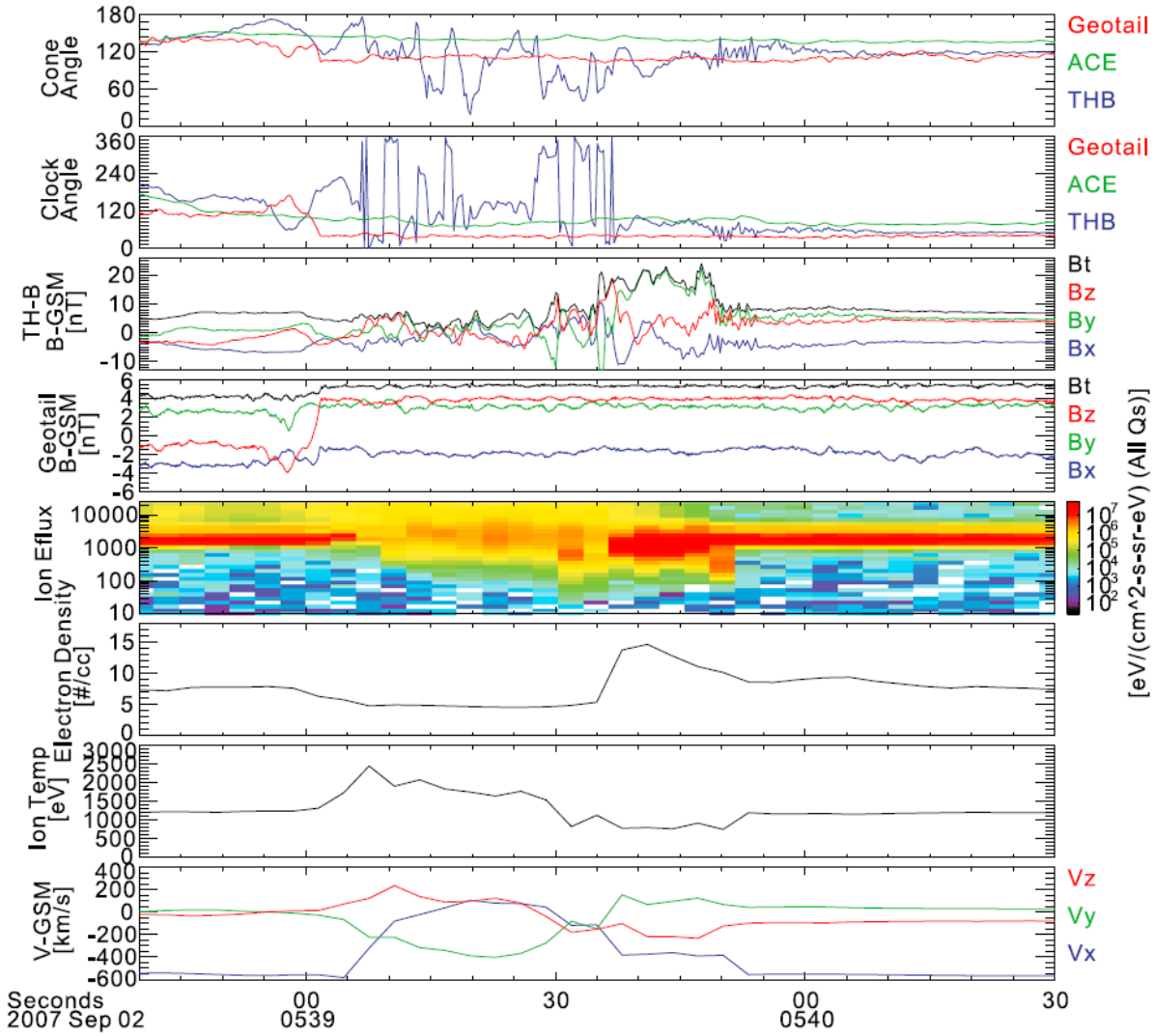

Figure 2.1. *TH-B observations of a foreshock bubble at [12.5, -7.1, -1.3] in GSM and ACE and Geotail ([13.6, 16.5, -9.4]) observations of the driver discontinuity. ACE and Geotail observations are shifted to the same time range as TH-B observations. From top to bottom: ACE (green), Geotail (red), and TH-B (blue) observations of an IMF cone angle (the angle between the IMF vector and the GSM-X direction); ACE (green), Geotail (red), and TH-B (blue) IMF clock angle (the angle between the IMF GSM-YZ component and the GSM-Z axis); TH-B observations of magnetic field components in GSM coordinates (XYZ in blue, green, and red,*

respectively); Geotail observations of magnetic field components in GSM coordinates (XYZ in blue, green, and red, respectively); TH-B observations of ion energy flux; TH-B observations of ion density; TH-B observations of ion temperature; TH-B observations of ion temperature; and TH-B observations of ion bulk velocity in GSM coordinates (XYZ in blue, green, and red, respectively).

2.2 Spatial structure and evolution

With observations from multiple spacecraft, we can calculate the spatial structure of this foreshock bubble (Figure 2.2a). Using Geotail, ACE, and THEMIS data, we obtained the orientation of the discontinuity, which (as discussed) was at the downstream boundary of the core. Then we applied coplanarity methods along with MVA to calculate the normal of the shock upstream of the foreshock bubble listed in Table 2.1. Because TH-A and TH-B were separated by more than 1 R_E (Figure 2.2a, c), they observed different shock normals, which can be used to estimate the radial curvature. Because the time delay between the shock encounters at TH-A and TH-B was 83s, we need to first estimate the position of the shock observed by TH-B after 83s. With the corrected distance between TH-A and TH-B divided by the normal angle difference (10-30°), we estimated the radius of curvature to be 2.5-7.6 R_E, of the same order as the foreshock bubble's size along the shock normal direction.

Next, we calculate the foreshock bubble's expansion speed, assumed to be the upstream shock normal speed in the solar wind frame as there is no compression at the downstream boundary, the driver discontinuity. Therefore, we calculated the shock normal speed at each spacecraft using the conservation of mass [Schwartz, 1998] and continuity of tangential convection electric field method [Smith and Burton, 1988] (Table 2.1). We found that the shock normal speed in the solar wind frame was not constant but decreased from 310 – 400 km/s to 210 – 230 km/s, in the sequence in which the spacecraft observed the shock. There may be at least three reasons for this trend: The first is that the expansion was decelerating, because the expansion energy was exhausted and could not support the initial expansion speed. From TH-B to TH-D (time delay ~25s), the deceleration was 4 km/s^2, whereas from TH-B to TH-A (time

delay ~83s) it was 1.5 km/ s^2. The second is the motion of the foreshock bubble. It could move along the discontinuity surface, as the expansion source, foreshock ions, was moving sunward along the discontinuity (since B_n was close to zero). As a consequence, the part of the shock closer to Earth will have a slower shock normal speed in the solar wind frame (Figure 2.2b, red arrows). As TH-A and TH-D were closer to Earth than TH-B (separation between TH-B and TH-A, D: 7500 km and 2035 km, respectively), they observed less sunward normal direction (even with ~20° uncertainty considered) and slower shock normal speed. This could explain the different shock normal speed as a spatial effect. The third is that the expansion was not necessarily uniform. The expansion was driven by a pressure gradient caused by concentration of foreshock ions on the upstream side of the discontinuity in the MHD point of view. This pressure gradient was not necessarily uniform. All three reasons could play a role in different shock normal speeds in the solar wind frame; more study is needed to determine which one is dominant.

As discussed, the shock normal speed in the solar wind frame may not exactly match the expansion speed caused by foreshock bubble motion. To further corroborate the expansion speed, we investigate it with yet another method. As shown in Figure 2.3a-c, the time interval of the core increased as each spacecraft (TH-B, TH-E, TH-C, TH-D, TH-A) observed the event. So the time interval of the core, Δt, can be expressed as a function of the time delay between TH-B and each subsequent spacecraft, i.e., $\Delta t_i = \Delta t_B\big(1 + \alpha(t_i - t_B)\big)$, where t_i is the time when the spacecraft observed the upstream boundary of the core. The expansion rate α can thus be estimated by using a linear fit, which was ~0.70. Because of the size of the core, $\Delta S_i = V_{sw} \cdot n\Delta t_i = \Delta S_B + V_s(t_i - t_B)$, its expansion speed V_s was $\alpha \boldsymbol{V_{sw}} \cdot \boldsymbol{n}$= 210 km/s at TH-D and 280 km/s at TH-B, where $\boldsymbol{V_{sw}} \cdot \boldsymbol{n}$ is the solar wind speed along the shock normal direction at each

spacecraft. The expansion speed of the core is actually the foreshock bubble sheath flow speed in the solar wind frame; this result is roughly consistent with observed sheath flow speed, confirming our earlier results. Additionally, as shown in Figure 2.3c, the thickness of the foreshock bubble sheath also increases with time because the sheath consists of piled-up plasma that originated at the core (the thickness of the foreshock bubble sheath is proportional to the size of the core). After considering the size increases caused by the foreshock bubble sheath and using the same linear fit method, the overall expansion speed was found to be 230 km/s at TH-D and 300 km/s at TH-B. This result is also roughly consistent with the expansion speed calculated from the shock normal speed. In addition, it confirms that the discontinuity was at the foreshock bubble's downstream boundary and that the foreshock bubble expanded in the upstream direction.

Next, we examine how density and temperature evolve inside the foreshock bubble's core. We first assume that the spatial effect is not important, as the five spacecraft positions are roughly aligned with the discontinuity normal (Figure 2.2c). Because, as mentioned earlier, foreshock ions dominated inside the core, resulting in foreshock bubble expansion, we mainly look at how electron density and temperature changed to study the evolution of the expansion (noting that ESA measurements were well cross-calibrated). While TH-B, the first spacecraft, observed the event, the minimum electron density and maximum electron temperature of the core were 5.0 cm^{-3} and 48 eV, respectively. Five seconds later, when TH-E entered the core, the minimum electron density had decreased to 1.0 cm^{-3} and the maximum temperature had increased to 113 eV. One second later, when TH-C and TH-D entered the core, the minimum electron density had decreased slightly to 0.95 cm^{-3} and the maximum electron temperature had increased slightly to 116 eV and 131 eV, respectively. Thus, as these four spacecraft observed this event consecutively, the foreshock bubble was in a state of growth and the growth was likely

nearing its end when TH-C, and TH-D observed it. Sixteen seconds later when TH-A entered the event, the minimum electron density had recovered to 2.9 cm^{-3} and the maximum temperature had decreased to 74 eV, maybe because the expansion cannot be supported when the size grows too large.

Table 2.1. *Foreshock bubble shock normal and normal speed measured by each spacecraft*

Spacecraft	Upstream normal	Shock normal Speed in SW frame [km/s]	Estimated size [R_E]
TH-A	[0.60,0.33,-0.72]	210-230	2.6-6.4
TH-B	[0.78,0.20,-0.59]	320-350	
TH-C	[0.66,0.36,-0.65]	250-280	
TH-D	[0.61,0.50,-0.61]	240-250	
TH-E	[0.75,0.19,-0.63]	330-350	

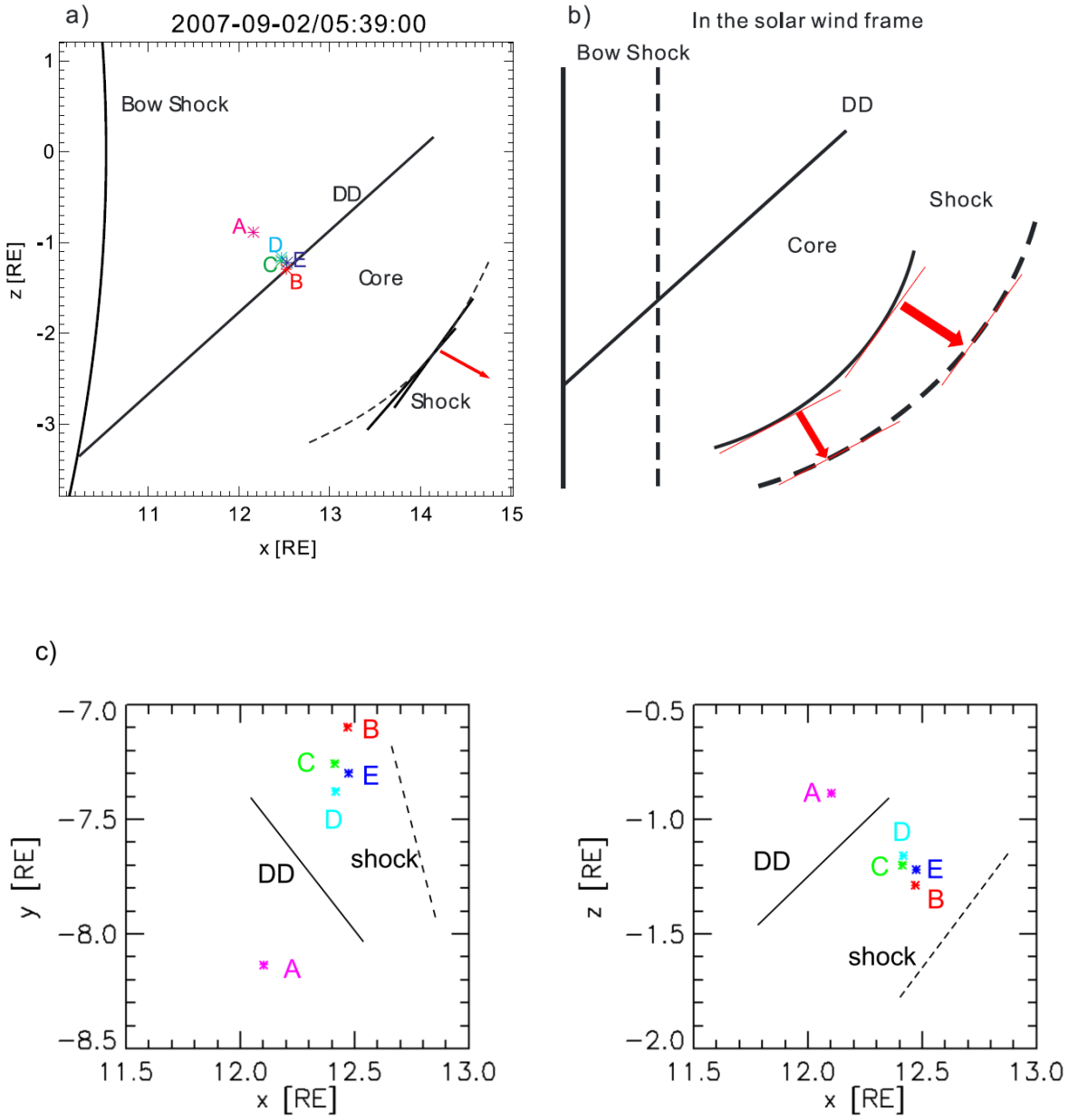

Figure 2.2. *(a) Pictorial representation of the XZ cross section of the foreshock bubble and the bow shock at Y= -7.1 RE, along with spacecraft projections on the same plane (labeled with A-E in different colors). The red arrow indicates the direction in which the foreshock bubble expands in the solar wind frame. The dashed line represents the estimated shape of the foreshock bubble shock. (b) Conceptual representation of how the foreshock bubble expanded and moved in the*

solar wind frame (from solid lines to dashed lines). Red arrows indicate the local shock normal speed, and red lines indicate the local shock surface. DD means directional discontinuity. (c) Enlarged plot of five spacecraft positions projected on the XY and XZ planes. Solid lines and dashed lines indicate the orientation of the discontinuity and the TH-B-measured foreshock bubble shock, respectively.

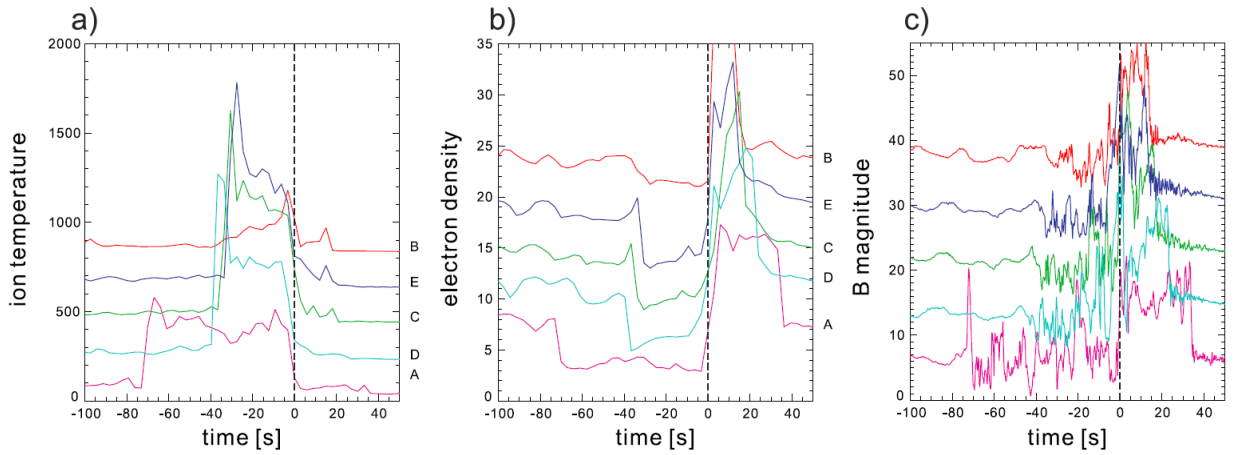

Figure 2.3. *Overlaid, time-shifted foreshock bubble signatures of (a) ion temperature, (b) electron density, and (c) magnetic field strength at the five THEMIS spacecraft. Time zero is when the spacecraft observed the upstream boundary of the foreshock transient. In each plot from top to bottom are TH-B (red), TH-E (dark blue), TH-C (green), TH-D (aqua), and TH-A (purple).*

2.3 Event 2

One hour after event 1, the five THEMIS spacecraft observed a transient phenomenon identified as a foreshock bubble. The driver discontinuity observed by ACE and WIND (Figure 2.4) exhibits IMF angle changes similar to those observed by TH-A. The normal obtained from three-spacecraft timing was [0.63, 0.59, 0.49] with uncertainty below 10°. Because the field strength change was 3% (ACE) and 6% (WIND) and $B_n/|B|$ could reach 0.73 (ACE) and 0.92 (WIND), the discontinuity was identified as a rotational discontinuity. By comparing the IMF from WIND and TH-A observations (Figure 2.4), the discontinuity can be clearly seen on the downstream side of the foreshock transient. The timing of the discontinuity was consistent with the propagation time delay to the downstream boundary of the foreshock transient observed by each THEMIS spacecraft with uncertainty below 20%.

The foreshock transient did not have an obvious downstream compressional boundary, only an upstream shock. The normal of the shock had a predominantly sunward direction. The density ratio of foreshock ions to solar wind ions was not large enough to produce an extreme hot flow anomaly with only one boundary. The size along the upstream shock direction, which varied from ~4 R_E to ~7 R_E, is larger than the typical size of hot flow anomalies. Thus, we identified this foreshock transient as a foreshock bubble driven by a rotational discontinuity.

With observations from multiple spacecraft, the spatial structure and evolution of a foreshock bubble can be studied (Figure 2.5). In this foreshock bubble, the upstream sheath region was very thin, so we can only use MVA to obtain the upstream shock normal. Because they were close to each other, TH-D and TH-E observed a very similar upstream shock orientation with a normal around [0.86, 0.01, 0.50]. Using the distance of two spacecraft along

the upstream shock normal direction divided by the time delay, the shock normal speed in the rest frame was calculated. Then the upstream shock normal speed in the solar wind frame, which ranged from 210 km/s to 350 km/s, was obtained. This shock normal speed was approximately the expansion speed of the foreshock bubble. In addition, TH-A observed a different shock orientation [0.90, -0.44, 0.05]. The angular difference between two parts of the shock was ~30-40°. The radius of curvature estimated from the distance between TH-A and TH-C or TH-D positions (propagated using time delay ~34s) was 1-2.5 R_E, which is smaller than the estimated size of the foreshock bubble. This may be due to the uncertainty in the shock normal determination or to the non-spherical shape of the foreshock bubble (where the curvature radius differs along the surface).

The evolution of the foreshock bubble can be explored by comparing the density and temperature changes. At TH-B, the first spacecraft that entered foreshock bubble, the minimum electron density was 5.0 cm^{-3} and the maximum electron temperature was 19 eV. When TH-C, D, E entered the foreshock bubble ~1s later, the minimum electron density had decreased to 1.1-1.4 cm^{-3} and the maximum electron temperature had increased to ~40-60 eV. The last spacecraft to enter the foreshock bubble (~4s later), TH-A, observed a minimum electron density increase to 3.2 cm^{-3} but no obvious change in ion density and electron temperature. The heating of electrons was weaker than in the foreshock bubble in Section 2.1, and the electron temperature increased from the earthward side to the sunward side of the core, probably because electrons were in the heating process but had not been fully heated when the spacecraft entered the core (in Chapter 5, I will show the reason for this electron energy increase). If we assume that the spatial effect was not dominant, this foreshock bubble was in the growth stage at TH-B and may have stopped growing at TH-A.

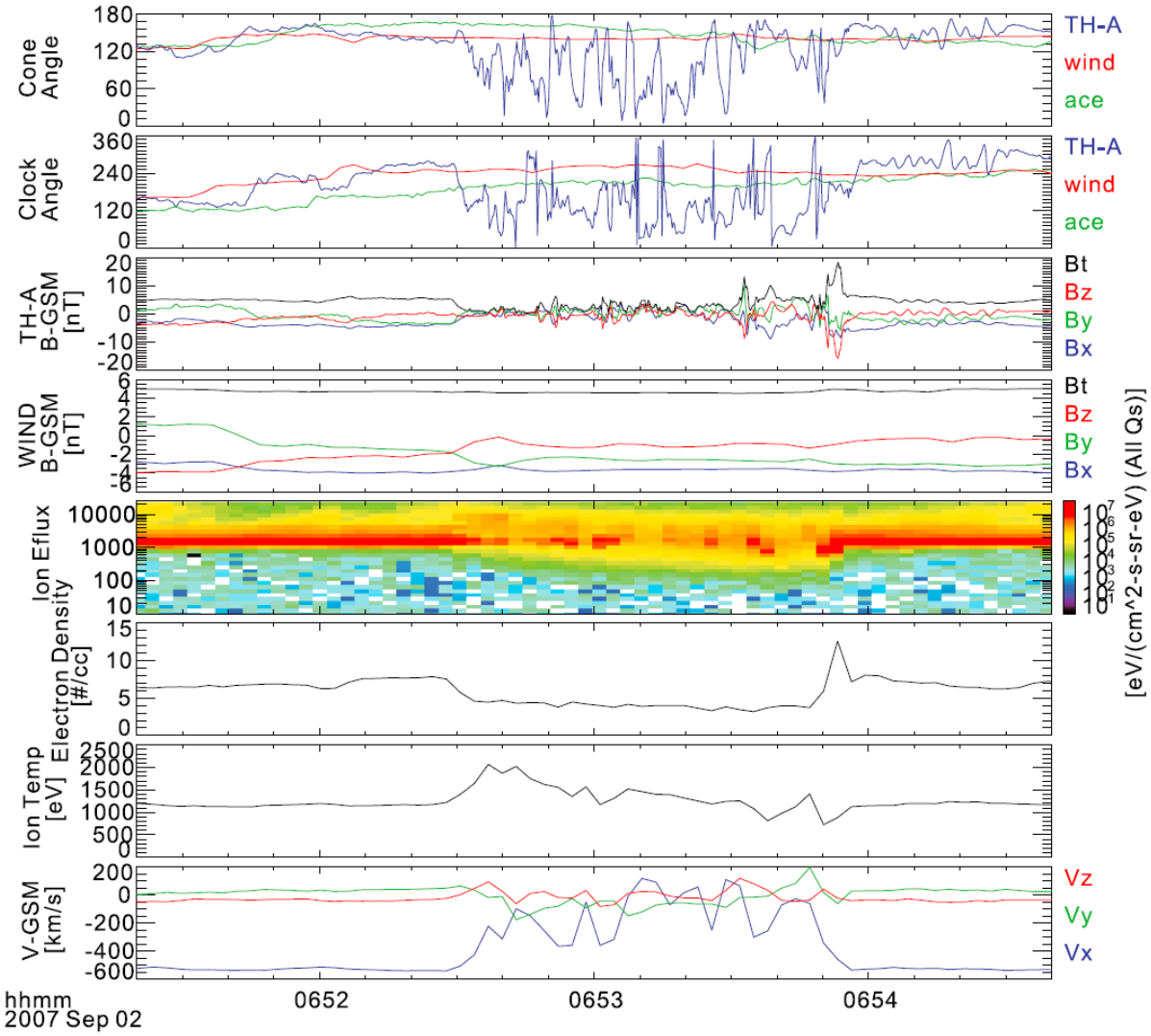

Figure 2.4. *TH-A ([12.3, -7.7, -0.6]) observations of an RD-driven foreshock bubble and ACE and Wind observations of an RD shifted to the same time range as TH-A observations. Similar to Figure 2.1.*

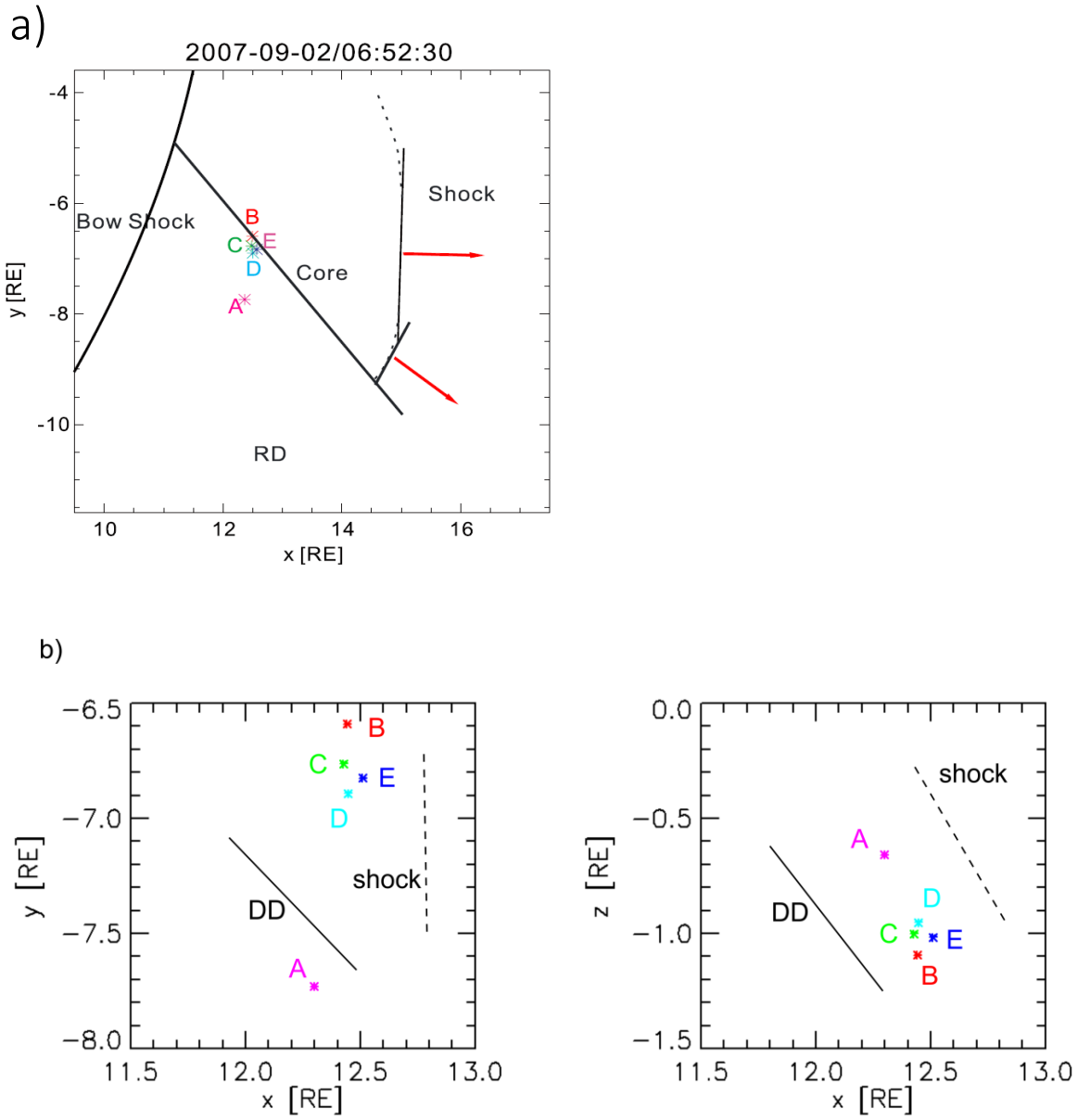

Figure 2.5. *(a) Sketch of an RD-driven foreshock bubble in the X-Y plane at Z=-1 R_E and projection of each spacecraft in this plane. Red arrows illustrate the expansion direction in the solar wind frame. Dashed line indicates the estimated shape of the foreshock bubble shock. (b) Enlarged plot of five spacecraft positions projected on the XY and XZ planes. Solid lines and*

dashed lines indicate the orientation of the discontinuity and the TH-D-measured foreshock bubble shock, respectively.

2.4 Hybrid simulations

To further confirm our observational results, we employ the 3-D global hybrid simulation for a general rotational discontinuity-driven foreshock bubble described in Appendix c (similar simulation results can be found in Chapter 6). From our simulation result (Movie S1), we can see that our inference on this structure from observations is consistent with the simulated structure with a curved shock. We can also see that both the size of the foreshock bubble's core and the thickness of its sheath grow with time in a manner consistent with the observed expansion process. By sampling the simulation output across the foreshock bubble's core along the X axis at Y = 8 R_E, Z = 0 R_E at each time (Movie S2), we can see that the evolution of the plasma parameters in the core is indeed similar to observations: the ion density decreases and the temperature increases after foreshock bubble formation; later, when the foreshock bubble connects to the bow shock, the density and temperature recover. In future I will further investigate the reason for this evolution using both observations and this simulation.

2.5 Summary

Using THEMIS multi-point observations, I demonstrated the spatial structure and evolution of foreshock bubbles. I outlined foreshock bubbles' shapes, estimated the curvature of the foreshock bubble shock, examined how the foreshock bubble expanded, and calculated its expansion speed. I discussed how it evolved and used results from a hybrid simulation to confirm that its evolution and expansion deduced from the data are indeed consistent with modeling.

Our observations covered foreshock bubbles in various states. We applied a simple model to explain their evolution. In the solar wind frame, the plasma begins in a static state. Concentrated foreshock ions interact with solar wind discontinuities, converting part of their kinetic energy

into thermal energy and causing increases in temperature and thus thermal pressure. Because of foreshock bubble expansion, plasma piles up upstream of its core, forming a sheath, and is accelerated to an initial sheath flow speed as the core density continues to drop. This stage is the growth stage. After this initial expansion, the foreshock ions concentrated in the core become an energy source, maintaining the expansion at a power dQ/dt. The energy Q heats the plasma and is converted partly to internal energy of the core plasma U and partly to work done by the thermal pressure supplying kinetic energy to the piled-up plasma in the solar wind frame, i.e., $Q = \Delta U + P\Delta V$. The thermal pressure is proportional to the internal energy of the core plasma. As observed in Event 1 from Section 3.1, the thermal pressure inside the core (not the sheath) varied only little (ion pressure: ~2000 eV cm^{-3}; electron pressure: ~200 eV cm^{-3}), indicating that the internal energy of the core plasma was almost constant, which means that $\Delta U \sim 0$ and $Q = P\Delta V$. The increase in kinetic energy per unit time is roughly $\frac{dQ}{dt} = \frac{dE}{dt} = \pi r^2 \frac{dr}{dt} \Delta\rho V_s^2 = \pi r^2 \Delta\rho V_s^2 V_{exp}$, where r is the radius of the foreshock bubble, $\Delta\rho$ is the density of the piled-up plasma, V_s is the sheath flow speed in the solar wind frame, and V_{exp} is the expansion speed in the solar wind frame. As r increases, $\Delta\rho$ (and probably the expansion speed) should decrease to keep $\frac{dE}{dt}$ constant. This means that the energy source cannot support the acceleration of all the solar wind plasma to the initial sheath flow speed. The core plasma density increase is accompanied by a temperature decrease, maintaining the internal energy almost constant based on observations. We refer to this stage as the remission stage. Different stages of hot flow anomalies were observed by Zhang et al. [2010]. This is the first time, however, that different stages of foreshock bubbles have been observed. In future, simulations can be used to confirm or amend this model and help us understand the evolution of foreshock bubbles.

Chapter 3. Foreshock bubble foreshock

In the simulations [Omidi et al., 2010], a foreshock bubble's shock could reflect solar wind particles and form a new foreshock. Although a field-aligned ion beam was observed upstream of a foreshock bubble shock by Archer et al. [2015], further analysis is required to prove that the ion beam was from that shock. Additionally, the joint structure of the foreshock bubble shock and the bow shock may accelerate particles through Fermi acceleration [Omidi et al., 2010; Turner et al., 2013]. As foreshock bubbles form upstream of quasi-parallel shocks propagating through inhomogeneous media, their ability to accelerate particles may provide a new dimension in studies of particle energization at such shock environments. In this chapter, I will take the first step in this broader context. Using THEMIS observations, I select the clearest example (out of three) to provide confirmation using data analysis and comparison with the shock drift acceleration model that indeed a new ion and electron foreshock region does form upstream of some foreshock bubble shocks.

3.1 Observation of a foreshock bubble foreshock

As shown in Figure 3.1, TH-C at [16.9, 1.6, -3.6] R_E in GSM near the bow shock observed a transient foreshock structure. Across the structure, the local bow shock changed from quasi-perpendicular to quasi-parallel (panel h in Figure 3.1; the purple line indicates bow shock θ_{Bn} calculated from TH-C data and the red line is from ACE data shifted by ~3480 seconds in accordance with a solar wind speed of 399 km/s). This structure did not have an obvious downstream compressional boundary and had a shock with a fast-mode wave Mach number ~3.6 on its sunward side. The density ratio of reflected ions to incident ions is less than 0.3, meaning that this structure cannot be an extreme hot flow anomaly with only one compressional boundary

based on Thomsen's model [1988]. The shock normal is [0.86, -0.50, 0.09] when the co-planarity method with uncertainty below 10° is used and [0.84, -0.50, 0.22] when the MVA method with uncertainty below 5° is used. These are consistent with each other and show a strong sunward direction. The shock normal speed in the solar wind frame or expansion speed V_{exp} is around 140-200 km/s in the sunward direction. The size of this foreshock transient is around 1.9 R_E along the shock normal direction. Using criteria by Turner et al. [2013], we identified this foreshock transient as a small foreshock bubble. The small size is due to the slow expansion speed, which is probably caused by the slow solar wind speed (399 km/s).

The driver discontinuity was observed by TH-B at [24.5, -9.8, -6.4] R_E, at ~19:59 UT and ACE at [237.2, 36.8, -12.2] R_E at ~19:00 UT (both in GSM coordinates). Across the discontinuity, the magnetic field strength increased by 13% and the density increased by ~0.4 cm^{-3} (~20%). The normal obtained using three-spacecraft timing is [0.55, 0.56, 0.62] with uncertainty <10°. The discontinuity was likely a tangential discontinuity as B_n crossed zero. However, here an identification of the discontinuity type is not necessary. I simply call it a directional discontinuity (DD). The geometry of the bow shock (using the Merka et al., 2005 model), the spacecraft positions, the DD, the location of the ion foreshock before and after the DD, the foreshock bubble shock, and the local IMF direction are sketched in Figure 3.2a.

From Figure 3.1 and 3.2a, we can see that TH-C was in the Earth's foreshock. Downstream of the foreshock bubble in the quasi-perpendicular regime, more beam-like ions were observed; upstream of it in the quasi-parallel regime, more diffuse ions were observed (Figure 3.1c). Upstream of the foreshock bubble shock from 19:58:18 UT to 19:58:40 UT, the ion energy flux spectrum shows an energy enhancement at around 2 keV (panel c). During the same period, the 180° pitch-angle (~sunward) electron energy flux at around tens to hundreds eV was enhanced

(panel d). As the IMF was connected to the foreshock bubble shock at this moment, as shown in Figure 3.2a, these high energy ions and electrons likely came from the foreshock bubble shock and made up a new foreshock in addition to the background Earth's foreshock. To further examine this scenario, we applied shock acceleration theory to calculate the reflected ion beam velocity and compared it with observations.

As seen in Figure 3.3a, which shows the ion distribution in the BV plane close to the upstream side of the foreshock bubble shock (from 18:58:18 to 19:58:21 UT), in addition to the solar wind ion beam in the parallel direction, there was another ion beam in the opposite direction. This ion beam was field-aligned, as it had the same perpendicular speed as the solar wind (the $E \times B$ drift speed). Because the beam parallel speed was larger than the solar wind speed, this ion beam should be caused by adiabatic reflection (mirror reflection) rather than specular reflection. To calculate the adiabatically reflected beam velocity at the foreshock bubble shock, we first transformed the frame of reference into the foreshock bubble shock normal incident frame. In this frame, the incident beam velocity, $\boldsymbol{V_i} = \boldsymbol{V_{sw}} - \boldsymbol{V_s}$, where the solar wind velocity $\boldsymbol{V_{sw}}$= [-399, -27, -24] km/s (in GSM) and the foreshock bubble shock normal velocity in the spacecraft frame, $\boldsymbol{V_s}$= [-154, 90, -16] km/s. Then we transformed the frame of reference into the de Hoffmann-Teller frame by subtracting the de Hoffmann-Teller velocity, $\boldsymbol{V_{HT}} = \frac{\boldsymbol{n_s} \times (\boldsymbol{V_i} \times \boldsymbol{B})}{\boldsymbol{n_s} \cdot \boldsymbol{B}}$, where $\boldsymbol{n_s}$ is the shock normal vector. By definition, the incident beam in this frame is along the local field line direction, $|\boldsymbol{V_i} - \boldsymbol{V_{HT}}| = V_{\|i} = V_i \cos\theta_{Vn} / \cos\theta_{Bn}$. By reversing the beam speed direction and adding the de Hoffmann-Teller velocity and the foreshock bubble shock normal velocity in the spacecraft frame (Figure 3.2b), we obtained the reflected beam velocity in the spacecraft frame, $\boldsymbol{V_r} = -(\boldsymbol{V_i} - \boldsymbol{V_{HT}}) + \boldsymbol{V_{HT}} + \boldsymbol{V_s} = -\boldsymbol{V_{sw}} + 2(\boldsymbol{V_s} + \boldsymbol{V_{HT}})$. Assuming that the foreshock bubble did not exist and that the IMF was connected to the bow shock, we calculated

another reflected beam velocity for comparison, $\boldsymbol{V_r' = -V_{sw} + 2V'_{HT}}$, where $\boldsymbol{V'_{HT}}$ is the de Hoffmann-Teller velocity of the model bow shock.

In the ion energy spectrum in Figure 3.1c, the blue dots indicate the calculated ion beam energy for adiabatic reflection at the foreshock bubble shock; the purple and red dots are the beam energy for adiabatic reflection at the bow shock with local (TH-C) and undisturbed (shifted ACE) IMF direction, respectively. Before the foreshock bubble, the red dots match the observed ion beam energy very well, confirming that this ion beam was adiabatically reflected at the local quasi-perpendicular bow shock (also seen in Figure 3.2a, pink lines). After the foreshock bubble shock, however, the red dots do not match the beam energy except very close to the shock. The blue dots, on the other hand, match the beam energy, which dropped from 2 keV to hundreds of eV. The purple dots match this dropping tendency, but the calculated energy is too large compared to the beam energy. The calculated difference between the blue dots and purple dots is mainly because the foreshock bubble shock was moving slowly earthwards in the spacecraft frame, resulting in lower reflected beam energy. To further compare our calculation with the observations, we need to analyze the ion distribution functions (Figure 3.3a, b).

In Figure 3.3a, b, the blue dot on the ion distribution function (from 18:58:18 to 19:58:21 UT) is the averaged expected beam velocity from reflection at the foreshock bubble shock. The blue ellipse represents the uncertainty from the shock normal and shock normal speed uncertainty and the variation of the IMF direction within the 3s spin. The calculated beam velocity is in excellent agreement with the ion beam observed in both the XZ_{gsm} cuts and the BV cuts. The purple dot and ellipse represent the calculated beam velocity if we assume there was no foreshock bubble and the local IMF (at TH-C) was connected to the bow shock, which is clearly inconsistent with the reflected ion beam. However, the purple dot may lie on another population,

the background diffuse ions (also in Figure 3.1c). These diffuse ions may be the reflected beam from the local bow shock that was scattered by ULF waves and at this later time exists together with the new beam reflected from the foreshock bubble shock. The red dots depict the calculated beam velocity from the bow shock with an undisturbed IMF (shifted ACE data). Even though the red dots are consistent with the observed beam energy at this moment (Figure 3.1c), the calculated beam direction was inconsistent: the reflected beam had a very small negative X_{GSM} component and was thus mainly in the Y-Z_{GSM} direction (Figure 3.3b), whereas the calculated beam velocity from the bow shock had a strong positive X_{GSM} component. This negative X_{GSM} component is because the reflected beam was convecting with the foreshock bubble shock. Thus, the sunward beam in the shock rest frame became slightly earthward in the spacecraft frame (as illustrated in Figure 3.2b). Additionally, by backward tracing the observed ion beam, we can estimate when and where the beam was created. For example, the ion beam observed at 19:58:35 was from ~30 s ago and ~2 R_E along the Y-Z_{GSM} direction. By subtracting the distance caused by convection with the driver discontinuity, we can obtain the size of the foreshock bubble along the foreshock bubble shock surface direction at 19:58:05, ~1.5 R_E, comparable to the size along the foreshock bubble shock at this moment, ~1.6 R_E. Therefore, by comparing observations with the adiabatic acceleration model, we further confirm that the ion beam upstream of the foreshock bubble shock should be the adiabatically reflected ion beam at the foreshock bubble shock, which made up a new foreshock different from the background Earth's foreshock.

In addition to the reflected ion beam, a reflected electron beam can be identified from further analysis. In Figure 3.1, the electron energy flux at 0° and 180° pitch angles (panels d and e) and the ratio of 180° to 0° pitch angles at different energies (panel f spectrum, panel g line plot) are presented. The field-line direction is on average in anti-sunward, meaning that the 0°

pitch angle is anti-sunward and the 180° pitch angle is sunward. We can see that the sunward electron energy flux was enhanced near the foreshock bubble shock around tens to hundreds of eV on average by a factor of ~1 – 2 (2 – 4) over that at the background foreshock before (after) the discontinuity, while the anti-sunward electron energy flux at this energy range was almost unvaried. At low energies, around 24-42 eV, the anti-sunward electron energy flux was always around three to five times the sunward electron energy flux. These electrons were likely solar wind strahl electrons. At higher energies above 73 eV, immediately upstream of the foreshock bubble shock, the sunward electron energy flux was 3 to 7 times larger than the anti-sunward electron energy flux, and this ratio gradually decreased to background level, ~1. The reason that flux ratio in the Earth's foreshock upstream of the foreshock bubble was close to one is likely that the local bow shock upstream of the discontinuity was quasi-parallel on average, unable to create an electron beam [Fitzenreiter, 1995]. Downstream of the discontinuity where the local bow shock was quasi-perpendicular, there was indeed strong sunward electron energy flux, but not as strong as that upstream of the foreshock bubble shock. (Inside the core, however, the ratio was ~1 at almost all energies, indicating isotropy or high thermalization.) To conclude, more high energy sunward field-aligned electrons from the foreshock bubble shock were observed than from the background local bow shock: a new electron foreshock was formed.

Similar calculations of reflected ion beam velocity can be applied to electrons. The corresponding electron beam energy is only several eV (because such calculation does not include the cross potential of shocks). If, however, that shock potential is included, the reflected electron beam should be in ten or a few tens of eV. Indeed, the electron distribution above 50 eV shows an anti-parallel (sunward) gyrotropic electron beam (Figure 3.3c). Therefore, the electron distribution functions also indicate an electron beam reflected by the foreshock bubble shock

although not as straightforwardly as indicated by the ion distribution functions.

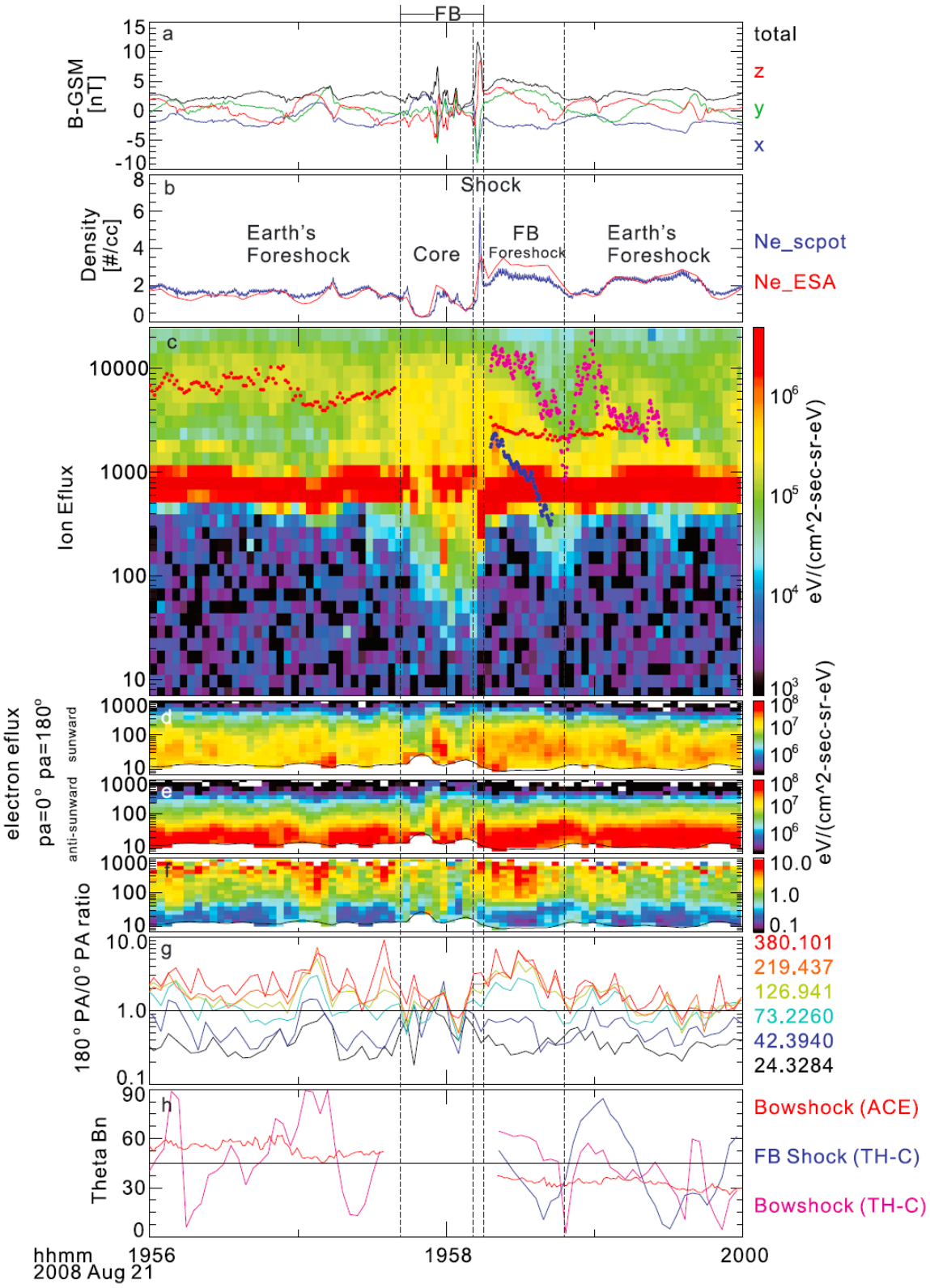

Figure 3.1. *TH-C observation of the event. From top to bottom: (a) magnetic field components in*

GSM coordinates (XYZ in blue, green, and red, respectively) and magnitude (black); (b) electron density from ESA (red) and EFI (blue); (c) ion energy flux spectrum – blue dots represent the calculated ion energy reflected by the foreshock bubble shock using TH-C magnetic field, purple dots and red dots represent the calculated ion energy reflected by the bow shock using TH-C and shifted (by ~3480s) ACE magnetic field, respectively; (d) 180° *pitch-angle electron energy flux; (e)* 0° *pitch-angle electron energy flux; (f) the ratio of* 0° *to* 180° *pitch-angle electron energy flux (spectrum); (g) the ratio of* 0° *to* 180° *pitch angle electron energy flux at different energy (line plot); (h)* θ_{Bn} *of the foreshock bubble shock (blue) and local bow shock (purple: from TH-C magnetic field data, red: from shifted ACE field data).*

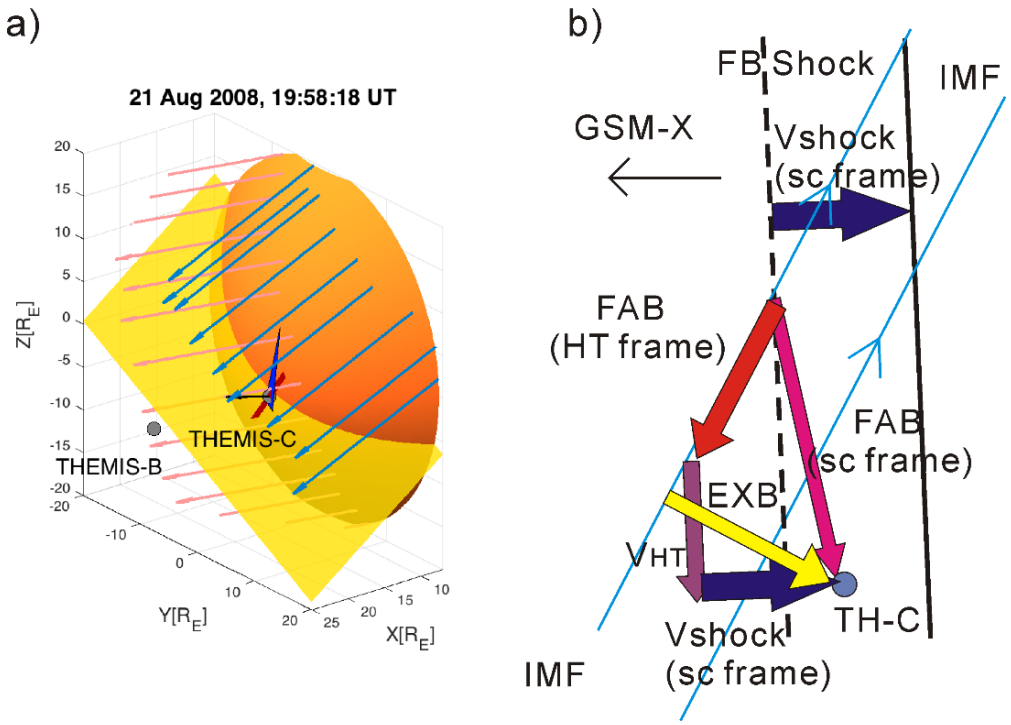

Figure 3.2. *(a) The 3D sketch of bow shock (orange), foreshock bubble shock (blue triangle), directional discontinuity (yellow rectangle), spacecraft positions (grey circles), and the estimated direction of reflected ion beams before/after the discontinuity (long pink/light blue arrows), and the local magnetic field orientation (red line) when TH-C observed the ion beam from foreshock bubble shock (GSE). The short black arrow gives the normal vector of the foreshock bubble shock. (b) Sketch of field-aligned beam (FAB) direction from the de Hoffmann-Teller frame (HT frame) to the spacecraft frame (sc frame).*

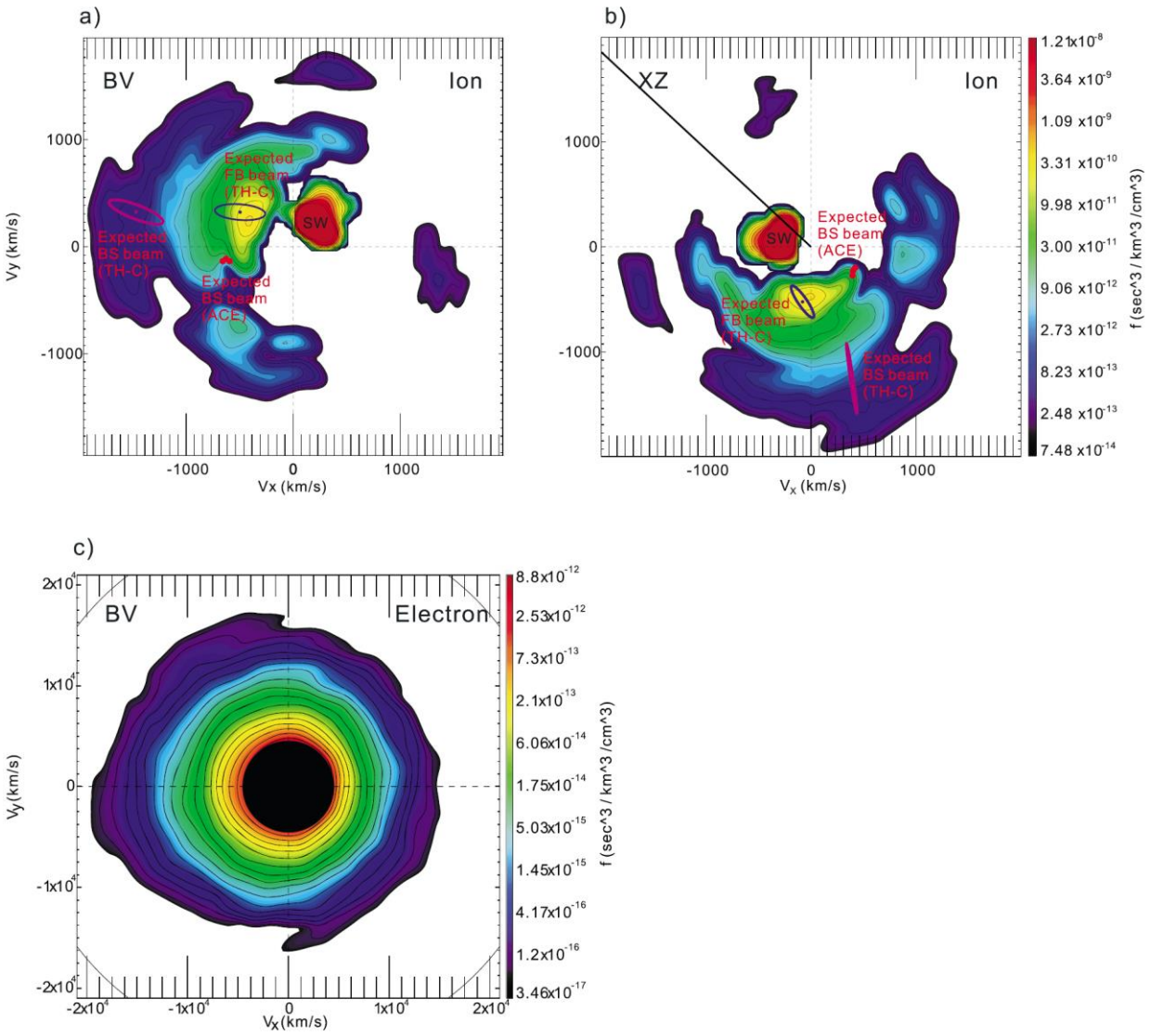

Figure 3.3. *Ion and electron distribution functions at 16:48:22-16:48:25 UT. (a) Ion distribution function in the BV cut (X axis is parallel to the magnetic field direction and XY plane is defined by the bulk velocity direction); (b) Ion distribution function in the GSM-XZ cut – black line indicates the spin-averaged (TH-C) magnetic field direction; (c) electron distribution function from 50 eV to 2 keV in the BV cut; In (a) and (b) the blue dot indicates the average calculated ion beam velocity from reflection at the foreshock bubble shock using the local TH-C magnetic field. Purple dot indicates the average calculated ion beam velocity from reflection at the local*

bow shock using the local TH-C magnetic field. Ellipses represent the uncertainty in the calculated ion beam velocity due to the variation of IMF direction within 3s and the uncertainty in the determination of foreshock bubble shock normal and shock normal speed. Red dots indicate the calculated ion beam velocity from reflection at the local bow shock by using shifted ACE magnetic field. BS is short for bow shock. SW is short for solar wind.

3.2 Summary

Using THEMIS observations, I presented definite evidence of a new foreshock region formed upstream of a foreshock bubble's shock. In this new foreshock bubble foreshock region, we observed a field-aligned ion beam and an electron beam with an IMF connected to the foreshock bubble shock. I showed that the field-aligned ion beam was accelerated through adiabatic reflection (shock drift acceleration) at the foreshock bubble shock.

Quasi-parallel shocks are traditionally considered less efficient particle accelerators than quasi-perpendicular ones [e.g., Lee et al., 2012]. However, the "either-or" view of acceleration efficiency versus shock obliquity has been questioned in recent studies [e.g., Eastwood et al., 2005, Omidi et al., 2010; Omidi et al., 2013; Wilson et al., 2013] that have clearly demonstrated a richness of transients upstream of a quasi-parallel parent shock where quasi-perpendicular regimes are embedded in the upstream region of quasi-parallel shocks. Therefore, the two obliquity regimes may co-exist, and shock acceleration must be considered in an integrated environment that includes upstream foreshock conditions and the evolutionary history of an event, given that an approaching interplanetary discontinuity may abruptly change shock obliquity as well as introduce foreshock transient interactions. We find that foreshock bubbles arising in the approaching solar wind upstream of a quasi-parallel bow shock create conditions of efficient acceleration ahead of them in the new shock/foreshock environment. Using THEMIS multi-point observations, we explored a foreshock bubble shock that was able to accelerate particles by a factor of 2-3 upstream of it. In our other two events, TH-C observations at 2008-07-18/16:48 and 2008-09-08/20:25 (Archer et al [2015] reported a field-aligned beam in this event, and we confirm that the beam is indeed from the foreshock bubble shock), particles can be accelerated to even larger energy due to their different foreshock bubble shock orientation and

IMF direction. These accelerated particles could convect with the foreshock bubble shock towards the parent shock. This means that foreshock bubble shocks could act as an additional accelerator in the foreshock environment and also as a particle source of diffusive shock acceleration for quasi-parallel parent shocks. In the future, statistical study can be applied to further investigate this process.

C. Part II. Particle acceleration by foreshock transients

In Part I, I showed that foreshock bubbles can accelerate particles and contribute to parent shock acceleration. In Part II, I further investigate whether other foreshock transients with similar characteristics can also accelerate particles and then determine how they could do so. Therefore, in Chapter 4, I first apply a statistical study mainly including foreshock bubbles, hot flow anomalies, and spontaneous hot flow anomalies to show the acceleration frequency and the crucial solar wind parameters that determine their particle acceleration. In Chapter 5, I will apply case studies along with test particle simulations and hybrid simulations to reveal two electron acceleration mechanisms. In Chapter 6, I will use case studies and hybrid simulations to reveal an ion acceleration mechanism.

Chapter 4. Statistical study of particle acceleration

In Chapter 3, I showed that foreshock bubbles can accelerate solar wind particles. Case studies by Wilson et al. [2016] also show that foreshock transients can accelerate electrons to hundreds of keV. Foreshock transients thus hold high potential as the source of parent shock acceleration and affect parent shock structure, requiring further investigation that could improve our understanding of shocks. In this chapter, I will present the statistical characteristics of particle acceleration by foreshock transients that have hot, tenuous core with plasma deflection, including foreshock bubbles, hot flow anomalies, spontaneous hot flow anomalies, and foreshock cavities. Although the distinction of these foreshock transients is still debated, particles in their similar cores could experience similar processes and general acceleration mechanisms. I will introduce how we collect events and measure particle energy in Section 4.1. Then in Sections 4.2 and 4.3, I will show that most foreshock transients can accelerate electrons, and at least some of

them can also accelerate ions. I will reveal that solar wind speed is critical to the particle acceleration energy.

4.1 Data and methods

By examining TH-B and TH-C observations upstream of the bow shock in 2008 and 2009, we established an event list of 247 foreshock transients with a core associated with foreshock ions (Appendix d). Our events include hot flow anomalies, spontaneous hot flow anomalies, foreshock bubbles, and foreshock cavities that have a finite flow deflection. We exclude SLAMS and foreshock cavitons, however, as they are more closely related to waves and have different characteristics. Figure 4.1 is an example (a hot flow anomaly) of an event in our list observed by TH-C.

In this chapter we only consider particle energization inside the cores of foreshock transients. The boundary of the core is defined as the point where density and field strength start to drop (two dashed vertical lines in Figure 4.1). The average value of the quantities described below is calculated in the time interval of the core. We also choose a background time interval within 5 min of the event either downstream or upstream, depending on which region contains only background foreshock particles (two dotted vertical lines in Figure 4.1), in order to obtain the typical foreshock particle energy spectrum for comparison with that inside the core.

To quantify the energization, we need to process the particle data beyond the standard moments and spectra. For ions, we first combine ESA and SST distributions. Next, we calculate the first order moment to obtain the mean kinetic energy and the second order moment to obtain the mean thermal energy of the non-solar wind component to characterize ion energization. Thus, we need to remove the solar wind beam from the ion distribution before computing the moments. We obtain the rough solar wind velocity from the total ion distribution by confining the phi angle

and then remove counts in the bins that are less than 3-5 angular and energy bins away from the solar wind velocity in the ion distribution. Then we fill these bins by interpolation. Because the ESA treats all ions as protons (mass over charge = 1), an alpha beam from the solar wind (mass over charge = 2) will appear at around two times the solar wind proton energy. We remove the alpha beam in the same way as the solar wind protons. Figure 4.1e shows the energy spectra of the non-solar wind component after ESA and SST have been combined. It is evident that the typical solar wind beam around 1 keV (see Figure 4.1d) has been removed. We then calculate the density, mean thermal energy, and mean kinetic energy shown in Figure 4.1f, g, h and other products. Inside the core, the density of the non-solar wind component increased, because to form a hot flow anomaly, foreshock ions must be concentrated by a driver discontinuity (as discussed in Chapter 1), and some cold solar wind ions can be thermalized in the core and mix with the non-solar wind ions [Wang et al., 2013; Chu et al., 2017]. In Figure 4.1g, h, we see that inside the core, the non-solar wind ion mean thermal energy increased as the mean kinetic energy decreased. This is because after foreshock ions pass through a discontinuity, their parallel speed must be projected in a new direction and thus decreases (see Chapter 1). In the discontinuity frame where the convection electric field is zero, particle energy is conserved. The decreases in kinetic energy (calculated from mean parallel speed) result in increases in thermal energy [e.g., Archer et al., 2015; Liu et al., 2015]. The increased thermal pressure of the core causes foreshock transients to expand.

In addition to these moments, we calculate the Kappa index of the ion phase space density distribution as another energization estimate by assuming that ion distributions follow a Kappa distribution. A smaller Kappa index means a stronger deviation from thermal equilibrium. To fit

the Kappa distribution, we transform the distribution of non-solar wind ions into their rest frame and obtain the corresponding energy spectra.

As for electrons, we combine ESA and SST electron distributions only in particle burst mode; we do not combine them in fast survey mode because of the poor angular resolution in that mode. Because two different modes may cause statistical differences, events in different modes are labeled separately. As we cannot directly remove solar wind electrons from the distribution, we concern ourselves only with their suprathermal tail. We define the suprathermal component as that with energy greater than three times the average temperature (Figure 4.1j, blue line). To quantify the electron energization, we calculate the average temperature of the suprathermal tail (Figure 4.1j red line, from ESA only in fast survey mode and from the combined distribution in particle burst mode). We also calculate the partial pressure of the suprathermal tail, and then we calculate $E_{5\%}$, the energy above which the bins contribute 5% to the partial pressure (in fast survey mode, we calculate partial pressure in ESA and SST separately and then add them up; in particle burst mode, we calculate it from the combined distribution). As with ions, we also calculate the Kappa index of the electron phase space density distribution below 1 keV (to avoid noise) after the frame transformation into the electron rest frame (Figure 4.1k). To approximate the maximum energy of electrons, we also determine the maximum energy bin for ESA or SST that can observe fluxes above the 1-count level after instrumental background noise subtraction. When determining the maximum energy in the SST energy range in fast survey mode, we also require that the electron signal be detected by at least the lowest three energy channels to fully distinguish it from noise.

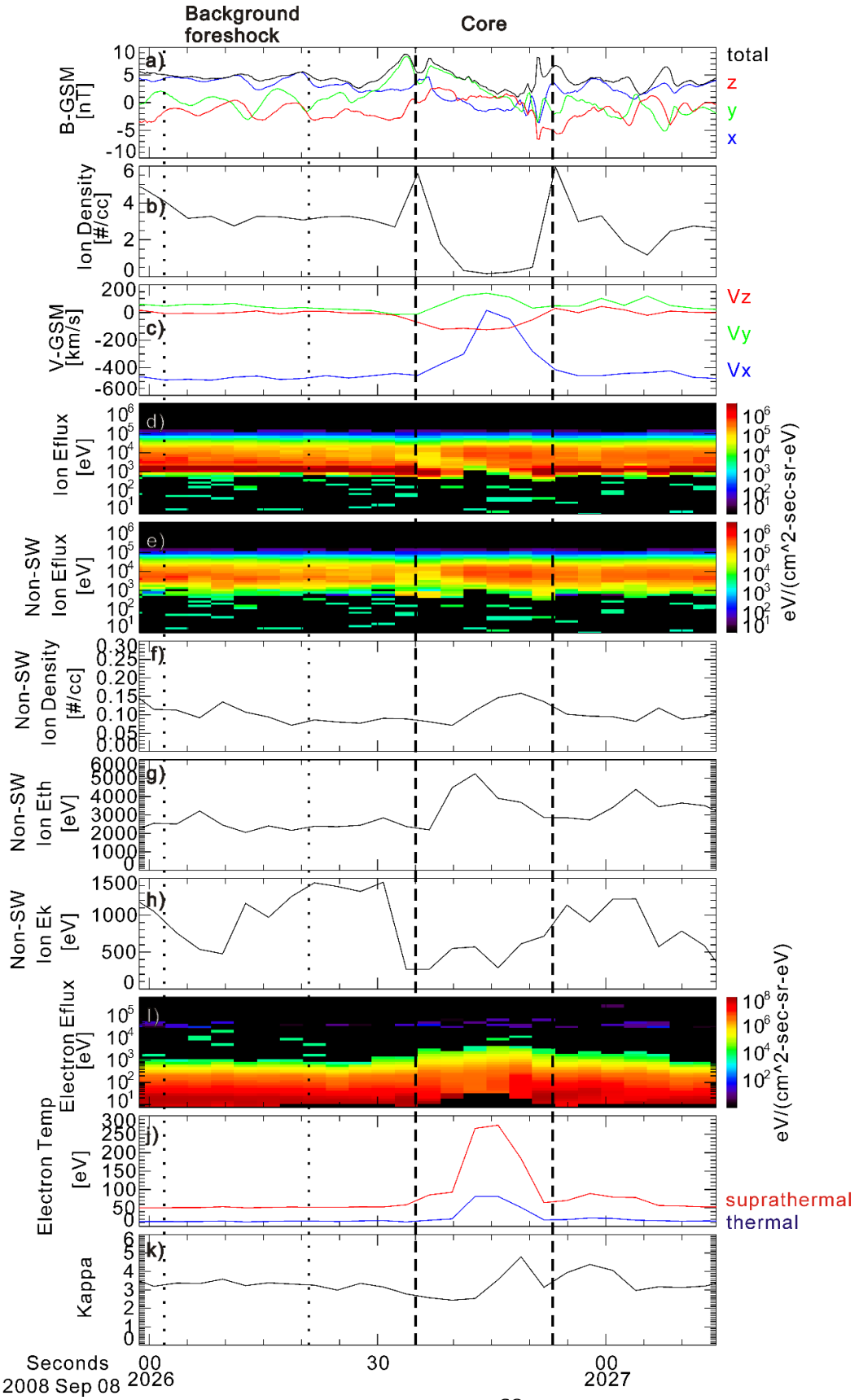
Background foreshock
Core
a)
B-GSM [nT]
total
z
y
x
b)
Ion Density [#/cc]
c)
V-GSM [km/s]
Vz
Vy
Vx
d)
Ion Eflux [eV]
e)
Non-SW Ion Eflux [eV]
eV/(cm^2-sec-sr-eV)
f)
Non-SW Ion Density [#/cc]
g)
Non-SW Ion Eth [eV]
h)
Non-SW Ion Ek [eV]
i)
Electron Eflux [eV]
eV/(cm^2-sec-sr-eV)
j)
Electron Temp [eV]
suprathermal
thermal
k)
Kappa
Seconds
2008 Sep 08
00
2026
30
00
2027

Figure 4.1. *TH-C observation of a typical foreshock transient (a hot flow anomaly) and various data products constructed from the particle distributions and used further in our statistical study. From top to bottom: (a) magnetic component in GSM coordinates (XYZ, total in blue, green, red, black, respectively); (b) total ion density; (c) ion bulk velocity in GSM coordinates (XYZ in blue, green, red, respectively); (d) ion ESA and SST (combined) energy spectra; (e) ion ESA and SST (combined) energy spectra of non-solar wind component; (f) ion density of non-solar wind component; (g) ion mean thermal energy of non-solar wind component; (h) ion mean kinetic energy of non-solar wind component; (i) electron ESA and SST (combined) energy spectra; (j) electron average temperature of total population (thermal, in blue) and suprathermal tail (in red); (k) Kappa index of the electron phase space density distribution in the energy range below 1 keV.*

4.2 Statistical results of electron energization

Now we analyze the statistical results of electron energization (see Figure 4.2). Calculating the average temperature of the suprathermal tail and $E_{5\%}$, the energy above which the bins contribute 5% to the partial pressure, we found that nearly 90% of the events have core electrons that are more energized than the ones in the background foreshock (see Figure 4.2d, e, horizontal lines). More than 70% of events also show a smaller Kappa index inside the core than in the background foreshock (see Figure 4.2f, horizontal line), indicating stronger energization. Thus, most foreshock transients energize electrons. In ~30% of our events, the maximum energy is larger than 25 keV (minimum SST energy range) in Figure 4.2g. In some of them, energies are hundreds of keV to 700 keV, consistent with the 100-300 keV events reported by Wilson et al. [2016] (their events are shown in green in Figure 4.2g).

Electron energy estimates in fast survey mode (black) and particle burst mode (orange) show no clear statistical differences except at around 25 keV in Figure 4.2g. This is because in the fast survey mode SST energy range, we require electrons to be detected by at least the lowest three energy channels, i.e., the threshold for the electron maximum energy is ~50 keV.

Next, we examine whether electron energization depends on solar wind speed. We find that average temperature of the suprathermal tail (Figure 4.2a) and $E_{5\%}$ (Figure 4.2b) increase with increasing solar wind kinetic energy. Additionally, electron Kappa indices (Figure 4.2c) decrease with increasing solar wind kinetic energy. Comparing the maximum energy that can be detected by the particle instruments with the solar wind speed, we see that the highest maximum energies more likely occur at high solar wind speed (Figure 4.2g, SST energy range). Normalizing our energization estimates in the core to those in the background foreshock (Figure 4.2d, e, f), we find that the correlations (except for the Kappa index) still hold, especially when the solar wind

kinetic energy is below ~2 keV (~620 km/s). Thus, the solar wind speed can affect the electron acceleration process. This effect, however, appears to saturate when the solar wind speed becomes too large (> 2 keV, ~620 km/s in Figure 4.2).

How, then, could foreshock transients accelerate electrons? One possible way is reflection at the upstream boundary like ions [e.g., Omidi et al., 2010]. Because electrons are fast, they can bounce between boundaries multiple times. If this bouncing is between the bow shock and the earthward-moving upstream foreshock boundary, electron energy could increase through Fermi acceleration. In Chapter 5, I will show the evidence of this acceleration process.

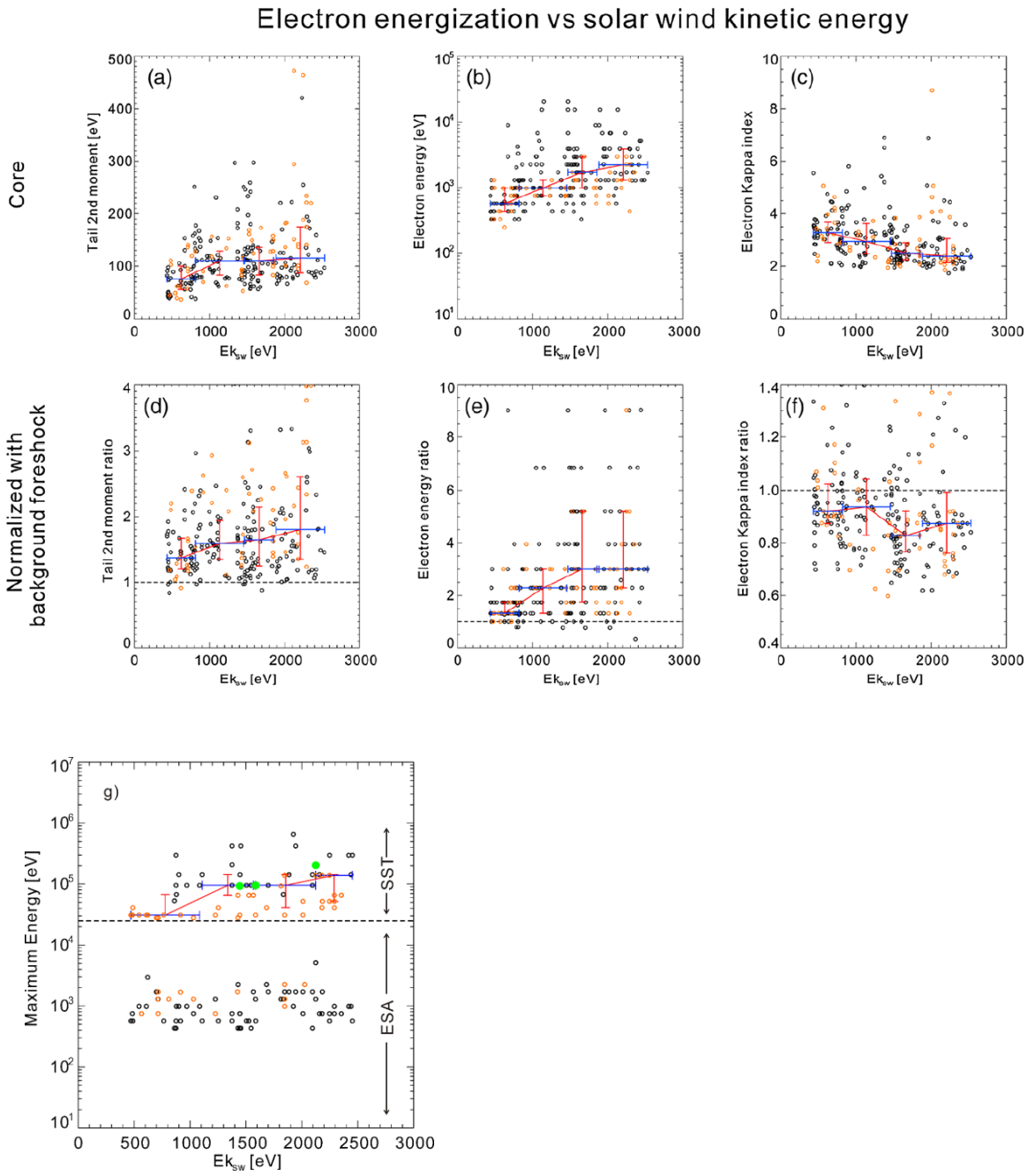

Figure 4.2. *Electron energization estimates plotted against solar wind kinetic energy: average temperature of suprathermal tail (a); $E_{5\%}$, the energy above which the bins contribute 5% to the partial pressure (b); Kappa index of the phase space density distribution (c); and normalized estimates for these quantities (d, e, f, respectively) are their ratios to the background. Dashed*

horizontal lines in (d, e, f) are at ratio = 1, which indicates that most events have electrons more energized than those in the background foreshock. Electron energy energization estimates with and without normalization to the background are all positively correlated with the solar wind speed. The maximum energy that can be detected by particle instruments, another measure of energization, is shown in (g). Higher maximum electron energy is more likely seen at higher solar wind speed. Green dots in (g) indicate the events reported in Wilson et al. [2016]. Red lines are medians, and error bars signify quartiles (25% and 75%). Dark blue horizontal bars indicate the data bins in which median and error bars are calculated (each data bin contains an equal number of data). Orange indicates events in particle burst mode. Events in particle burst mode show no statistical differences from events in fast survey mode (black) in (a)-(f). In (g), only orange circles can be seen around 25 keV, because we require that events in fast survey mode be detected by at least the three lowest energy channels of SST.

4.3 Statistical results of ion energization

After we obtain the non-solar wind ions mean kinetic energy, mean thermal energy, and Kappa index (described in Section 4.1), we study their statistical characteristics as a function of the solar wind parameters.

We first compare the mean total energy (mean kinetic energy plus mean thermal energy) inside the core with the value in the background foreshock. As shown in Figure 4.3, the mean total energy inside the core overall is a little smaller than that in the background foreshock. So why is the ion energy decreased? One possible reason is expansion of the foreshock transients. Because of the high thermal pressure in the core, the core expands and pushes the surrounding solar wind cold plasma and magnetic field. This process requires ions to do work approximately equal to the volume change multiplied by the pressure. To further explore this scenario, we identified all events with a shock-like structure (i.e., pink circles in Figure 4.3). Almost all such events are below the diagonal in Figure 4.3. We suggest that this is because the amount of energy ions lose depends on the speed of expansion. If a shock is observed, the expansion must be faster than the local fast-mode speed. Therefore, more of the plasma's internal energy needs to be consumed for the expansion. The ion energy may also be used to generate waves. However, wave energy is typically much smaller than the expansion energy, which is comparable to the solar wind kinetic energy. Another possible reason is that some remaining cold solar wind ions could be thermalized in the core [Wang et al., 2013; Chu et al., 2017] and mix with the non-solar wind ions. As the energy of a solar wind ion is generally smaller than that of a foreshock ion, mixing of thermalized solar wind ions could result in an underestimate of the energy of the non-solar wind ion component.

Although ions must lose energy to support the formation and expansion of foreshock transients, ~30% of our events have a mean total energy inside the core that is larger than the value in the background foreshock. Thus, there could be ion acceleration processes inside the core. One possible zero-order acceleration mechanism inside the core is reflection at the earthward-moving upstream boundary of foreshock transients. Let us consider foreshock bubbles as an example. Foreshock bubbles and their upstream boundary should convect with the solar wind toward the bow shock. Reflection in the core at its upstream boundary will give ions additional velocity approximately equal to two times the normal speed of the upstream boundary in the Earth frame. Foreshock bubbles also have an earthward-moving downstream boundary, however. Because foreshock bubbles expand, the downstream boundary should move faster towards the bow shock than the upstream boundary (in the Earth frame). Therefore, ions trapped in the core between these two boundaries will lose more energy by reflecting at the downstream boundary than they would gain by reflecting at the upstream boundary. This is a picture of energy transfer from ions to expansion from the perspective of a single ion. However, after foreshock bubbles connect to the bow shock, the downstream boundary merges with the remainder of the bow shock. Remaining ions and those that are later trapped in the core could gain energy during this time interval. Higher ion energy than that in the background foreshock can thus be observed if the energy gain during this process is larger than the energy loss. In Chapter 6, I will show the evidence of this acceleration process.

Next, we examine how the solar wind speed affects the non-solar wind ion energy. Figure 4.4a, b, shows that non-solar wind ion mean kinetic energy and mean thermal energy inside the core increase with solar wind kinetic energy. We can also see that the Kappa index decreases with increasing solar wind kinetic energy (Figure 4.4c). Thus, the solar wind speed can

dramatically affect the ion energy. This is probably because faster solar wind speed can give higher foreshock ion energy, which is the initial energy of source particles for foreshock transients. Additionally, mixed thermalized solar wind ions may make a partial contribution to the correlation between the mean thermal energy and the solar wind kinetic energy (Figure 4.4b).

If we plot the ratios of our energization estimates inside the core over those in the background foreshock (the normalized energization estimates) against the solar wind kinetic energy (Figure 4.4d, e, f), we can see that the correlation that held for the non-normalized estimates disappears except for the Kappa index. There are two possible explanations for this lack of correlation. The first is that high energy ions could leak from foreshock transients and affect the ion energy in the background foreshock (see Chapter 6). The gyroradii of ions with an energy of several keVs can be thousands of km, i.e., comparable to the boundary thickness of foreshock transients (hundreds to thousands of km). Once foreshock ions have been accelerated to several keV or tens of keV, they could easily leak out and increase our estimated background ion energy. This effect may also help explain why in most of our events, ion energy inside the core is lower than that in the background foreshock. The second possible explanation for the lack of correlation may be that the ion energy loss in the core is related to (proportional to) the transient's expansion speed, which may also be proportional to the solar wind speed. The initial ion energy is also proportional to the solar wind speed. Thus, this may also prevent the ratio of these two quantities from exhibiting a clear correlation to the solar wind speed.

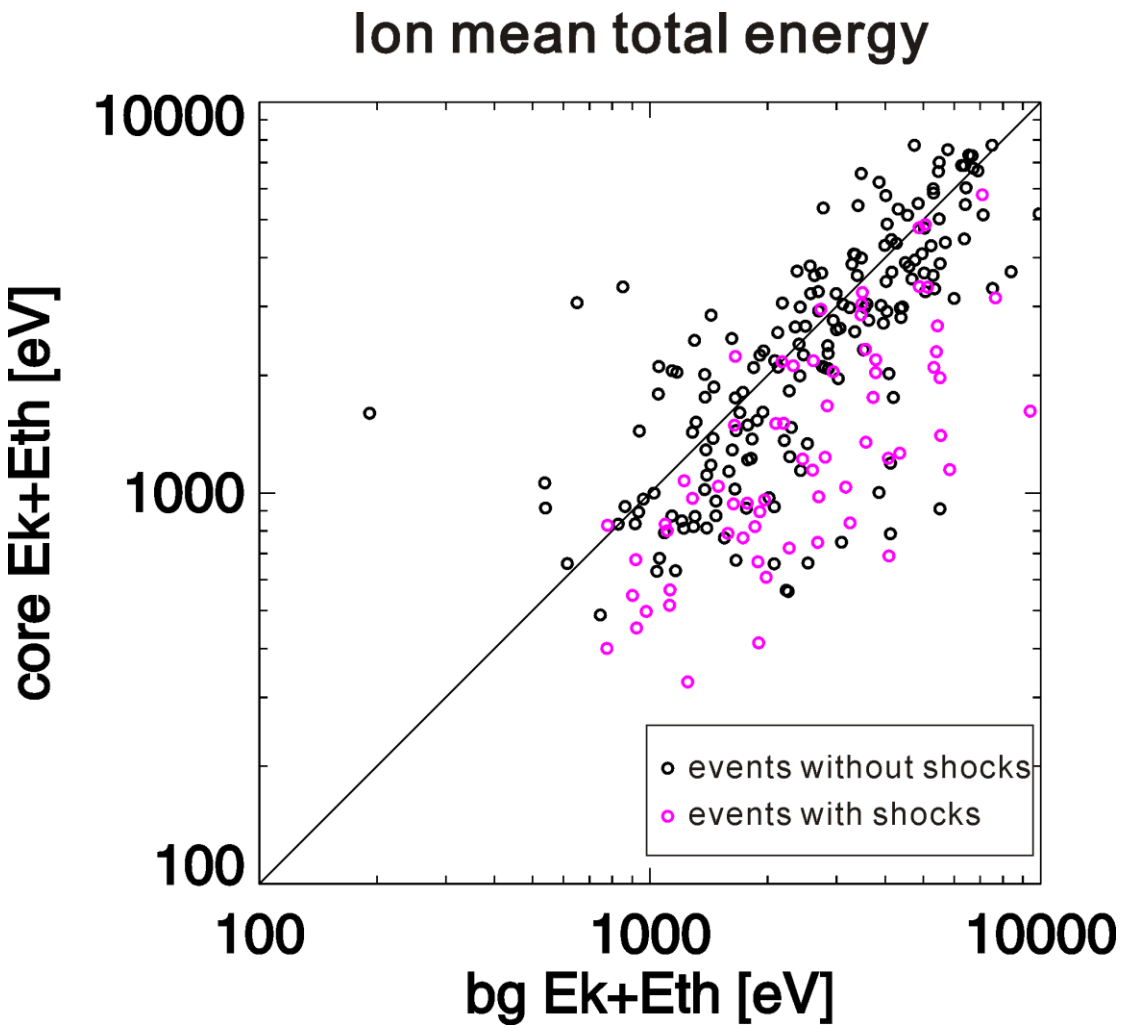

Figure 4.3. *Non-solar wind ion mean total energy in the core vs in the background foreshock. Pink indicates events with a shock-like structure. Seventy percent of events have ion mean total energy smaller than that in the background foreshock (circles below the diagonal). Almost all the events with shock-like structures (pink circles) are below the diagonal.*

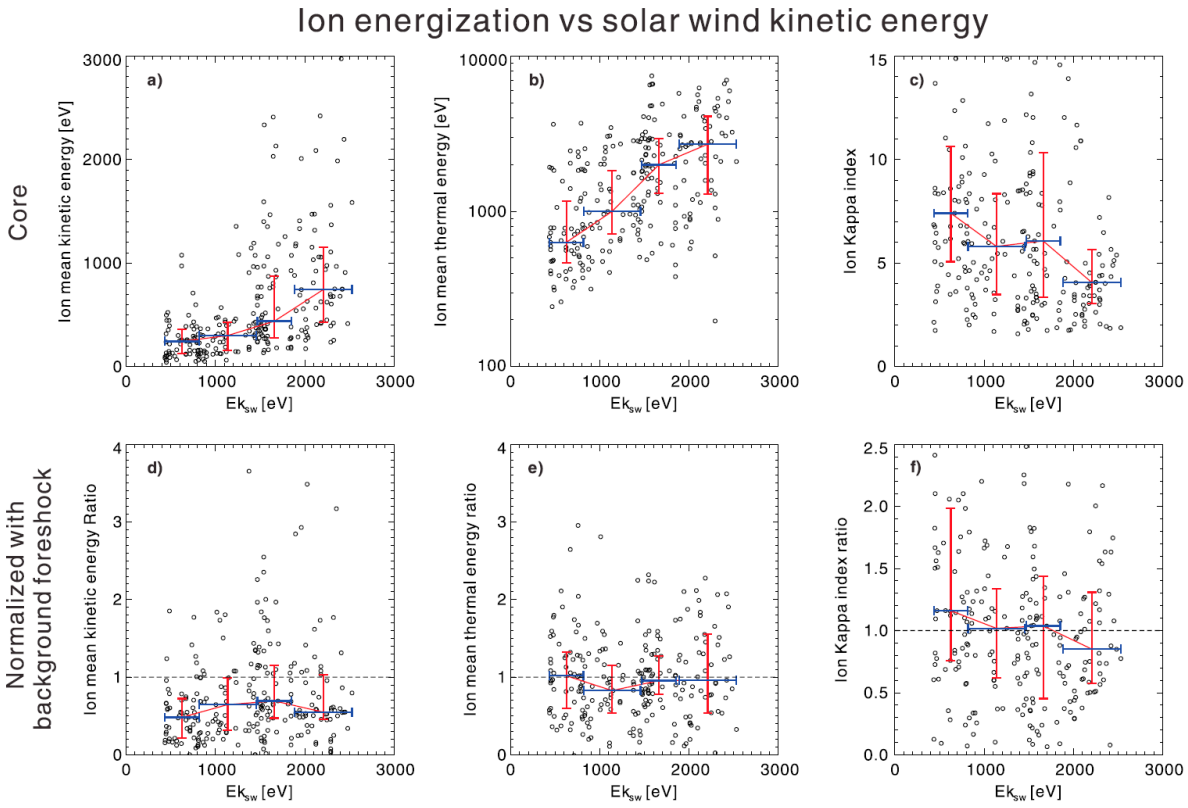

Figure 4.4. *Non-solar wind ion energization estimates in the foreshock transient core plotted against the solar wind kinetic energy: mean kinetic energy (a); mean thermal energy (b); Kappa index of the phase space density distribution (c). Normalized estimates (d, e, f, respectively) are the ratios of these quantities to the same quantities in the background foreshock. Horizontal dashed line in (d, e, f) is at ratio = 1. Red line indicates the median and quartiles (25% and 75%). Dark blue horizontal bars indicate the data bins in which median and error bars are calculated (each data bin contains an equal number of data). A positive correlation between ion energization in the core and the solar wind speed can be seen in (a, b, c), but the correlation is barely seen after normalizing mean kinetic energy and mean thermal energy to those in the background foreshock (d, e).*

4.4 Summary

I have shown that the most important role of energetic (heated) ions in the core is to enable formation and expansion of foreshock transients, which create an environment for particle acceleration. Even though ions must give up some of their energy so that foreshock transients can fully form and expand, net energization over and above the background is ultimately occurring when the core collapses onto the bow shock. The net energization can be observed occasionally (30%) for ions, and almost always (90%) for electrons. Thirty percent of foreshock transients have maximum electron energies of more than 25 keV.

Solar wind speed is the parameter having the highest positive correlation with (and likely the dominant factor controlling) the energization. It is positively correlated with all our ion and electron energization estimates, likely because higher solar wind speed can provide a particle source of higher initial energy. The ratio of our electron energization estimates (except the Kappa index) in the core to the same estimates in the background foreshock is also correlated with solar wind speed, suggesting that solar wind speed can also increase electron acceleration efficiency. By comparing other solar wind parameters during our transient events with the same parameters computed from the entire time interval of our study, we found that weak magnetic field strength and fast solar wind speed favor formation of foreshock transients.

Next I discuss the role of ions and energy transfer during the lifetime of a foreshock transient using hot flow anomalies and foreshock bubbles as examples. Foreshock ions encounter and pass through the solar wind discontinuity responsible for formation of hot flow anomalies or foreshock bubbles. During this process, part of their kinetic energy is converted into thermal energy. Hot, concentrated foreshock ions create a high thermal pressure core that starts to expand. During the expansion, the core's increasing size means that work is done to the surrounding cold,

solar wind plasma. Therefore, the overall energy of concentrated ions in the core should decrease. Some of these ions are expected to leak out, some to remain inside, and new foreshock ions are expected to continue being trapped from outside and lose some energy to support the expansion. Because the expansion speed is normally lower than the solar wind speed, the upstream boundary should move towards the bow shock at a speed slower than the solar wind speed. In the spacecraft frame (Earth frame), ions in the core will gain energy by being reflected at the moving upstream boundary. However, the reflection at the downstream boundary, which moves towards the bow shock faster than the upstream boundary, will make them lose more energy than they gain by reflection at the upstream boundary. This is another way to explain how overall ion energy decreases. When the foreshock transient starts to connect to the bow shock, the volume of the core begins to decrease. Both ions and electrons no longer reflect and lose energy at an earthward-moving downstream boundary; that boundary is now merged into/transmitted through the bow shock. Rather, they reflect between a fixed or even sunward-moving boundary, the bow shock, and an approaching upstream boundary of the foreshock transient, and gain energy. This process releases energy that had been stored during the foreshock transient formation and expansion process from early thermalized, concentrated ions. Therefore, as far as particle energization to suprathermal energies is concerned, the most important role of ions is to establish the structure of foreshock transients and store their energy inside the structure so it can later on accelerate electrons and some ions as it collapses onto the bow shock.

Almost all foreshock transients convect with the solar wind and finally merge into the bow shock. Electron energy increases were observed in more than 90% of our events. However, since both electrons and ions can gain energy during this process (by reflecting at the earthward-moving upstream boundary and the bow shock), it is not immediately obvious why ions do not

exhibit energization in most of our events. One possible reason is that electrons move much faster than ions, so electrons can be accelerated through many more reflections than ions during the same timescale (e.g., 1 min) of the foreshock transient's collapse. Electrons could also be accelerated through some other mechanisms, e.g., by whistler mode waves. Thus, we hypothesize that the ion energy increase may not be strong enough to compensate for the energy loss during the expansion process. The second possible reason is the larger gyroradii of energetic ions, which make them more likely to leak out of the core than electrons of comparable energy. This leakage will lower the energy in the core and increase the energy in the background foreshock. (The leaked electrons, on the other hand, can move quickly away from the local neighborhood of the foreshock transient, and thus do not have the opportunity to change the average electron energy in that neighborhood.) The third possible reason is that we could be underestimating the ion energies in the core due to mixing with some thermalized solar wind ions.

We have shown that the solar wind speed is critical to energization. Both the electron energization estimates and their normalized counterparts are correlated with the solar wind speed. Thus, the solar wind speed can increase not only the initial energy of a particle source but also the efficiency of the electron acceleration process. But how does solar wind speed affect the acceleration process? One candidate acceleration mechanism is Fermi acceleration [e.g., Omidi et al., 2010], in which electrons bounce between converging boundaries: the earthward-moving upstream boundary of the foreshock transient and the bow shock. In this case, the electron energy is related to the initial distance between the two boundaries, i.e., the size of the foreshock transient when it connects to the bow shock. Because a faster solar wind speed can make the transients expand farther, resulting in higher compression between walls during the transient's

collapse, this is one possible way for the solar wind speed to affect the electron acceleration process. To further investigate this scenario and reveal the exact acceleration mechanism, case studies and simulations need to be applied. We do this in the next two chapters.

Chapter 5. Electron acceleration

In Chapter 4, I showed that almost all foreshock transients can accelerate electrons, suggesting that electron acceleration by foreshock transients may contribute to parent shock acceleration. In this chapter, I will explain how foreshock transients accelerate electrons. Fermi acceleration is one possible acceleration mechanism [e.g., Omidi et al., 2010]. When a foreshock transient is connected to the bow shock, its core is bounded by its earthward-moving boundary and the bow shock. Electrons inside the core can be accelerated by bouncing between the converging foreshock transient boundary and the bow shock. In Sections 5.1 – 5.3, I will show the evidence of such a process by comparing our observational results with an analytical model and test particle simulations. However, such a mechanism cannot explain relativistic electrons observed by Wilson et al. [2016] and in the statistical study shown in Chapter 4. In Section 5.4, I will demonstrate that a two-step betatron acceleration can account for such energetic electrons.

5.1 Electron Fermi acceleration: an analytical model

Fermi acceleration, including diffusive shock acceleration [e.g., Drury, 1983], is an important acceleration mechanism in the universe, especially for cosmic rays [e.g., Fermi, 1949; Helder et al., 2012]. Particles reflected by a moving reflecting boundary can gain energy from it, but the energy gain from a single particle bounce is small. If particles experience reflection many times, however, the energy increase will be much more significant. The simplest illustrative example is a particle bouncing between two approaching walls. If L is the distance between the walls, v_x is the particle speed normal to the walls, and U is the converging speed of the walls, then each complete bounce (wall-to-wall and back) lasts $\Delta t = 2L/|v_x|$ when $U \ll |v_x|$ and results in $\Delta|v_x| = 2U$. We have $\Delta L = -U\Delta t = -U \cdot 2L/|v_x|$ and obtain

$$\frac{\Delta L}{L} = -\frac{2U}{|v_x|} = -\frac{\Delta|v_x|}{|v_x|}. \quad (5.1)$$

We then obtain $|v_x| \cdot L = |v_{x0}| \cdot L_0$ (similar to the conservation of the second adiabatic invariant in a magnetic mirror). As the distance decreases, the particle energy normal to the wall increases, causing anisotropy.

Observations of foreshock transients, however, show that electrons are nearly isotropic [e.g., Wilson et al., 2016]. Low-frequency waves observed in the foreshock [e.g., Wilson, 2016] could account for pitch-angle scattering. As electrons are moving much faster (thousands of km/s) than these low-frequency waves (which move at or around the Alfven speed, ~10s of km/s, in the core, where bulk flow velocity is very small), such waves can be treated as static fluctuations relative to electrons (the electric field fluctuations are nearly zero, and thus there is no energy transfer between waves and particles). When electron gyroradii are comparable to the length scale of these fluctuations, their pitch angles can be scattered (by $\sim \delta B/B$ per wave length) [e.g., Longair, 1981; Drury, 1983]. If the wave phases are random, magnetic fluctuations can cause stochastic changes in the pitch angles [e.g., Longair, 1981; Drury, 1983]. Blandford and Eichler [1987] derived the pitch-angle diffusion coefficient of this process (assuming Alfven waves with randomly distributed wave phases) showing that it is proportional to the ratio of wave amplitude to the background field. Inside the cores of foreshock transients, the field strength is much lower than in the ambient foreshock, resulting in a larger wave amplitude ratio and thus significant scattering (tens of rad/s, using an equation from Blandford and Eichler [1987]). Strictly speaking, when the wave amplitude is comparable to the background field, linear theory fails. In Section 5.3, however, we use test particle simulations to confirm that magnetic fluctuations inside foreshock transient cores can indeed isotropize electrons.

First, we use pitch-angle scattering to modify the Fermi acceleration model from equation (5.1). When $v \gg U$, the energy increase rate becomes

$$\alpha = \frac{E}{E_0} = (\frac{L}{L_0})^{-\frac{2}{3}}. \tag{5.2}$$

The derivation is similar to that of adiabatic compression of an ideal gas except that because electrons are collisionless, there is no energy transfer between them. Next, we consider the evolution of the electron probability distribution or phase space density (PSD) in velocity space (a process that is independent of density). As this process is not a function of space (when $v \geq U$), assuming that the initial probability distribution is uniform in space, the electron distribution $f(t, \vec{r}, \vec{v})$ can be written as $f(t, \vec{v})$. Because of pitch-angle scattering by static magnetic fluctuations, $f(t, \vec{v})$ can be written as $f(t, v)$ or $f(t, E)$ by integrating over the pitch angle [e.g., Parker, 1965]. Based on Liouville's theorem (as electrons are collisionless, no energy transfer occurs between them), phase space density is conserved along the electron trajectory in velocity space, i.e., $f(t_0, E_0) = f(t, E) = f(t, \alpha(t)E_0)$, where $\alpha(t) = (L/L_0)^{-\frac{2}{3}} = [(L_0 - Ut)/L_0]^{-\frac{2}{3}}$. As α is not a function of energy, the evolution of electron probability distributions is simply a translation in energy axis in logarithmic space, i.e., $f(\log(E_0)) \rightarrow f(\log(E_0) + \log(\alpha))$, regardless of position. For an ideal gas, energy can be transferred through collisions, violating the conservation of phase space density. The evolution of the probability distribution is manifested as an isotropic temperature increase during which a Maxwellian distribution is maintained.

When $v \sim U$, the energy increase rate for one bounce becomes

$$\alpha' = 1 + \frac{2}{3}\frac{Ut}{L_0}\left(1 + \frac{U}{\langle|v_x|\rangle}\right)^2, \tag{5.3}$$

where $\langle|v_x|\rangle$ is the angular average of $|v_x|$ at a certain speed v for one bounce. Comparing α' to α in equation (5.2) $\alpha \approx 1 + \frac{2}{3}Ut/L_0$ when $\Delta L \ll L_0$ for one bounce, we see that α' is larger than α, and when $U/\langle|v_x|\rangle \to 0$ ($\langle|v_x|\rangle \gg U$), $\alpha' \to \alpha$. At low energies, the PSD value at a certain position decreases gradually with time from the lowest energy to higher energies.

To investigate whether Fermi acceleration can explain our observations, I will first determine whether the observed electron distribution evolution and energy increase rate are consistent with theory in both the high energy ($v \gg U$) and low energy ($v \sim U$) ranges. Then I will present test particle simulation results with an ideal Fermi acceleration model to compare them with our observations.

5.2 Electron Fermi acceleration: observations

Figure 5.1 shows a TH-A ([12.3, -6.5, -4.1] R_E in GSE) observation of a foreshock bubble shown in Chapter 2. From that work, we note that the foreshock bubble shock normal was [0.90, 0.44, 0.05] at TH-A, and the average shock normal speed V_n was 217 km/s in the spacecraft frame. Inside the core, magnetic fluctuations were very strong (Figure 5.1a): the strength of the average magnetic field $|\langle\vec{B}\rangle|$ was only 0.88 nT ($\langle\vec{B}\rangle = [0.06, 0.88, 0.05]$ nT in GSE), whereas the mean field variation $\langle|\Delta\vec{B}|\rangle$ was ~1.6 nT. Thus, the fluctuations are strong compared to the background field and can provide very significant scattering. Unfortunately, because in 2007 THEMIS did not transmit high angular resolution electron distributions routinely in fast-survey mode, we can only explore the anisotropy of electron distributions in two other events from 2008; in those events we find that the electrons are indeed isotropic.

Inside the core, the normalized PSD spectra show a gradual increase in electron energy (Figure 5.1d). (Although we cannot calculate the spectra in the plasma rest frame because of the

low electron angular resolution in 2007, the bulk velocity is very small in the core (Figure 5.1e), and therefore the use of the spacecraft frame does not cause significant differences.) The omni-directional spectra reveal the energy evolution for a fixed PSD value. Using equation (5.2) and the method described in Section 5.1, we calculated the expected energy evolution at certain initial energies (we used 60 eV and 150 eV as examples) as a function of time (the two black lines in Figure 5.1d). We can see that the black lines match the constant flux contours very well (between red and yellow and between yellow and green, respectively), indicating that our observation is consistent with equation (5.2) if phase space density is conserved. Additional quantitative comparisons will be presented later in this paper.

For further clarification, Figure 5.2a shows the evolution of the density-normalized electron distribution (from black to green, same time interval of black lines as in Figure 5.1d). Electrons follow a kappa distribution. At initial energies above 60 eV (electron thermal speed $v \approx 21V_n$), electron distributions translate in the logarithmic axis of energy consistent with expectations from theory for high energy electrons ($v \gg V_n$; the power law slope of the high energy tail is almost constant, ~4.5). At initial energies below 30 eV ($v \approx 15V_n$), on the other hand, the electron phase space density decreases gradually with time beginning from lower energies, which is consistent with our expectations for low energy electrons ($v \sim V_n$).

Additionally, the energy increase rate of low energy electrons α' should be greater than that of high energy electrons, α. For example, for 10 eV electrons, $\alpha' = 1 + 0.9Ut/L_0 \approx [(L_0 - Ut)/L_0]^{-0.9}$. Because electron temperature is dominated by low energy electrons, we can confirm this faster increase rate from the temperature increase rate (determined by α' and the distribution of low energy electrons). Indeed, as seen in Figure 5.1c, the temperature increases as

$[(L_0 - Ut)/L_0]^{-1}$ (red line), faster than the -2/3 rate (black line) from equation (5.2), which is consistent with our expectations.

To further quantify the difference between the data and equation (5.2), we calculate the relative error between them, defined as $\sigma = \sqrt{\sum(\log(y_i) - \log(Y_i))^2 / n(n-1)}$, where Y_i is the measured energy of certain PSD values at different times, y_i is the energy calculated from equation (5.2) with initial energy determined by minimizing the relative error, and n is the number of data points indexed from 0 to $n - 1$. Figure 5.2b shows the relative error as a function of initial energy. Because the PSD evolution of low energy electrons does not follow equation (5.2), the relative error is very large below 30 eV. Between 30 eV and 60 eV, the relative error gradually decreases as equation (5.3) gradually approaches equation (5.2). Between 60 eV and 2 keV, the relative error is around 3%, a good match. Above 2 keV, the relative error becomes large again because the electron flux is approaching ESA's detection threshold, and the statistical noise from the low count rates increases against the relative error. Figure 5.2c, d shows two comparisons between equation (5.2) and the energy evolution of certain PSD values at initial energies ~60 eV and 400 eV, respectively, which demonstrate good agreement.

If this is indeed Fermi acceleration, the energy evolution of high energy electrons should be the same at different locations within the core. Thus, we compare the normalized PSD evolution at different spacecraft (Figure 5.3). In this event, the other four spacecraft (TH-B through TH-E) were close to each other and about 1 R_E away from TH-A in the GSE-Y direction. Because of their finite separation (ΔY~0.2 R_E − 1.2 R_E in GSE), they observed different parts of the foreshock bubble at different times, as evidenced by the magnetic field signatures (Figure 5.2a, b). We plot the same energy-time relation in Figure 5.3d-g as in Figure 5.1d, 5.3c except that the

end times differ because the core terminates at different times at different locations (spacecraft). All these lines follow constant flux contours (between red and yellow and between yellow and green). Thus, the energy evolution is almost identical regardless of the specific initial energy considered in the high energy (>60 eV) range. Therefore, our observations are consistent with the Fermi acceleration model.

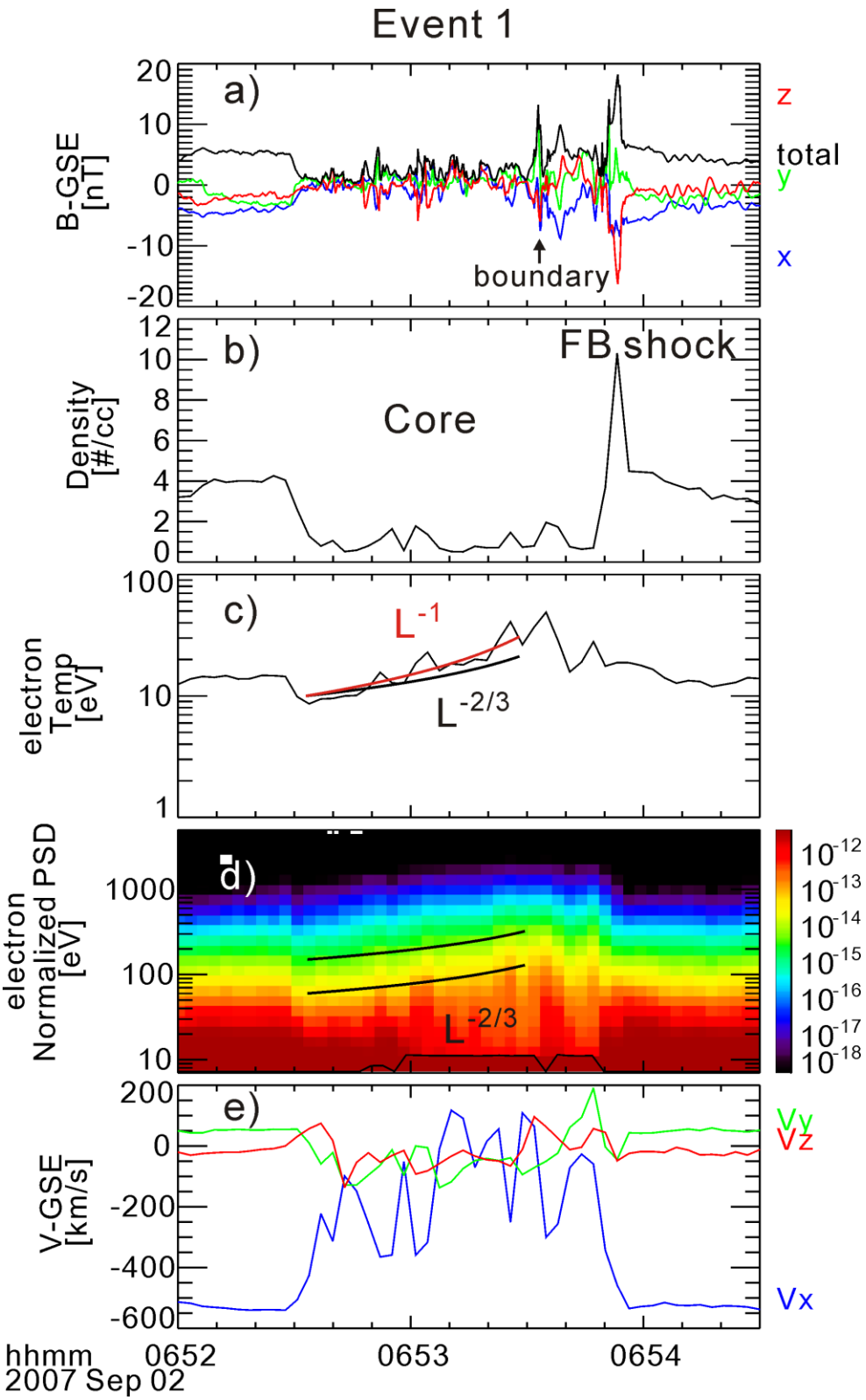
Event 1
a)
B-GSE [nT]
20
10
0
-10
-20
z
total
y
x
boundary
b)
FB shock
Core
Density [#/cc]
12
10
8
6
4
2
0
c)
electron Temp [eV]
100
10
1
L-1
L-2/3
d)
electron Normalized PSD [eV]
1000
100
10
L-2/3
10-12
10-13
10-14
10-15
10-16
10-17
10-18
e)
V-GSE [km/s]
200
0
-200
-400
-600
Vy
Vz
Vx
hhmm
0652
0653
0654
2007 Sep 02

Figure 5.1. *TH-A observations of a foreshock bubble. From top to bottom are: (a) magnetic field components in GSE coordinates (XYZ, total in blue, green, red, black, respectively); (b) ion density; (c) electron temperature; (d) electron phase space density spectra normalized by electron density* $(\#/(km/s)^3)$*; (e) ion bulk velocity in GSE coordinates (XYZ in blue, green, red, respectively). Black lines in (d) are the calculated energy increase at initial energy 60 eV and 150 eV using equation (5.2). They match the contour of spectra (between red and yellow and between yellow and green). Electron temperature (c) increases along* L^{-1} *(red line) rather than* $L^{-2/3}$ *(black line).*

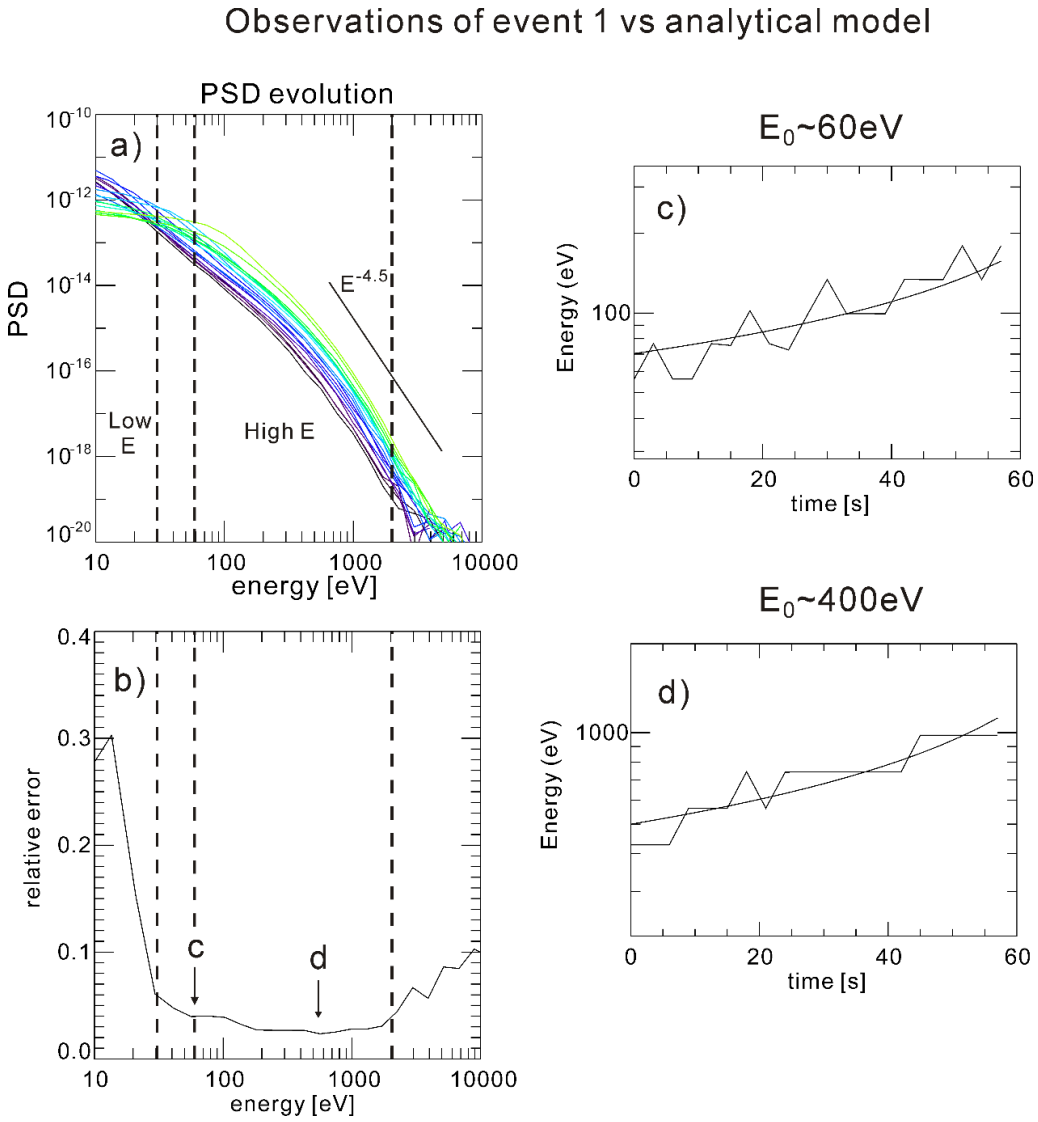

Figure 5.2. *Comparison of observations to an analytical model. (a) the evolution of normalized electron PSD in the core (from black to green; the same time interval as the black lines in Figure 5.1d, [06:52:33, 06:53:28] UT). The spacecraft potential is subtracted at each time. The unit of PSD is* $\#/(km/s)^3$. *At energies above 30 eV, the distribution evolution is nearly a translation of the logarithmic axis of energy. (b) the relative error between data and equation (5.2) (~3% between 30 eV and 2 keV). (c) and (d) comparison of observed energy evolution of certain PSD values to equation (5.2) at initial energies of 60 eV and 400 eV, respectively. They match well.*

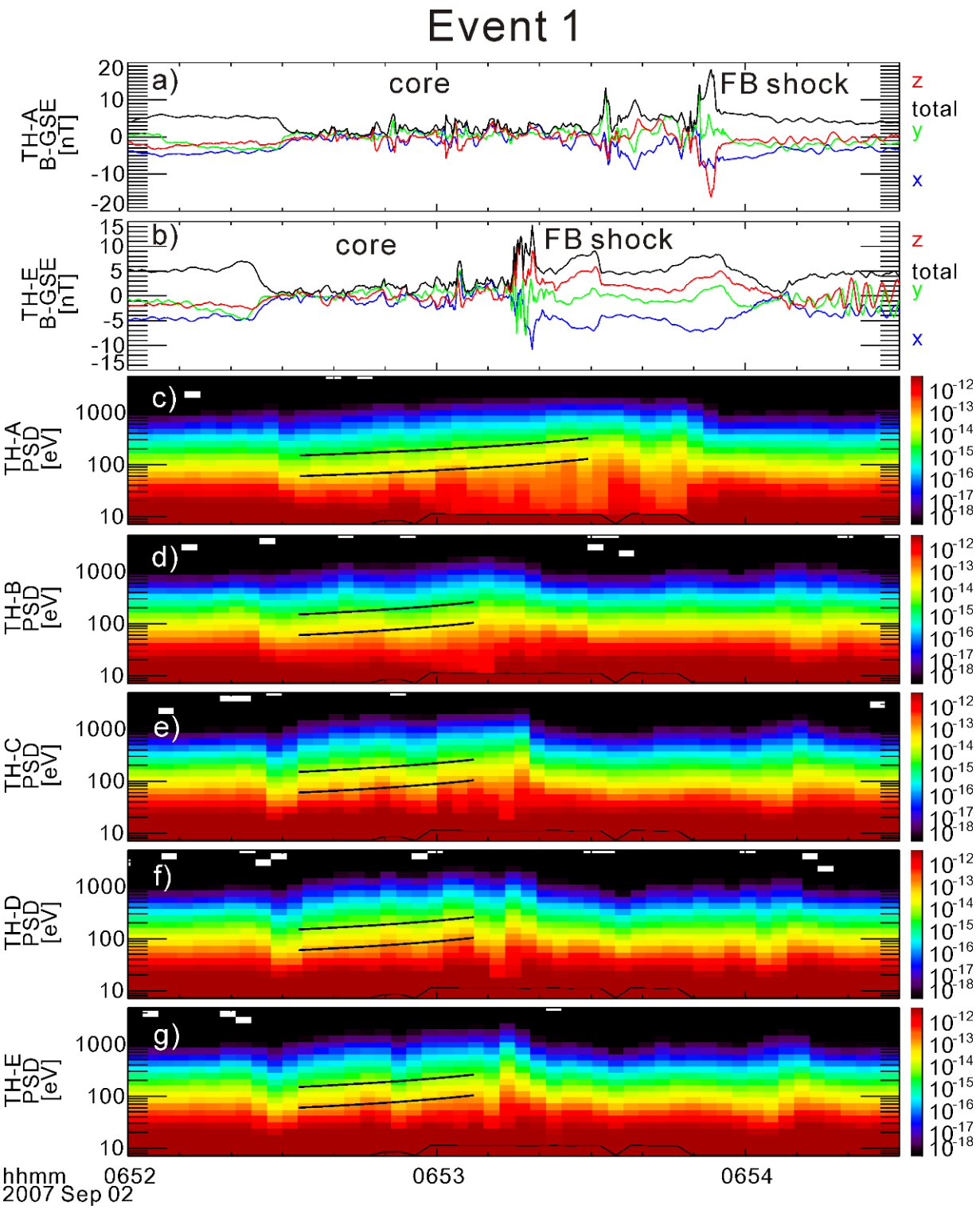

Figure 5.3. *Observations from all five THEMIS spacecraft. From top to bottom are: (a, b) TH-A and TH-E observations of magnetic field components in GSE coordinates (XYZ, total in blue,*

green, red, black, respectively); (c-g) TH-A, TH-B, TH-C, TH-D, and TH-E observations of electron normalized PSD spectra. Black lines in (c-g) are identical to those in Figure 5.1d except the end time. Electron distribution evolution is almost identical at five locations at high energies (>60 eV).

5.3 Electron Fermi acceleration: simulations

To further confirm the Fermi acceleration scenario in the presence of magnetic fluctuations, we employed test particle simulations (see Appendix b), comparing the spectral evolution and energy increase rate of the simulated electron distributions with observations.

Our one spatial- (three velocity-) dimension simulation domain is 2 R_E long, with the magnetosheath at $X_{sim} = 0.0 - 0.5\ R_E$ having a magnetic field $B_z = 20$ nT and the bow shock at $X_{sim} = 0.5\ R_E$. Electron trajectories are traced in prescribed electromagnetic fields, with both DC and AC components in time and space. The foreshock transient boundary is initially at $X_{sim} = 1.5\ R_E$ and moves towards the bow shock at a speed $U = 100$ km/s. The region beyond $X_{sim} = 1.5\ R_E$ is the foreshock transient sheath in which the magnetic field is $B_z = 10$ nT. Therefore, a convection electric field $E_y = -1$ mV/m consistent with the velocity U is introduced in the foreshock transient sheath. Between the two boundaries, $0.5\ R_E < X < 1.5\ R_E$, is the foreshock transient's core region.

Based on previous observations and simulations, the magnetic field inside the core fluctuates considerably [e.g., Omidi et al., 2010; Turner et al., 2013]. Such fluctuations are also part of our aforementioned transient event selection criterion. Therefore, we impose magnetic fluctuations inside the simulated core, as well, to study their effect on electrons. The fluctuations are prescribed as:

$$\delta B_{x,y,z} = \sum_{N=N_0}^{N_1} \delta B_N \cos\left(\frac{2\pi N x}{L_0} + \varphi_{x,y,z}^{N}\right), \tag{5.4}$$

$$\delta B_N = \tilde{B}(N/N_0)^{-1.2},\ N = N_0, N_0 + 1, \dots, N_1. \tag{5.5}$$

Here $L_0 = 1\ R_E$ is the initial length of the core in the x direction. We choose $N_0 = 100$, $N_1 = 1000$, $\tilde{B} = 0.2$ nT, and $\varphi^N_{x,y,z}$ are the random phases of various modes between 0 and 2π (independently different in the x, y, and z directions). Equation (5.5) is based on the observations, assuming that the dispersion relation of low-frequency waves is linear. (Note that δB_x cannot be divergenceless as this is a 1-D simulation.) As the low-frequency wave speed (tens of km/s) is much smaller than the electron speed (thousands of km/s), we do not include wave propagation in this 1-D model. Thus, the wave component of the electric field is zero (it is treated as negligible).

A total of 50,000 electrons are put into the above electromagnetic fields and advanced in time. The electron initial temperature is $T_0 = 10$ eV, and the initial flow velocity is zero. We use a time step $\Delta t = 2 \times 10^{-6}$s. The simulations have 2×10^7 steps, i.e., 40 seconds, during which the foreshock transient boundary moves 4000 km towards the bow shock.

To quantify the electron spectral evolution and compare it with theory and observations, we show the time evolution of core electrons with an initial kappa distribution in fluctuating fields (case 3). We adopt $\kappa = 3.5$, which is consistent with previous THEMIS statistics (Chapter 4). Figures 5.4a and 5.4b show the electron velocity distributions at $t = 40$s. As in case 2, the electrons inside the core are Fermi-accelerated by bouncing between the approaching foreshock transient boundary and the bow shock while being scattered by the fluctuations to be isotropic. Compared to a Maxwellian of equivalent temperature, a kappa distribution has more high energy electrons, which are difficult for short wavelengths fluctuations to scatter and therefore retain a weak anisotropy (evident in Figure 5.4b). Note that our distributions include all electrons inside the (simulated) core, but a spacecraft can only observe one point. This difference, however, will

not cause trouble because this process is not a function of space in the high energy range (the simulated distributions from a random spatial interval in the core do not show clear differences, which is consistent with Figure 5.3).

According to the evolution of energy spectra (Figure 5.4d), the electrons are accelerated from thermal to suprathermal energies, very similar to observations (Figure 5.1d). Using equation (5.2) we calculated the theoretical energy evolution at initial energies 50 eV and 100 eV (two black lines in Figure 5.3d) that increase to 100 eV and 200 eV, respectively, based on the evolution of the simulated wall separation in 40 s. The theoretical energy evolution matches the simulated constant phase space density spectral contours, confirming our simple Fermi acceleration model in the presence of strong fluctuations.

Next we examine in greater detail our physical picture of the energy range over which the above simple Fermi model applies. Towards that end, in Figure 5.5, we show phase space density versus energy temporal evolution in the same format as in Figure 5.2. The distribution evolution (from black to green) in Figure 5.5a looks very similar to observations (Figure 5.2a): above ~50 eV ($v \approx 42U$), the electron PSD has a spectral evolution that results from a logarithmic energy-translation of the initial spectrum. The power-law slope of the high energy tail set by the initial kappa distribution is almost constant, ~4. Below 20 eV ($v \approx 27U$), the electron PSD decreases with time; 20 eV to 50 eV is a transition range from equation (5.3) to equation (5.2). As in the observations shown in Figure 5.1c, the temperature dominated by low energy electrons ($v \sim U$) increases faster than equation (5.2), following the $(L/L_0)^{-1}$ law (Figure 5.4c).

As in observations (Figure 5.2c, d), in Figure 5.5c, d, we compare the theoretical (equation

(5.2)) to the modeled energy evolution for fixed PSD values corresponding to ~50eV and 100eV, respectively, for case 3. The good match between simulations and theory shows that Fermi acceleration in the presence of isotropization from strong fluctuations is well described by equation (5.2). The relative error between theoretical (equation (5.2)) and simulated energy profiles such as those was plotted as a function of the initial energy in Figure 5.5b, as was done for observations (Figure 5.2b). The relative error is very large below 20 eV. Between 20 eV and 50 eV, it decreases gradually as electron behaviors gradually approach those described by equation (5.2). The relative error is around 0.5% between 50 eV and 200 eV. It becomes larger above 200 eV because high energy electrons are not well scattered in the simulation (more anisotropy in x results in a shorter bounce period, causing a larger energy increase rate), and the small number of particles at high energies results in increased statistical noise (similar to the error from low counting statistics in the observations). As the simulations are consistent with theoretical expectations and observations, we conclude that electron Fermi acceleration is the principal physical mechanism responsible for electron acceleration in these events.

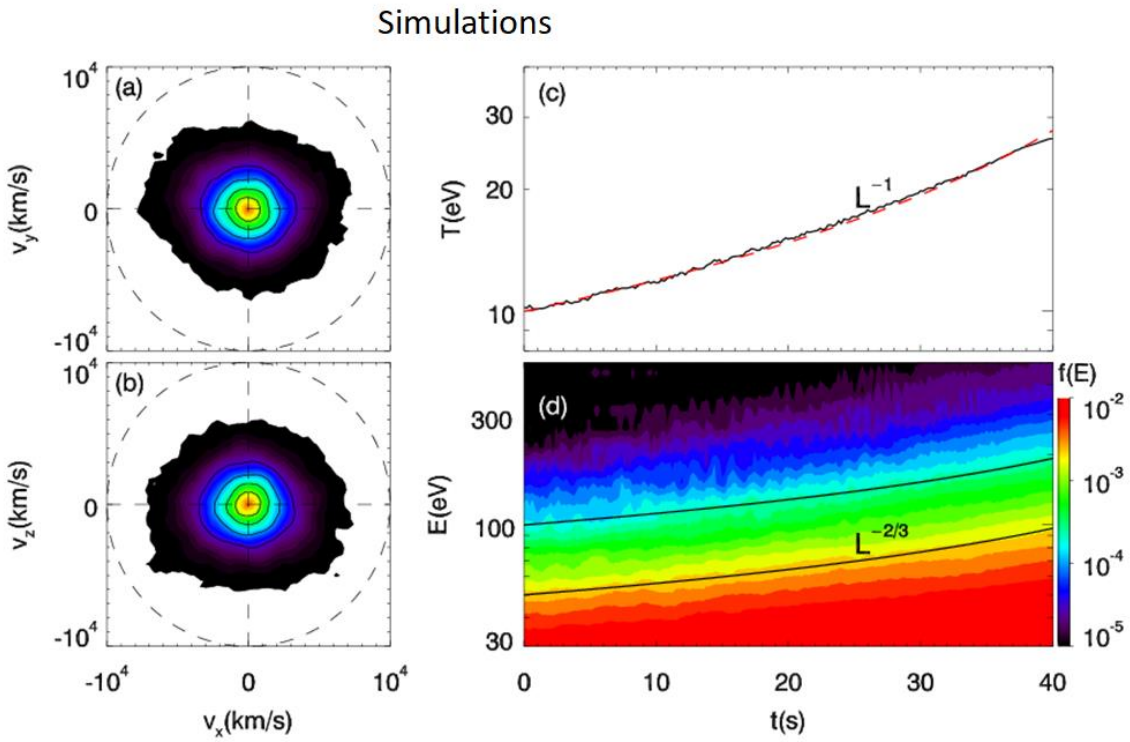

Figure 5.4. *(a) and (b) Electron velocity distribution functions* $f(v_x, v_y)$ *and* $f(v_x, v_z)$ *calculated inside the core at* $t = 40s$ *for case 3 (kappa distribution and fluctuations). They are nearly isotropic. (c) Electron temperature evolution fitted with* $T/T_0 = (L/L_0)^{-1}$ *(red dashed line). (d) Electron energy spectra evolution* $(\#/eV)$*. Two black lines represent the calculated energy evolution from equation (5.2) at initial energies* $50\ eV$ *and* $100\ eV$*, respectively. They match the spectral contour very well.*

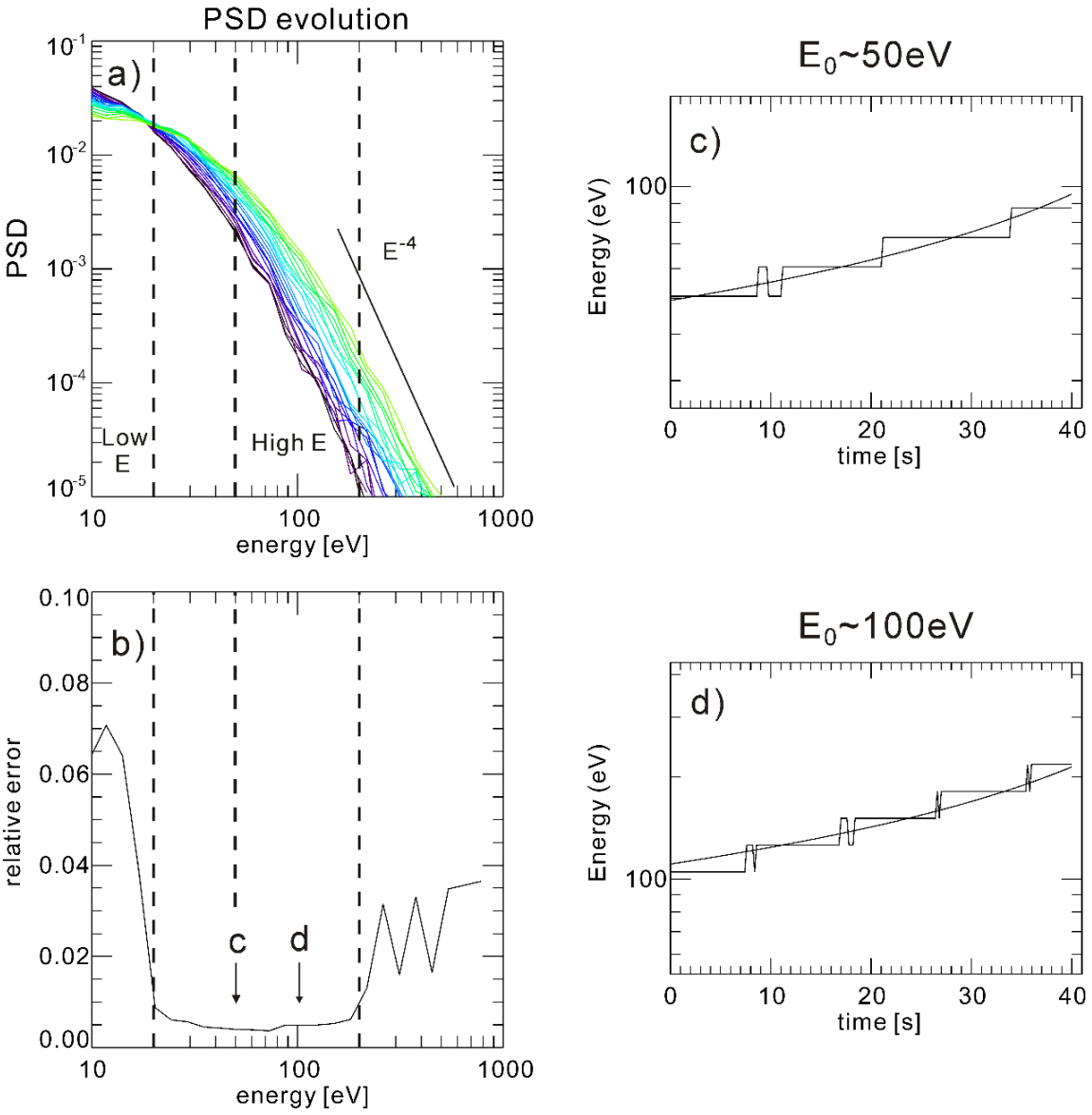

Figure 5.5. *Comparison with the analytical model in the same format as in Figure 5.2, but for simulations (case 3). The unit of PSD is* $\#/eV$.

5.4 Electron betatron acceleration

The relativistic electrons (hundreds of keV) recently observed upstream of Earth's bow shock associated with foreshock transients far exceed expectations from current theory [Wilson et al., 2016]. Because the Mach number of Earth's bow shock is low (~10), the theoretical maximum electron energy that can be accelerated is $\sim 10^{-4} M_A^2 E_0 \sim 10\ keV$, where M_A is Mach number and E_0 is electron rest energy [Treumann, 2009]. Using hybrid simulations and observations, here we address this apparent inconsistency.

We first trace how field lines of a foreshock bubble typically evolve in hybrid simulations (Figure 5.6 and Movie S3) to infer how electrons interact with foreshock transients. In a representative case of foreshock bubble generation, a solar wind rotational discontinuity which rotates the field by 40° is modeled to convect towards Earth. Initially, the solar wind magnetic field is uniform. As expected from previous works, the rotational discontinuity will trap and thermalize backstreaming foreshock ions, enhancing the local thermal pressure and distorting the magnetic field there. The enhanced thermal pressure expands the plasma and transports the associated magnetic flux sunward, causing field lines to straighten inside the hot region and become more bent sunward of it (Figure 5.6a). As this sunward expansion is faster than the local fast-wave speed, a foreshock bubble sheath/shock with an enhanced field (Figure 5.6b) forms around the hot core with the weak field. As the foreshock bubble continues to evolve, field lines in the core continue to pile up from the center of the core (expansion region in Figure 5.6c) to the surrounding region (compression region in Figure 5.6c). Using THEMIS observations, I will show that the observed foreshock bubble has a similar field line evolution. By analyzing the observed evolution of electron phase space density, I will demonstrate that electrons can be

accelerated to relativistic energy through betatron acceleration while they are piling up with field lines.

Using THEMIS spacecraft observations at Earth's bow shock, we investigate foreshock transient events associated with relativistic electrons in particle burst mode. Here I present one example in detail (Figure 5.7). As a foreshock bubble convects with the solar wind, a spacecraft first observes a hot, tenuous core, then a foreshock bubble sheath – this is what is seen in this event, too (Figure 5.7). Motivated by our simulations clearly showing the flow diverging sunward and sideways from the core center, we separate the core into two regions, an expansion region in which sunward flow has positive divergence ($dV_n/dn \sim dV_x/dx > 0$, where n is the foreshock bubble shock normal; Figure 5.7d) and a compression region in which sunward flow has negative divergence ($dV_n/dn < 0$). Field strength (Figure 5.7a) and density are low (Figure 5.7b) in the expansion region and grow stronger in the compression region. These two regions are consistent with our simulation (see Figure 5.6c).

Inside the core, the electron phase space density (PSD) contour (dotted line in Figure 5.7g) is very well correlated with the scaled field strength (solid line), suggesting betatron acceleration. Such trends can also be seen in the SST spectra (Figure 5.7f). Figure 5.8a shows the perpendicular PSD in different regions. If we compare the perpendicular PSD in the expansion region (black), compression region (red), and the region where the field strength is strongest (green), we see that their PSD acts as a shift in energy from a weak field to strong field. The maximum energy above the instrument noise level (dashed lines, defined as four times the standard deviation of noise signals) increases from ~100 keV to ~200 keV. Additionally, the relativistic electrons (hundreds of keV; by smoothing the spectra to lower the noise level, the maximum electron energy can be ~400 – 500 keV) are mainly in the compression region (Figure

5.7f). This suggests that such relativistic electrons could be betatron-accelerated while piling up with field lines from the expansion region (tens of keV) to the compression region (hundreds of keV).

Next, we investigate the source of the tens of keV electrons in the expansion region. The perpendicular phase space density in the expansion region (black) and in the foreshock bubble sheath (blue) in Figure 5.8a are nearly identical at energy above 1 keV, although the total electron density in the expansion region is much lower than that in the foreshock bubble sheath (Figure 5.7b). Such similarity can also be seen in Figure 5.7g, f. This similarity suggests that the energetic electrons in the expansion region come from the foreshock bubble sheath. Energetic electrons can freely leak from a strong field region to a weak field region along field lines until the phase space density is balanced. For low energy electrons, which follow the MHD approximation, their high density at the foreshock bubble sheath is balanced by the high thermal pressure in the core.

Next, we explain how tens to hundreds of keV electrons are generated in the foreshock bubble sheath. If we compare the perpendicular phase space density (Figure 5.8a) in the foreshock bubble sheath (blue) to that in the upstream background foreshock (magenta), we see they are well described by a factor of 2.5 energy increase across all energies. The maximum energy above the noise level (dashed lines) also increases from ~30 keV to ~100 keV (Figure 5.8a, partially due to the specific profile of the instrument noise level, denoted by the dashed lines). This suggests that energetic electrons in the foreshock bubble sheath can be betatron accelerated when they enter the sheath (spin-averaged field strength at the blue line in Figure 5.7a is ~17.5 nT) from the upstream foreshock (~5 nT). The energy shift from magenta to blue in Figure 5.8a underestimates the energy increase ratio inferred from the field increase ratio, likely

because leakage into the expansion region lowers the phase space density in the foreshock bubble sheath. Comparing the parallel phase space density (Figure 5.8b) in the compression region (red) to that in the foreshock bubble sheath (blue), we see they are nearly identical above ~300 eV. This is likely because after acceleration in the compression region, energetic electrons with small pitch angles within the loss cone can leak sunward through the foreshock bubble sheath.

The solar wind typically does not contribute tens of keV electrons to the background foreshock. If we compare the perpendicular phase space density (magenta in Figure 5.8a) with the anti-parallel phase space density (magenta in Figure 5.8c), which can roughly represent the earthward solar wind electron distribution, we see extra energetic (1 keV to 30 keV) electrons. Such electron energy is consistent with electron acceleration at Earth's bow shock. In the parallel phase space density (magenta in Figure 5.8b), we see more energetic electrons than in the perpendicular phase space density. Accelerated electrons leaked from the foreshock bubble could partially account for this difference. Additionally, we see that the electron phase space density in different regions has the same slope, ~4 (Figure 5.8). Such a slope is likely determined by the source, the background foreshock electrons. This further confirms that the relativistic electrons are accelerated from the background foreshock electrons through a two-step betatron acceleration.

From the above observational results and the field-line motion in the simulations, we conclude that the electron acceleration process proceeds as follows. In the foreshock, electrons are accelerated by the bow shock (e.g., 30 keV). When a solar wind discontinuity arrives, a foreshock bubble with a weak-field core and a boundary with an enhanced field (foreshock bubble sheath) forms. Foreshock electrons that enter the foreshock bubble sheath can experience

betatron acceleration (e.g., from 30 keV to 100 keV). Accelerated electrons at the foreshock bubble sheath can easily leak into the core along field lines (Figure 5.6b). As field lines in the core continue piling up from the center to the surroundings (compression region in Figure 5.6c), accelerated electrons that leak into the core can experience another betatron acceleration (e.g., from 100 keV to 200 keV or more). Finally, some electrons with small pitch angles can leak back through the foreshock bubble sheath along field lines. Such an acceleration process suggests that foreshock transients can further enhance the energy of electrons accelerated by the bow shock by an order of magnitude.

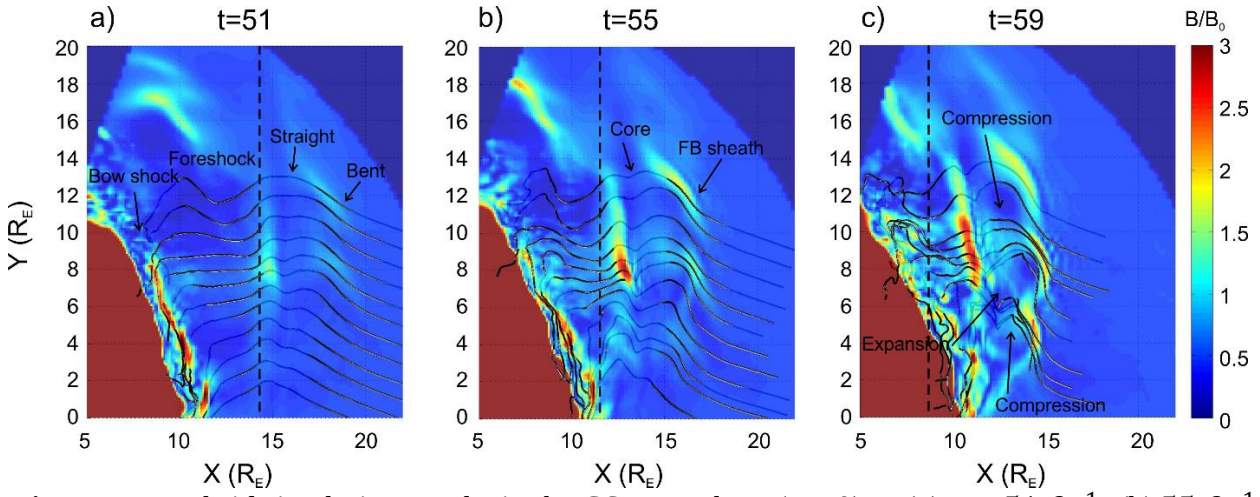

Figure 5.6. *Hybrid simulation results in the GSE-XY plane (z = 0) at (a)* $t = 51\ \Omega_0^{-1}$*, (b)* $55\ \Omega_0^{-1}$*, and (c)* $59\ \Omega_0^{-1}$*, respectively. Colors indicate normalized field strength. Vertical dashed line indicates the position of a rotational discontinuity that is convecting earthward. Curved solid lines are traced field lines. Upstream of the discontinuity, a giant plasma bubble (foreshock bubble), which is expanding faster than the local fast-wave speed, forms. It has a hot, tenuous core surrounded by a foreshock bubble sheath and shock.*

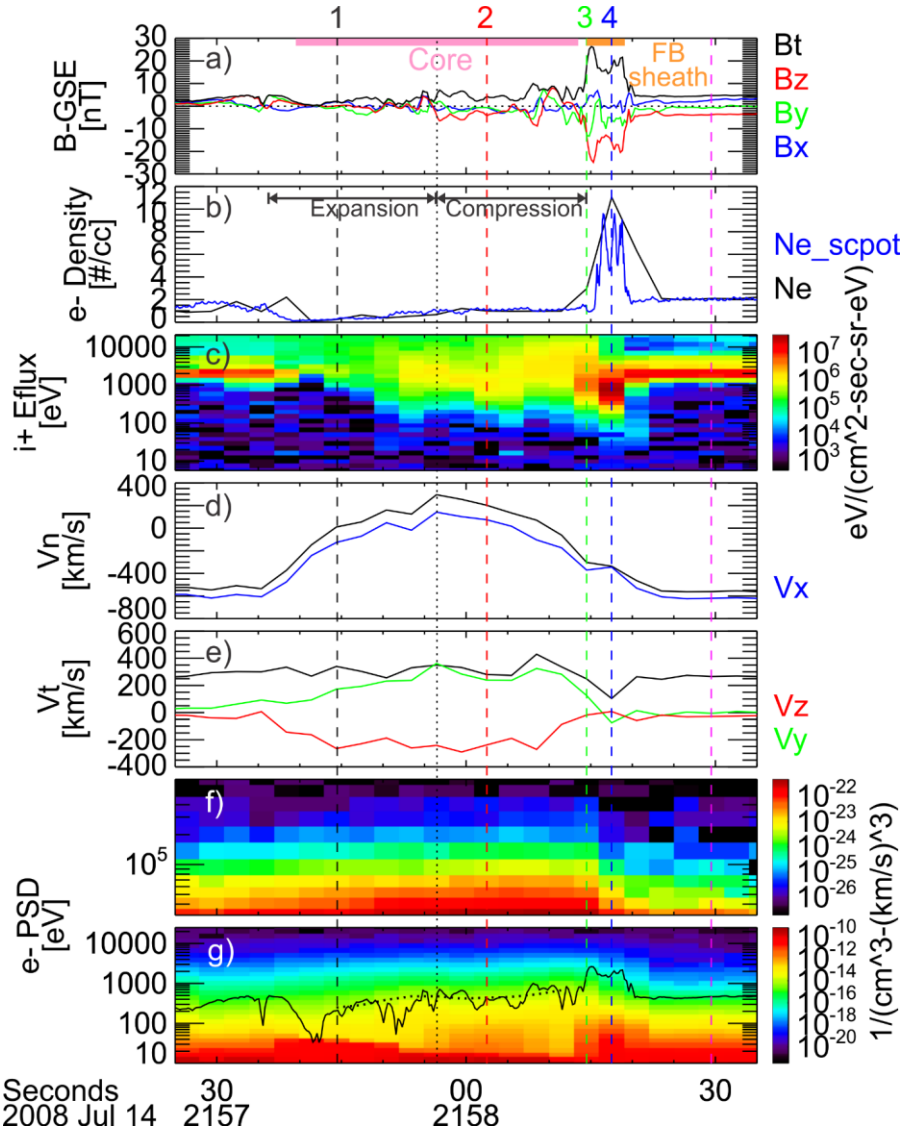

Figure 5.7. *THEMIS observations of a foreshock bubble. From top to bottom: (a) magnetic field in GSE coordinates (XYZ, total are in blue, green, red, black, respectively); (b) electron density from the onboard moment (black) and calculated from high-resolution spacecraft potential (blue); (c) ion energy flux; (d) ion bulk velocity along foreshock bubble shock normal ([0.91, 0.24, -0.31] in GSE) and ion bulk velocity in GSE-X (blue) as a comparison since foreshock bubble shock is mainly in sunward direction; (e) ion bulk velocity tangential to the foreshock bubble shock normal and bulk velocity in GSE-YZ (green and red, respectively); (f) electron*

phase space density (PSD) spectrum from 30 keV to 700 keV; (g) electron PSD spectrum from 10 eV to 25 keV. Solid line indicates the magnetic field strength scaled by a factor of 100 to compare with the PSD spectrum contour, dotted line. The foreshock bubble core and foreshock bubble sheath are labeled with a pink bar and an orange bar, respectively. The expansion region and the compression region are labeled in the core and separated by a vertical dotted line. Colored vertical dashed lines indicate the time of electron phase space density in Figure 5.8. A suggestive correlation between ion (c) and electron energy flux (g) can be seen. This is likely caused by the ion flow speed tangential to the foreshock bubble shock (e), as Vx is very small (in the spacecraft/Earth rest frame) likely because tangential flow speed implies how fast field lines pile up in the YZ direction.

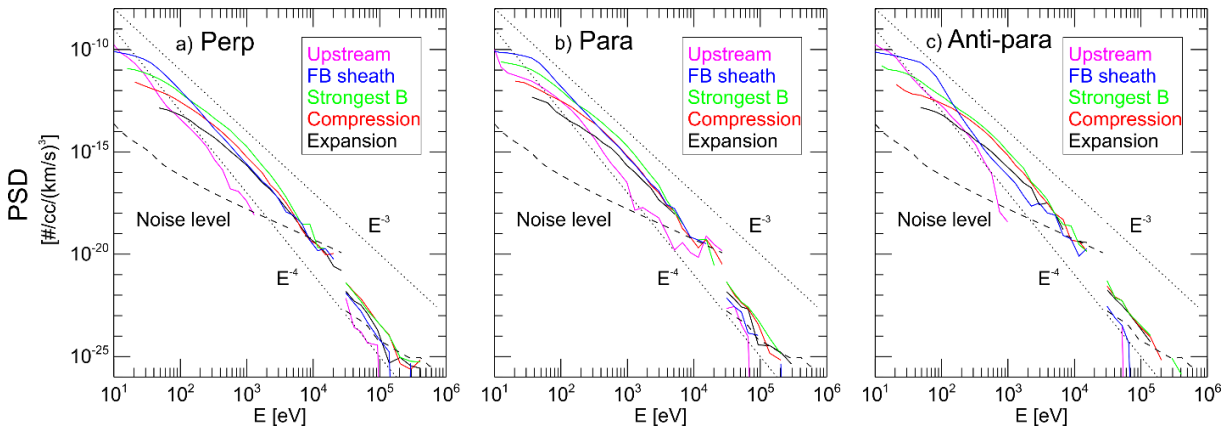

Figure 5.8. *Electron phase space density (PSD) in perpendicular (a), parallel (b), and anti-parallel (c) from ESA and SST. Different colors correspond to the colored vertical dashed lines in Figure 5.7. Dotted lines indicate the slopes, -3 and -4, respectively. Dashed lines indicate the noise levels for ESA and SST, respectively.*

5.5 Summary

By examining data from case studies and using 1-D test particle simulations, we show that Fermi acceleration is an important electron acceleration mechanism inside foreshock transient cores, which have low background field strength and strong magnetic fluctuations. In the observations, the evolution of electron distributions can be explained well by a simple Fermi acceleration model: 1. the energy increase rate of high energy electrons ($v \gg U$) is consistent with equation (2); 2. The evolution of distributions follows $f(E) \rightarrow f(\alpha E)$, conserving the phase space density in the high energy range; 3. Such an evolution is not a function of space; 4. Low energy electrons ($v \sim U$) have a higher increase rate of (mean) energy consistent with equation (3); 5. Low energy electron phase space density gradually decreases with time. From test particle simulations using an ideal Fermi acceleration model, we show that the above five acceleration attributes are confirmed by our simulations, further validating the model.

This ideal Fermi acceleration model can only explain a limited set (13%) of electron acceleration events, however, likely because low background field strength and large magnetic fluctuations inside the core are required for the model to work, and only a small subset of events have these properties. The low background field strength can lower the electron leakage and decrease the effects of the convection electric field in the core (conveniently simplifying our theoretical model). Large magnetic fluctuations can result in pitch-angle scattering (again simplifying our model). When the background field strength in the core is strong, on the other hand, the phase space density evolution will become complicated. Although Fermi acceleration may still exist or co-exist with other processes, such events cannot be characterized by a continuous energy increase along the phase space density contour, as in the subset we elected to study, and thus they are harder to classify and understand.

From observations we also showed that foreshock transients, especially foreshock bubbles, can enhance bow shock-accelerated electrons to relativistic energy through two betatron accelerations (e.g., from ~30 keV to ~200 keV). Additionally, as the phase space density is lowered by leakage, the observed energy increase could be smaller than that inferred from field strength increases (~10). This two-step betatron acceleration explains the observations of relativistic electrons at the low-Mach number Earth's bow shock.

In prior studies of electron acceleration at shocks only the shock itself has been considered. Thus, inconsistency between expectation and observations can be attributed to the over-simplified assumptions made previously, which ignored the foreshock region and the associated transients. Our study reveals that foreshock transients should be considered as parts of the shock acceleration process and viewed as extended nonlinear shock structures.

Chapter 6. Ion acceleration

In Chapter 4, I showed that some foreshock transients can accelerate ions. In this chapter, I will investigate how ion acceleration might occur and demonstrate such an acceleration mechanism. Previous 2-D hybrid simulations by Omidi et al. [2010] suggest that ions may be accelerated by bouncing between the bow shock and an earthward-moving foreshock bubble's upstream boundary, which could also be true for hot flow anomalies, spontaneous hot flow anomalies, and foreshock cavities, although this effect has not been reported observationally. In Chapter 5, I showed that electrons can be accelerated through such a process. Here I will investigate whether such a Fermi-like process also operates on ions as suggested by Omidi et al. [2010]. In Section 6.1 I will present one observational example. I will compare it with hybrid simulation results in Section 6.2. In Section 6.3, I will demonstrate that energetic ions can leak out of foreshock transients and explain how such leakage masks our assessment of ion energization at cores, implying that ion acceleration is more pervasive than inferred by a strict consideration of the statistical analysis presented in Chapter 4.

6.1 Ion acceleration: observations

According to the simulation by Omidi et al. [2010], if ions can gain energy through bouncing, i.e., reflection at the earthward-moving upstream boundary of foreshock transients, earthward ions faster than the solar wind should be observed. Thus, we use the observations of an energetic earthward component inside the cores of foreshock transients as a criterion to search the event list in Appendix d, and we found 63 events out of 247. To further investigate whether this component is caused by bouncing, we selected 13 events with less diffuse (more beam-like) ion distributions so we can more easily identify the solar wind beam, a sunward foreshock ion

beam, and an earthward high-speed beam. Here I present the most representative event from this group. I will demonstrate the acceleration process by analyzing the spatial structure and ion distributions.

As shown in Figure 6.1, TH-C (at [15.8, 3.4, -2.7] R_E in GSE coordinates) observed a foreshock transient with a hot, tenuous core bounded by a shock-like structure on its upstream side. This foreshock transient is likely a foreshock bubble (classification of the foreshock transient type is unnecessary for the purposes of the ensuing discussion, however). Using the magnetic/mixed-mode coplanarity method [Schwartz, 1998], we estimated the shock normal, [0.91, -0.40, -0.06]. The shock normal speed in the spacecraft frame, calculated from mass conservation [Schwartz, 1998], is ~300 km/s earthward (solar wind speed is ~520 km/s from OMNI).

Ion energy flux enhancement at several to tens of keV inside the core can be seen in Figure 6.1c. The minimum energy of this energy flux enhancement gradually decreases (the ions exhibit energy dispersion). The flux enhancement, which can also be seen in the azimuthal (phi) spectra of the 50 keV to 100 keV ion energy flux (Figure 6.1b), is evident mainly at 180º (earthward). Around the downstream boundary of the core (first vertical dashed line in Figure 6.1), this flux enhancement is along a field line (black line in Figure 6.1b indicates the IMF phi angle).

To fully characterize these energetic ions, we examine the ion distributions (Figure 6.2). Figure 6.2a shows the ion distribution around the downstream boundary of the core (the first vertical dashed line in Figure 6.1) in the BV plane (X-axis is parallel to the IMF; Y-axis is along the bulk velocity component perpendicular to the IMF). There are three components: the solar wind ion beam, an anti-field-aligned foreshock ion beam, and another field-aligned beam in the

same direction as the solar wind but much faster (~1000 km/s). Because the downstream IMF is mainly radial (Figure 6.1a), the local θ_{BN} of the bow shock is very small. Thus, as expected from the adiabatic reflection model [e.g., Burgess et al., 2012], the sunward foreshock ion speed is close to the solar wind speed.

Inside the core, on the other hand, because the magnetic field is very small, the BV plane is not well defined. To avoid such uncertainties, we also examine the distributions in the GSE-XY plane. In Figure 6.2d (middle of the core; second vertical dashed line in Figure 6.1), the solar wind beam is barely seen, but we can still see a sunward foreshock ion beam at ~400-500 km/s and an earthward ion beam at ~1000 km/s. In Figure 6.2f, near the upstream boundary of the core (third vertical dashed line in Figure 6.1), the distribution is also dominated by earthward high-speed ions. Thus, the several keV to tens of keV energy flux enhancement is caused by these earthward high-speed ions.

But where do these earthward high-speed ions originate? Because the most energetic ions are moving earthward, their source should be at the upstream side of the enhancement, which is also the upstream boundary of the core (foreshock bubble sheath; fourth vertical dashed line in Figure 6.1). Thus, one reasonable hypothesis for the ion energization is sunward foreshock ion reflection at this boundary (see sketch in Figure 6.3).

To analyze how these ions are reflected, we need to know the geometry of the magnetic field. In Figure 6.1a, the magnetic field is very weak inside the core and suddenly increases to more than 10 nT at the foreshock bubble sheath. Because the magnetic field is divergenceless, the magnetic field in the foreshock bubble sheath near the boundary should be roughly perpendicular to the boundary normal (assumed to be the same as the foreshock bubble shock

normal [0.91, -0.40, -0.06]). Indeed, the magnetic field at the fourth vertical dashed line in Figure 6.1 has a very strong negative Y component and a weak negative X component, nearly perpendicular to the normal (or along the surface in Figure 6.3). When sunward ions from the core reach the foreshock bubble sheath, the ion velocity must be separated into field-aligned motion and gyromotion. As seen from the geometry in Figure 6.3, the field-aligned component, though determined by the injection direction of each ion, is on average opposite the field direction. These ions can only gyrate partially, mainly along negative Z, and then move back to the core. In the spacecraft frame (Earth frame), ions gain twice the boundary normal velocity because of their partial gyration along the convection electric field (mainly in negative Z) inside the foreshock bubble sheath (Figure 6.3), i.e., specular reflection from a moving boundary.

To confirm this process, we look at the distribution function (Figure 6.2g and 6.2h) collected near the fourth vertical dashed line in Figure 6.1. Because the gyroradius of 1-10 keV ions in a 10 nT field is ~1000 km and the boundary normal speed is ~300 km/s, the distributions (each collected during a minimum accumulation time of 3 s, the spin period) can cover most reflecting ions. In Figure 6.2g (BV plane), we see that the foreshock bubble sheath flow is mainly in the perpendicular direction ($E \times B$ drift, ~300 km/s earthward calculated using foreshock bubble sheath velocity and 3 s averaged magnetic field), and secondary ions are antiparallel to the field. Figure 6.2h is the ion distribution in the BE plane (Y-axis is the convection electric field direction; BE plane is perpendicular to the BV plane). These ions gyrate only partially, mainly along the convection electric field (along Y-axis). Therefore, the distributions are consistent with what we expect from reflection at the upstream boundary.

Next we discuss the energy gain from this process. Note that in Figure 6.2g, the Y-axis is approximately earthward. If transformed into the rest frame of the foreshock bubble sheath flow

(where the convection electric field is zero), sunward- and earthward-moving ions (ions before and after reflection) have roughly the same speed. However, in the spacecraft frame (Earth frame) in Figure 6.2g, the earthward-moving (reflected) ions have an additional twice the $E \times B$ drift speed (~600 km/s) of sunward (unreflected) ions. Indeed, in Figure 6.2b and 6.2d we see that the speed difference in the x direction between sunward (~400-500 km/s) and earthward (~1000 km/s) ions is roughly 600 km/s. We conclude that these earthward high-speed ions are those reflected by the earthward-moving boundary.

The ion energy flux enhancements in the event extend outside the core's downstream boundary (around 22:40:30-22:40:45 in Figure 6.1b and 6.1c). We suspect that ion leakage is occurring here due to the large gyroradii of energetic ions. However, because of the large, variable background magnetic field, we cannot identify the exact location of the downstream boundary to definitively claim that downstream leakage is occurring. We will show definite evidence of leakage in Section 6.3.

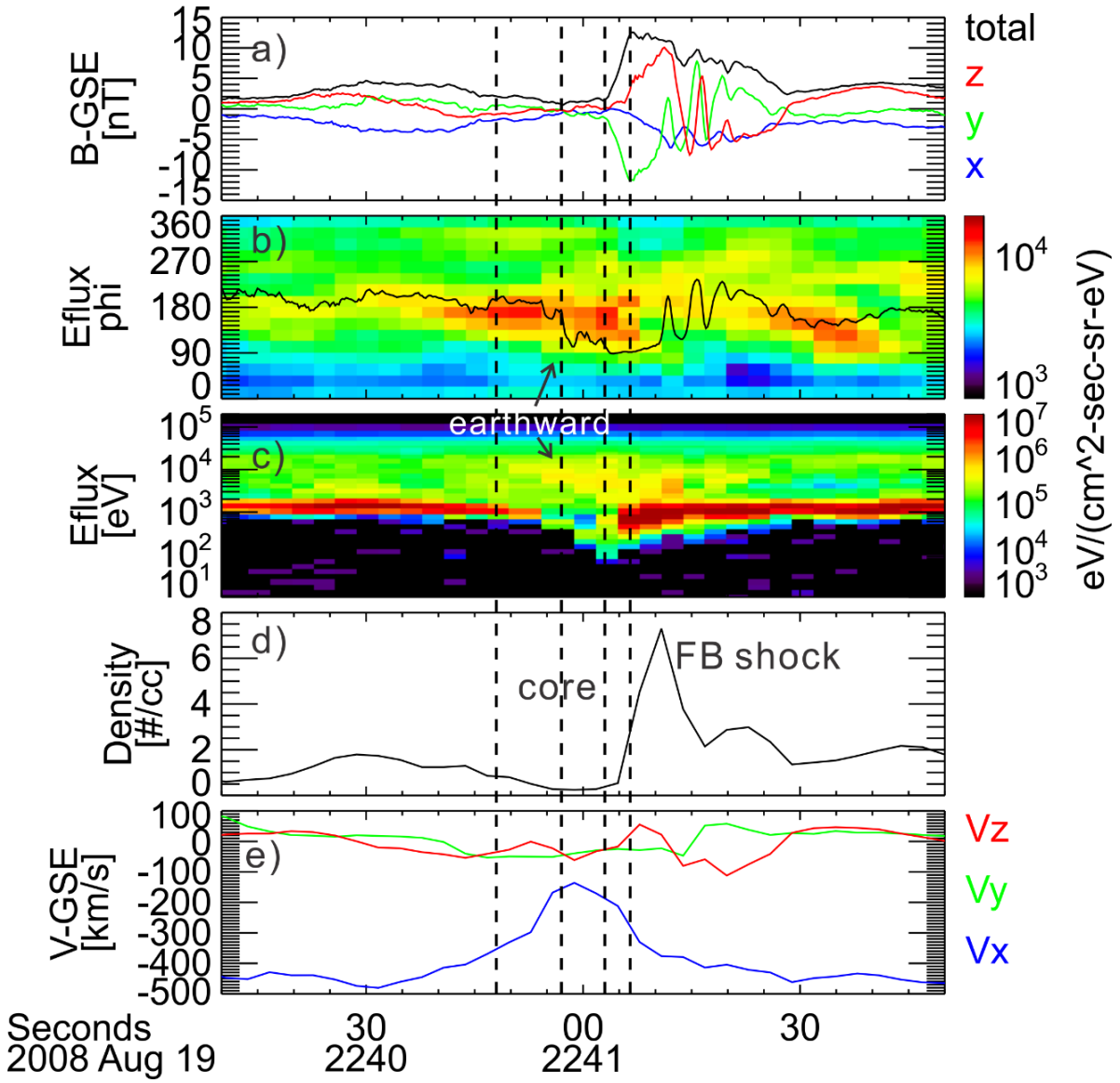

Figure 6.1. *TH-C observations of our event. From top to bottom: (a) magnetic field in GSE coordinates (here and in all subsequent plots XYZ, totals are in blue, green, red, black, respectively); (b) ion energy flux spectra in spacecraft azimuthal (phi) angle in the 50 keV to 100 keV energy range (black line indicates the magnetic field azimuth in spacecraft coordinates); (c) ion ESA and SST (combined) energy spectra (d) total ion density; (e) ion velocity in GSE coordinates. Vertical dashed lines indicate the time of ion distributions in Figure 6.2.*

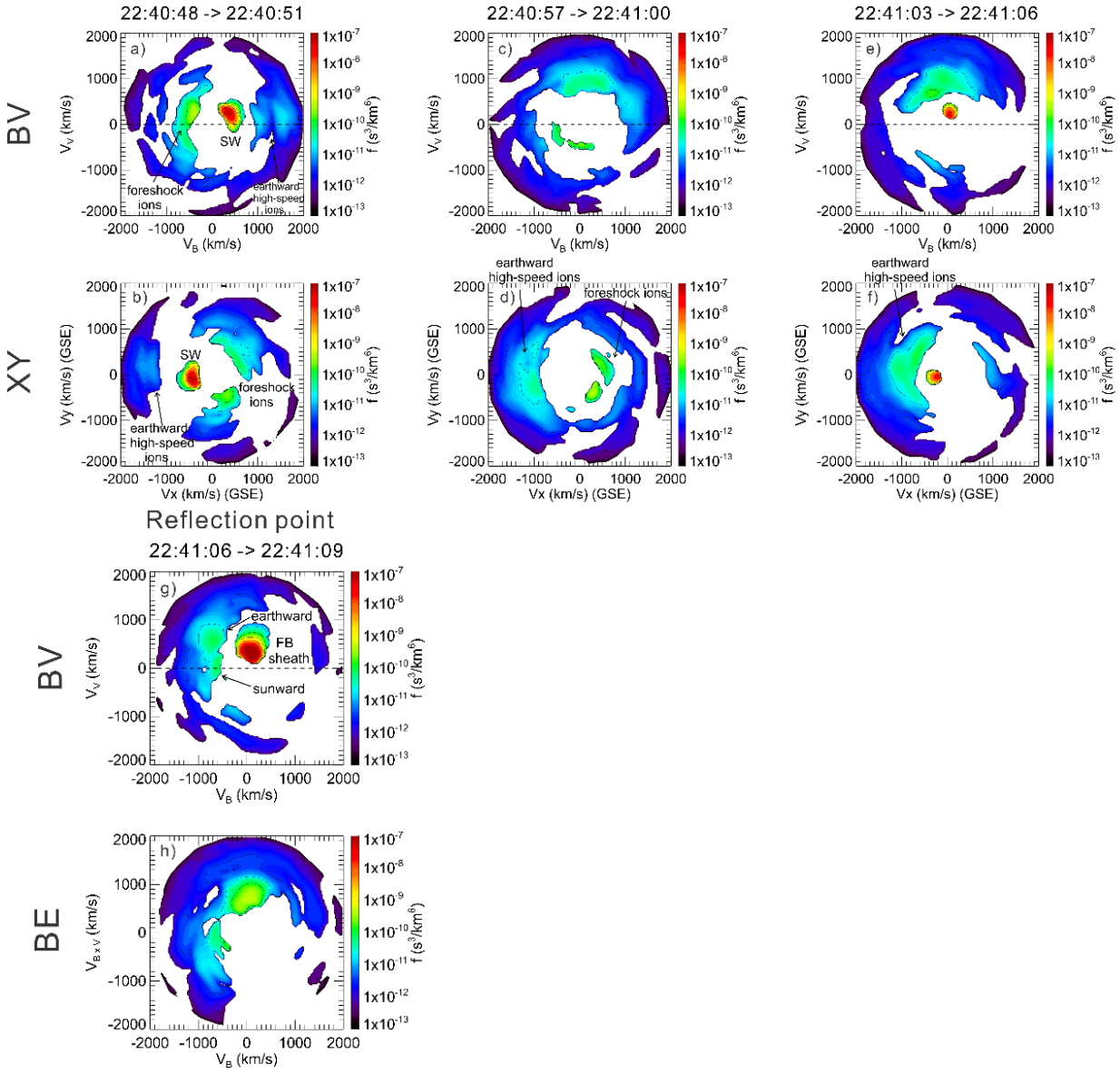

Figure 6.2. *Ion distributions at four observation times (the four columns correspond to the four vertical dashed lines in Figure 6.1) in the BV, GSE-XY, and BE planes. The distributions are 2-D slices extracted from 3-D distributions. The BV plane means that the X-axis is in the direction of the field line (averaged over 3 s) and the V-axis is in the direction of the velocity component perpendicular to the magnetic field. The BE plane means that the X-axis is along the field-line*

direction and the plane contains the convection electric field, positive along the +Y axis. SW is short for solar wind.

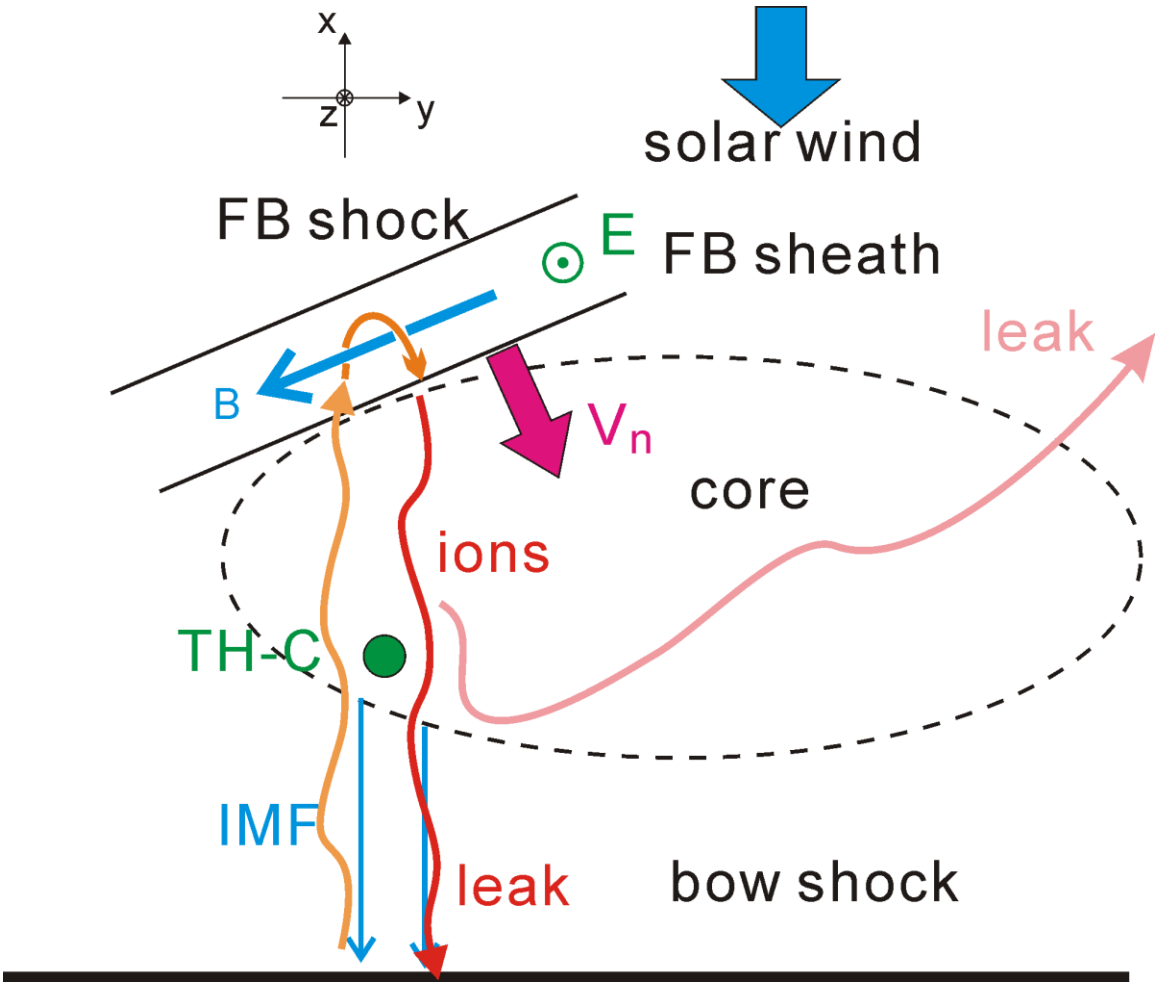

Figure 6.3. *Sketch of the event. The orientation of the foreshock bubble sheath and the field direction are sketched based on measurements. Solar wind ions are first reflected by the bow shock and then become sunward field-aligned foreshock ions (orange squiggly line). When these foreshock ions encounter the enhanced magnetic field at the foreshock bubble sheath, they gyrate partially along the convection electric field (orange half turn) then move with higher energy/speed back towards the core and occasionally past it, earthward, towards the bow shock (red squiggly line). Some of them can also move upstream and leak out (pink squiggly line).*

6.2 Ion acceleration: simulations

From the previous observations, I have shown that sunward foreshock ions in the cores of foreshock transients can be reflected by an earthward-moving boundary and gain energy. To further confirm this, we employed a generic 3-D global hybrid simulation motivated by the characteristics epitomized by the event presented and the other 12 events in our database. Figure 6.4 shows our simulation result in an XY cut ($Z = 0$) and an XZ cut ($Y = 10\ R_E$, because the foreshock is in the first quadrant of the XY plane as IMF is [-4.7, -1.7, 0] nT). The simulation result is also shown in Movie S4 in the supplementary material. After the bow shock forms, the foreshock starts to develop upstream of the quasi-parallel bow shock, which is much more disturbed than the quasi-perpendicular bow shock (Figure 6.4a and 6.4b). In the foreshock, spontaneous structures (including foreshock cavities, foreshock cavitons, and spontaneous hot flow anomalies) with large density and field strength variations can be seen. Later, a rotational discontinuity convects into the simulation domain. A foreshock bubble (identified by its tenuous core bounded by a shock labeled in Figure 6.4c and 6.4d) forms upstream of the rotational discontinuity, grows larger and larger, and collides with the bow shock. The variation patterns of the magnetic field and density are quite similar. Our 3-D simulation is consistent with previous 2-D simulations by Omidi et al. [2010], except that the foreshock bubble in our system has a finite shape in the YZ plane (Figure 6.4), leading to important constraints on how particles can evolve.

To compare the simulation more directly with observations, we put multiple virtual spacecraft in the first quadrant of the XY plane. Here we present an observation by one of these spacecraft at [13.2, 4.8, 0.0] R_E ($r = 14\ R_E, \varphi = 70°$) as an example (Figure 6.5), because this spacecraft crosses the middle of the fully formed foreshock bubble. Figure 6.5 reveals the classic

signatures of a foreshock bubble with a hot, tenuous core bounded by a shock on its upstream side. Inside the core, there is enhancement of the ion energy flux at several keV (Figure 6.5f). To find the reason for this energy flux enhancement, we look at ion distributions (vertical dotted line in Figure 6.5) in the XY and XZ planes (Figure 6.5g and 6.5h). As in observations, there are three main components: the solar wind beam, a sunward foreshock ion beam, and an earthward high-speed component. The sunward foreshock ion speed is close to the solar wind speed; thus, the enhancement of ion energy flux at several keV corresponds to the most energetic earthward high-speed component, as in observations. Note that the earthward high-speed component has two beams, one mainly in the earthward direction with stronger flux, and the other one with a strong YZ component and weaker flux.

To understand the ion distributions, we trace each component in Figure 6.5g and 6.5h to obtain their trajectories. We first confirm that the solar wind beam is indeed directly from the solar wind (but decelerated), and sunward ions are bow shock-reflected solar wind ions, i.e., foreshock ions that enter the core (not shown here). What about earthward ions? Figure 6.6 shows representative ion trajectories corresponding to two earthward ion beams (star and cross in Figure 6.5g and 6.5h). As seen in Figure 6.6a-d, both ions are originally solar wind ions. Then they are reflected by the bow shock and become foreshock ions. This process barely increases their energy (indicated by trajectory colors) because the local bow shock is quasi-parallel. Then these sunward ions encounter the foreshock bubble sheath and are reflected. Upon reflection, the ions gain energy (from ~1-2 keV to 4.2 keV for ion-1 and to 3.7 keV for ion-2). (Movie S4 shows the motion of traced ions even more clearly.) Therefore, the ion tracing results confirm our explanation of energization of earthward high-speed ions.

But how are ions reflected, and why are there two beams? As seen in Figure 6.5a, there are two magnetic field peaks in the foreshock bubble sheath: one mainly in the Y direction and a second one mainly in the Z direction. In Figure 6.6a-d, we label the magnetic and electric field directions at the time and location of each ion's reflection. As shown in Figure 6.6a and 6.6b (corresponding to star in Figure 6.5g and 6.5h), the local magnetic field has an enhanced B_y and the electric field is dominated by E_z (we do not consider B_x as B_x does not affect V_x, but with a finite B_x, the boundary is closer to a magnetic mirror than to a discontinuity). In Figure 6.6b, we see ions gyrate partially on the XZ plane along E_z back to the core. Ion-2 (cross in Figure 6.5g and 6.5h) is similar but reflected by the enhancement of B_z: ions partially gyrate on the XY plane along E_y (Figure 6.6c), although their reflection occurs at different times for the two beams (corresponding to two different but well-formed magnetic structures within the foreshock bubble). The calculated instant gyroradii of ion-1 and ion-2 using B_y and B_z at the reflection point (labeled in Figure 6.6a and 6.6d) are 1.98 R_E and 1.56 R_E, respectively, consistent with the ion trajectory shown in Figure 6.6b and 6.6c. Thus, both ion trajectories are consistent with our explanation of the reflection process from observations (Figure 6.2g and 6.2h): when ions in the core encounter the enhanced magnetic field in the YZ plane, they gyrate partially along the convection electric field (Earth frame) back to the core. Additionally, we see that the difference between the two beams is that they are reflected at different locations on the foreshock bubble sheath with different magnetic field directions. Note that most of our observations and virtual spacecraft observations in simulations see only one earthward beam, probably because it is unlikely that ions reflected at different locations will reach the same point at the same time.

In the observations, we saw that energetic ions in the core could leak out. To confirm this, we continued to trace these earthward high-speed ions after they reached the virtual spacecraft.

(We do not show a full ion trajectory from solar wind to acceleration and then leakage, because details of acceleration and leakage can be seen more clearly in two separate figures.) Figure 6.7 shows two representative subsequent trajectories of these earthward high-speed ions. We see one traced ion directly leak downstream towards the bow shock. The other is reflected by the downstream boundary of the core and then exits the core on the upstream side along the field line into the solar wind. Thus, from simulations, we also confirm that accelerated, energetic ions in the core can indeed leak out to both the downstream and upstream sides. Therefore, the simulated ion acceleration and ion leakage processes are consistent with our observations. In the next section, I will further investigate the ion leakage and show that leaked ions can affect our identification of ion acceleration events in our statistical study (as discussed in Chapter 4).

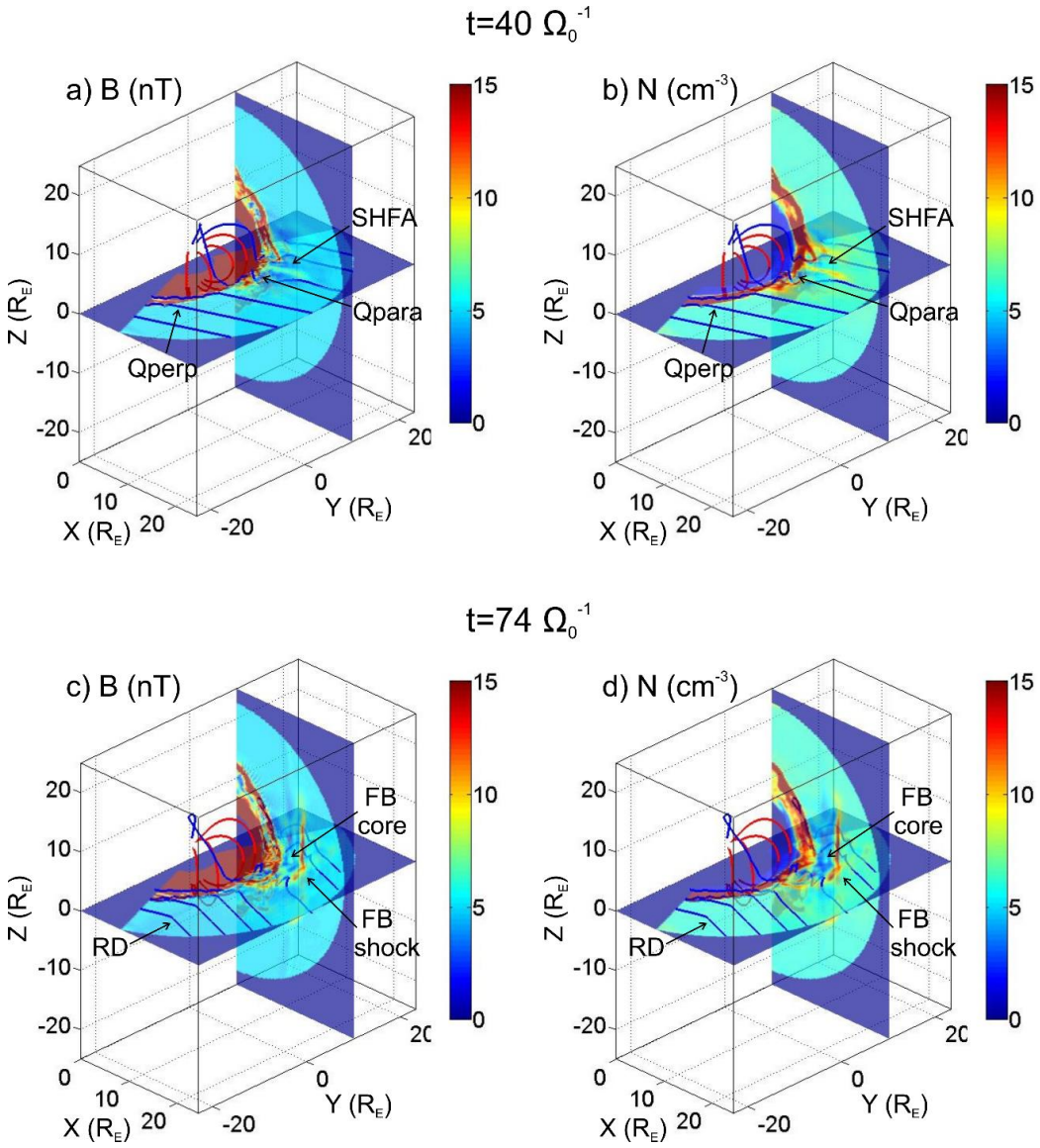

Figure 6.4. *Three-dimensional global hybrid simulation results at time* $t = 40\,\Omega_0^{-1}$ *(a, b) to show the foreshock and* $t = 74\,\Omega_0^{-1}$ *to show a fully formed foreshock bubble (c, d). Contours of the (a, c) magnetic field magnitude* $B(nT)$ *and (b, d) density* $N(cm^{-3})$ *in the XY* $(Z = 0)$ *and XZ* $(Y = 10R_E)$ *planes. Red lines indicate Earth's closed dipole field lines and blue lines indicate IMF field lines. Quasi-parallel bow shock (Qpara), quasi-perpendicular bow shock (Qperp), spontaneous hot flow anomaly (SHFA), rotational discontinuity (RD), and foreshock bubble (FB core and FB shock) are labeled.*

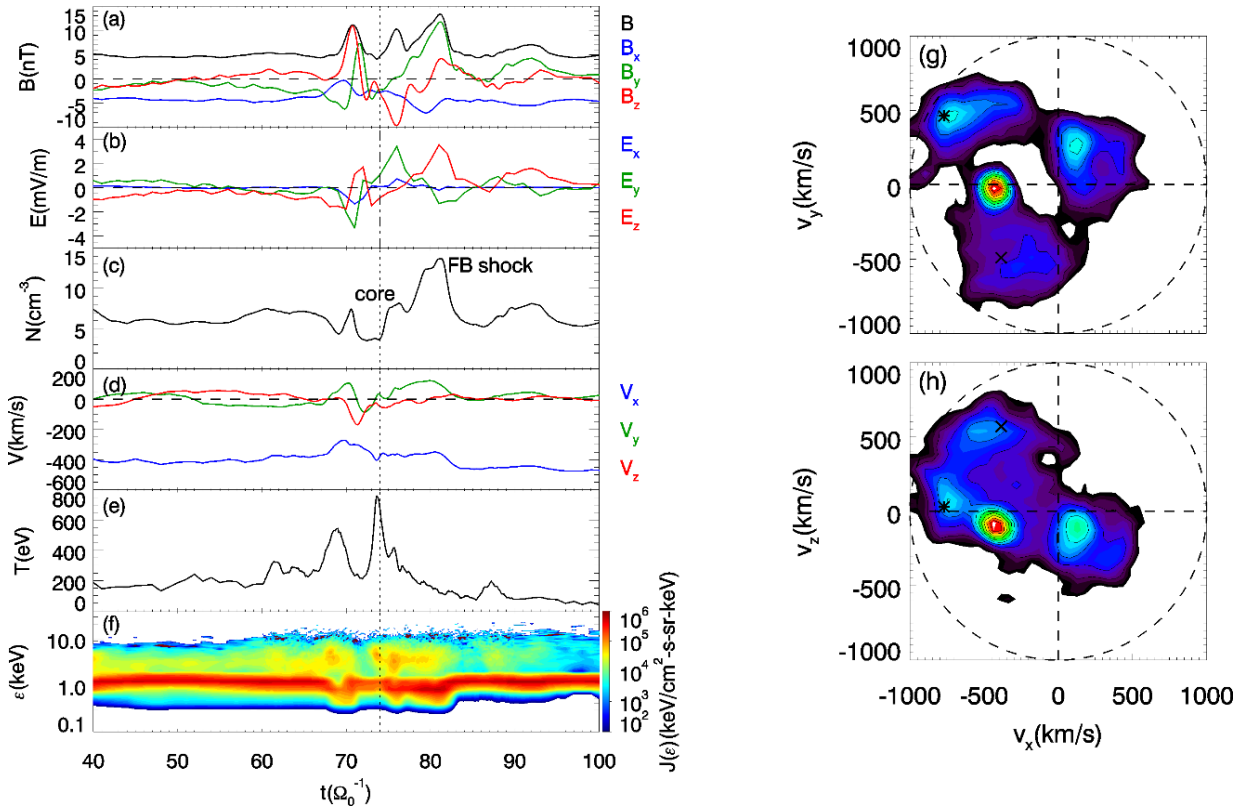

Figure 6.5. *Virtual satellite observations at [13.2, 4.8, 0.0] R_E in the simulation for (a) magnetic field $B\ (nT)$, (b) electric field $E\ (mV/m)$, (c) ion density $N\ (cm^{-3})$, (d) ion flow velocity $V\ (km/s)$, (e) ion temperature $T\ (eV)$, and (f) ion energy flux $J(\mathcal{E})(keV/(cm \cdot s \cdot sr \cdot keV))$. Ion velocity distributions in the (v_x, v_y) (g) and (v_x, v_z) (h) planes at $t = 74\ \Omega_0^{-1}$ (shown by the vertical dotted line).*

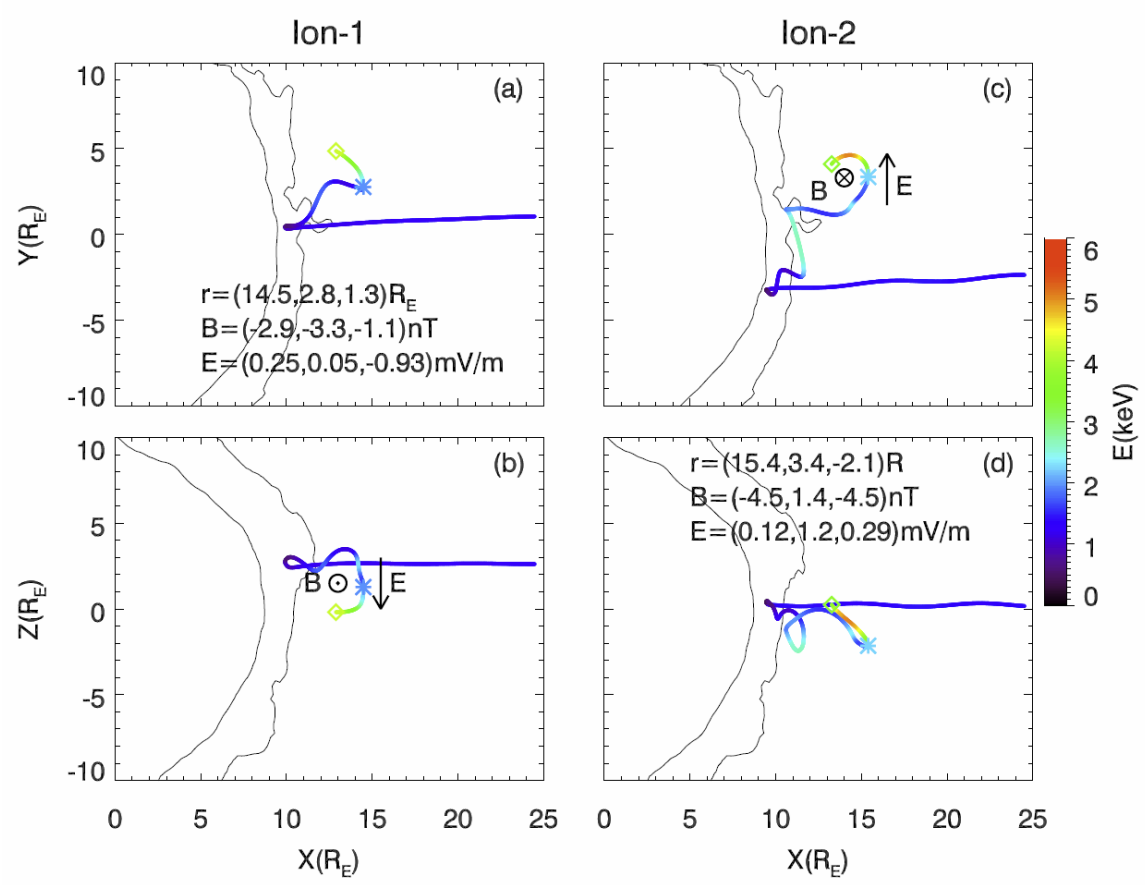

Figure 6.6. *Two representative trajectories (projected in the XY and XZ planes) of ions that are accelerated in the foreshock bubble. The color of the trajectories represents the energy of the ions. The black curves are the contours of number density at* $11cm^{-3}$ *showing the locations of the magnetopause and bow shock mapped to the XY* ($Z = 0$) *and XZ* ($Y = 5R_E$) *planes. The prism indicates the virtual spacecraft. The asterisk indicates the reflection point with position (r), magnetic field (B), and electric field (E) listed.*

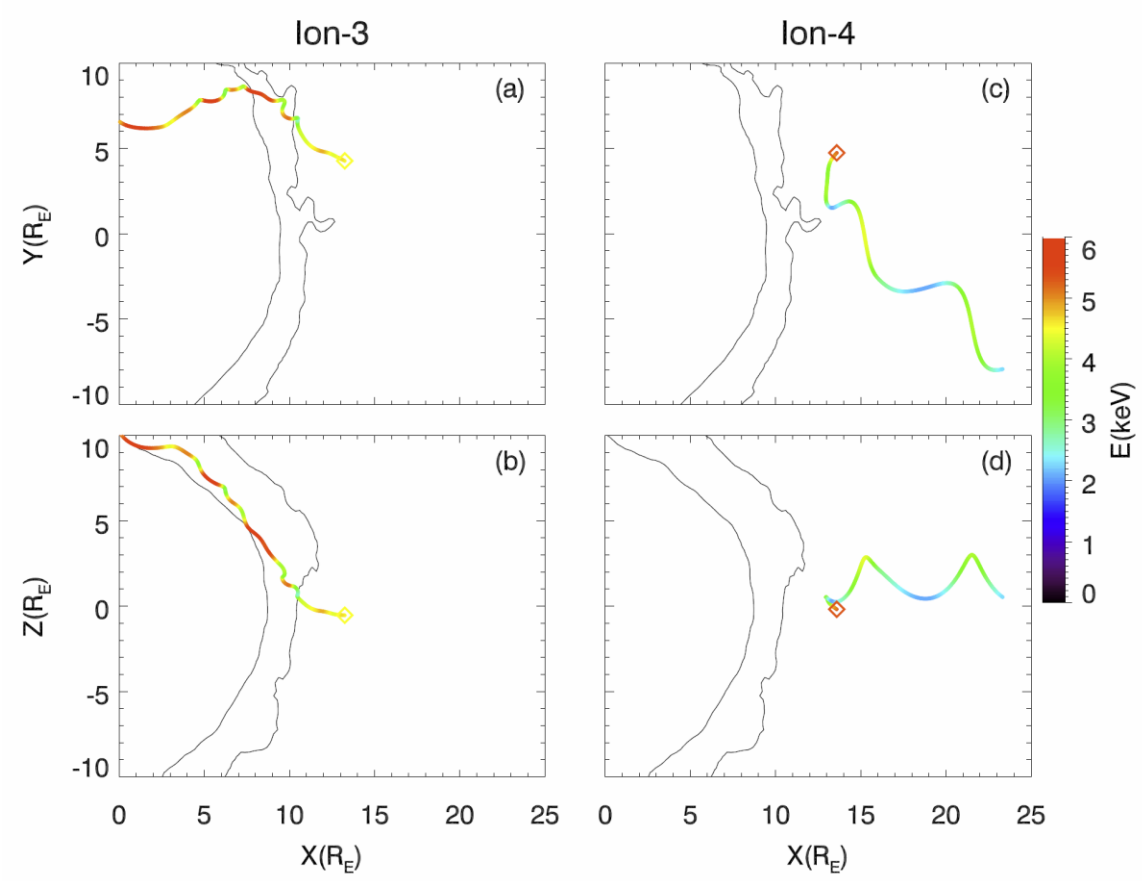

Figure 6.7. *Two representative ion leakage trajectories after the ions have been accelerated inside the foreshock bubble. Same format as in Figure 6.6.*

6.3 Observation of energetic ion leakage

Inspection of the event list in Appendix d reveals occasional energy dispersion signatures of earthward-moving ions downstream and/or upstream of the transient (in 7 out of 247 events). Here I apply a detailed case study to the event with the most ideal IMF direction: the GSE-X component is nearly zero on one side of the foreshock transient. Under this condition, the geometry is simple to analyze, and no background foreshock ions can be produced from the local

bow shock. I will reveal that these dispersed earthward-moving ions were leaked from the cores of the foreshock transients.

Figure 6.8 presents TH-C ([14.6, 3.0, -2.1] R_E in GSE, ~0.82 R_E away from the bow shock along GSE-X) observations of a hot-flow anomaly. The driver discontinuity of this hot flow anomaly was observed by TH-B and ACE. By using the three-spacecraft timing method from ACE, TH-B, and TH-C, we obtain the discontinuity normal [0.41, 0.18, 0.89]. The normal component of the magnetic field over the field strength is 7% at TH-B and 2% at TH-C, meaning that the transit motion of the discontinuity and the corresponding hot flow anomaly is almost perpendicular to the IMF direction. The transit speed of the discontinuity along the local bow shock surface, near TH-C, is ~142 km/s.

Upstream of the hot flow anomaly (around 23:07-23:10 UT), a clear energy dispersion (low energies first – high energies later) can be seen in the combined ESA-SST ion energy spectra (Figure 6.8d). (There is a gap between ESA and SST at around 25 keV due to their different instrument sensitivities.) To investigate the origin of this dispersion, we examine the ion distribution functions shown in Figure 6.9a, b for 23:08:13 UT and Figure 6.9c, d for 23:08:28 UT (these times are indicated by two vertical dotted lines in Figure 6.8). Figure 6.9a, c is a BV cut, i.e., the X-axis is the magnetic field direction, and the XY plane contains the ion velocity vector with a positive projection along the +Y direction. Figure 6.9b, d is a cut perpendicular to the magnetic field direction, with the X-axis along the bulk velocity projection, to indicate the gyrovelocity phase (the angle between the bow shock normal/GSE-X and the gyrovelocity shown in Figure 6.10). First, we see that the solar wind beam was almost perpendicular to the IMF (Figure 6.9a, c). This is because the magnetic field was almost perpendicular to GSE-X (B_x~0 in Figure 6.8a). Thus, the solar wind speed nearly equals the $E \times B$ drift speed. Then we

see that there is another beam, also perpendicular to the IMF, that corresponds to the dispersed ions in Figure 6.8d. Because this beam was moving in the same direction as the solar wind (earthward) it more likely originates at a place farther upstream than the spacecraft and thus is less likely to have come from the bow shock. As the energy dispersion commenced at the hot flow anomaly (Figure 6.8d), it is reasonable to consider that the beam was coming from the hot flow anomaly.

To understand the reason for the dispersion, we must examine the event geometry in Figure 6.10. The vertical direction is the local bow shock normal, approximately along the GSE-X direction because TH-C was near the nose of the bow shock ([14.6, 3.0, -2.1] R_E in GSE). The IMF is perpendicular to the solar wind and points out of the plane. The field strength, only 1.3 nT, results in energetic ions from the hot flow anomaly having very large gyroradii to gyrate towards TH-C (several R_E for a few keV ions). Because the discontinuity normal is perpendicular to the IMF direction, the driver discontinuity as well as the hot flow anomaly was moving along the bow shock perpendicular to the IMF away from TH-C (magenta arrow in Figure 6.10). As the distance between the hot flow anomaly and TH-C increases, ions from the hot flow anomaly would need larger gyroradii – meaning larger energy – to reach TH-C. This, then, would be the likely reason for the ion energy dispersion.

To test the above hypothesis, we first calculate the ion energy that can reach the spacecraft based on this geometry and compare it with observations. We separate the ion motion into two parts: a constant velocity that satisfies $0 = q\vec{v}_0 \times \vec{B} + q\vec{E}$ (equals the $E \times B$ speed, but we do not call it a drift because ions cannot finish a full gyration) and a gyromotion that obeys: $m\frac{d\vec{v}_\perp}{dt} = q\vec{v}_\perp \times \vec{B}$. In other words, we move into the solar wind frame, moving at $\vec{v}_0$, in which the electric

field vanishes and the particle gyrovelocity $|\vec{v}_\perp|$ and gyroradius R are thus constant. Indeed, in Figure 6.9b, d, we can see that in the perpendicular plane the energetic ion distribution displays roughly gyromotion around the solar wind $E \times B$ drift speed. Then we can relate the ion trajectory with the geometry of the hot flow anomaly and TH-C. The first equation is the projection of the ion trajectory onto the horizontal direction (along the bow shock, in the plane of Figure 6.10),

$$\Delta L + v_t t_s = R(\cos\varphi_s - \cos\varphi), \tag{6.1}$$

where v_t is the hot flow anomaly's transit speed (142 km/s in this event), t_s is the time when the ions were ejected relative to the time when TH-C left the hot flow anomaly, R is the gyroradius, φ_s is the initial gyrovelocity direction when the ions were ejected (the angle between the initial $\vec{v}_\perp$ and the local bow shock normal, increasing clockwise if viewed opposite the field direction; in Figure 6.9b, d, since the shock normal is opposite the solar wind speed, the gyrovelocity angle is approximately 0º in the opposite solar wind direction, increasing clockwise to ~180º along the solar wind direction), and φ is the final gyrovelocity angle observed by TH-C. ΔL can be determined by the second equation:

$$\Delta L = \Delta H \cdot \cot\theta = -[R(\sin\varphi - \sin\varphi_s) - v_0(t - t_s)] \cdot \cos\alpha \cdot \cot\theta, \tag{6.2}$$

where ΔH is the projection of ion trajectory onto the vertical direction, θ gives the slope of the local hot flow anomaly boundary, $t - t_s$ is the time difference of ions moving from the hot flow anomaly to TH-C, which is equal to the gyrovelocity phase difference over gyrofrequency, $\frac{\varphi - \varphi_s}{\omega}$, and $cos\,\alpha$ comes from the finite B_x, i.e., $\sin\alpha = B_x/|B|$. In this event, $cos\,\alpha$ is almost 1. From equations (1) and (2), we obtain the perpendicular speed at TH-C as a function of time and gyrovelocity phase,

$$v_\perp = \frac{v_t(\omega t-(\varphi-\varphi_s))+v_0(\varphi-\varphi_s)\cdot\cos\alpha\cdot\cot\theta}{(\cos\varphi_s-\cos\varphi)+(\sin\varphi-\sin\varphi_s)\cdot\cos\alpha\cdot\cot\theta}. \quad (6.3)$$

In this equation, θ is the only parameter we cannot measure. Based on simulations [e.g., Omidi and Sibeck, 2007], hot flow anomalies are likely elongated. A reasonable estimate of θ is around 60º. Since term $v_t(\omega t-(\varphi-\varphi_s))$ is not directly multiplied by $\cot\theta$, the estimates of θ barely affect the $v_\perp$- t relation with fixed gyrovelocity phase and mainly affect the $v_\perp$- φ relation with fixed observation time.

From equation (6.3), we can see that $v_\perp$ is proportional to time because larger gyroradii are needed when the hot flow anomaly is moving away. But what is the relation between $v_\perp$ and the initial gyrovelocity phase φ_s? Figure 6.9e shows an example of ion trajectories from different initial gyrovelocity phases reaching the spacecraft at the same moment (moment of Figure 6.9a, b) with a fixed final gyrovelocity phase (135º). Note that these ions are not necessarily ejected at the same time; their ejection time depends on the shape or slope of the hot flow anomaly boundary. Positive φ_s means that ions will travel towards the bow shock very quickly after ejection and thus need a very large $v_\perp$ to reach TH-C. Negative φ_s, on the other hand, implies that ions have plenty of time to gyrate and do not need a large $v_\perp$. Larger φ_s gives larger $v_\perp$. Additionally, ions with larger (smaller) final gyrovelocity phase, φ, come from farther (closer) upstream than shown in Figure 6.9e. Thus, the upper (lower) limit of the gyrovelocity phase in Figure 6.9b, d likely corresponds to the ions from the hot flow anomaly's top (foot).

By fixing the observation time t (relative to the start time of dispersion, represented by the blue dashed line in Figure 6.8), we can obtain the exact relation between the observed $v_\perp$ and φ as a function of φ_s and compare it with the observed ion distributions. As shown in Figure 6.9b, d, the colored lines give the calculated relation at the corresponding observation time. Different

colors represent different φ_s, as in Figure 6.9e. The colored lines can fit the shape and energy range of the ion distribution in the cut perpendicular to the magnetic field direction. The energy range of the ion distribution is determined by different φ_s: large positive φ_s (red, yellow) gives the maximum energy that can reach the spacecraft, and negative φ_s (black, magenta) gives the minimum energy that can reach it. We have also calculated the velocity- φ relation for bow shock-ejected ions, which is inconsistent with the observations, confirming that the ions cannot have come from the bow shock.

By fixing the gyrovelocity phase φ and φ_s, we can also fit the energy dispersion ($E = \frac{1}{2}m((v_\perp \cos\varphi - v_0)^2 + (v_\perp \sin\varphi)^2)$ as parallel speed is nearly zero) in Figure 6.8d. From the ion distribution in Figure 2b, d, we choose φ =135º as an average value. In Figure 6.8d, the three red lines are the energy-time relation at three different φ_s: -30º, 50º, and 80º, giving a sense of minimum, intermediate, and maximum energy, respectively. These lines can straddle and match the observed ion energy dispersion very well. Therefore, our model is consistent with the observed ion distributions and energy dispersion, supporting our hypothesis that ions originated at the hot flow anomaly.

But how are these ions generated? This is similar to the question regarding the origin of foreshock ions: are they reflected solar wind ions or leaked magnetosheath ions? As the energy of ions upstream of the hot flow anomaly can reach tens of keV (Figure 6.8d), we can first estimate whether reflection can provide such high energy for solar wind ions. Adiabatic reflection can increase ion energy through shock drift acceleration, i.e., ions could drift on the hot flow anomaly surface along the convection electric field. As the convection electric field is continuous tangential to the boundary, we use the solar wind convection electric field (~0.4

mV/m in the spacecraft frame, an overestimate because in the hot flow anomaly rest frame, the convection electric field is smaller) multiplied by the size of the hot flow anomaly along the electric field (~3 R_E, an overestimate as the hot flow anomaly was cut by the discontinuity). The resultant maximum energy gain is ~7.5 keV, too low when compared to the observed ion energy range (Figure 6.8d). Specular reflection by itself, on the other hand, cannot increase the ion energy in the boundary rest frame. As in this event the boundary was moving away from the spacecraft, specular reflection can only decrease the ion energy in the spacecraft frame. Thus, reflection cannot explain the observed ion energy.

Next, we consider the possibility of leakage. Comparing the maximum ion energy outside the core to that inside (Figure 6.8d, blue dashed line and magenta dashed line), we see they are almost the same – in fact, the upstream dispersed ion energy gradually increases as the distance from the hot flow anomaly to the spacecraft increases. This is because ejected ions gyrate along the solar wind convection electric field to reach the spacecraft (when the distance is 1 R_E, the resultant energy gain is 2.5 keV). Therefore, leakage from the core can explain the observed ion energy.

For further proof that the ions leaked, we can examine their distributions. Figure 6.8e shows normalized phase space density-energy distributions (in the spacecraft frame without the solar wind beam) in the middle of the core (magenta), near the source (blue), and away from the source after removing the energy gain from gyration along the convection electric field (black line; obtained from phase space density along the middle red line in Figure 6.8d ($\varphi_s = 50^0$, φ =135º) after removing $qE_{conv}R(\cos\varphi_s - \cos\varphi)$, where $R = \frac{mv_\perp}{qB}$, and $v_\perp$ is determined from

equation (6.3)). We find that they match very well, concluding that these ions must have leaked from the hot flow anomaly's core.

Downstream of the hot flow anomaly, there is another energy dispersion (~23:02 UT in Figure 6.8d). From the ion distributions (not shown here), we find that these ions are field-aligned sunward ions that gain energy through adiabatic reflection at the local bow shock; their energy dispersion is simply due to a gradual change in IMF direction (or θ_{Bn}). Most importantly, however, we note that the maximum ion energy inside the hot flow anomaly is higher than the downstream background maximum foreshock ion energy (Figure 6.8d). This is not only because ion energization greater than that at the local bow shock likely occurred inside this hot flow anomaly, but also because the foreshock population downstream of it is not contaminated by leaked hot flow anomaly-heated ions. This supports the earlier hypothesis in Chapter 4 that ion heating in foreshock transients could be obscured by core ion leakage into the ambient foreshock region, and that it is hard to disentangle from energy spectrograms alone without careful modeling.

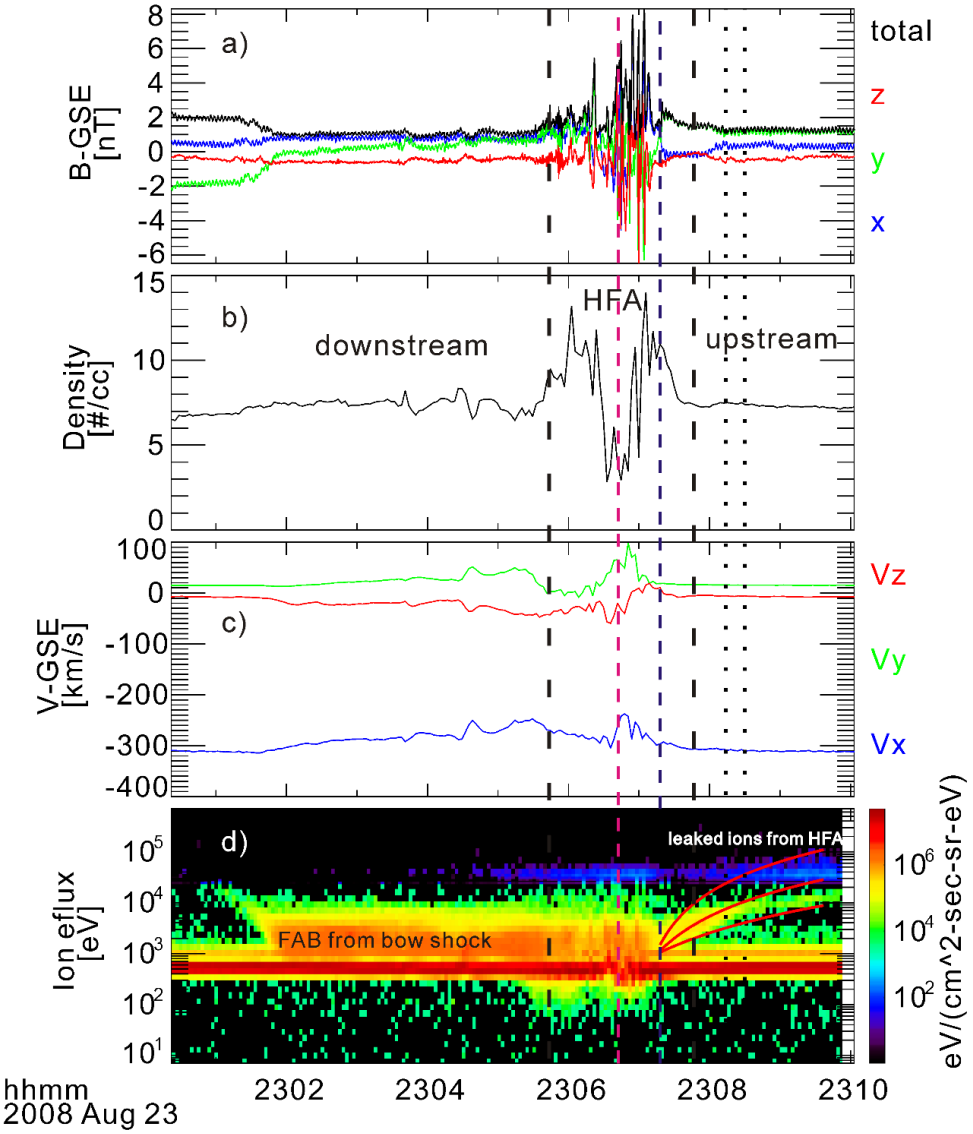
a)
B-GSE [nT]
total
z
y
x
b)
HFA
downstream
upstream
Density [#/cc]
c)
V-GSE [km/s]
Vz
Vy
Vx
d)
leaked ions from HFA
FAB from bow shock
Ion eflux [eV]
eV/(cm^2-sec-sr-eV)
hhmm
2008 Aug 23
2302
2304
2306
2308
2310

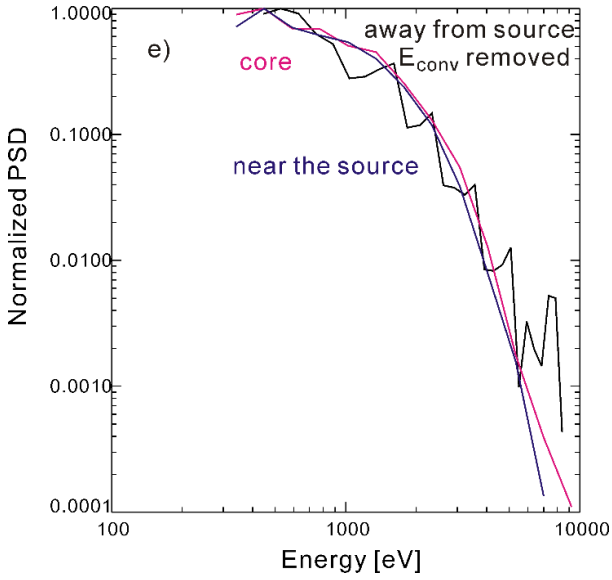

Figure 6.8. *TH-C observations of a hot flow anomaly at [14.6, 3.0, -2.1] R_E in GSE (labeled by two vertical dashed lines). From top to bottom: (a) magnetic component in GSE coordinates (XYZ, total in blue, green, red, and black, respectively); (b) total ion density; (c) ion bulk velocity in GSE coordinates (XYZ in blue, green, and red, respectively); (d) ion ESA and SST (combined) energy spectra. Ion energy dispersion can be seen from the energy spectra upstream of the hot flow anomaly (~23:07-23:10 UT). (e) comparison of normalized ion phase space density-energy distributions in the spacecraft frame without the solar wind beam: inside the core (magenta), near the source (blue), and away from the source after removing the energy increase from the convection electric field (black). The three red lines in (d) are the ion energy calculated from our model by setting the initial gyrovelocity phase φ_s to -30°, 50°, and 80° to fit the minimum, median, and maximum energy of dispersed ions. Two vertical dotted lines indicate the time of ion distributions in Figure 6.9. Ions observed downstream of the hot flow anomaly are a field-aligned beam (FAB) reflected at the local bow shock. Magenta dashed line indicates the middle of the core corresponding to the magenta line in (e). Blue dashed line indicates the source boundary, the start time of dispersion/red lines, corresponding to the blue line in (e).*

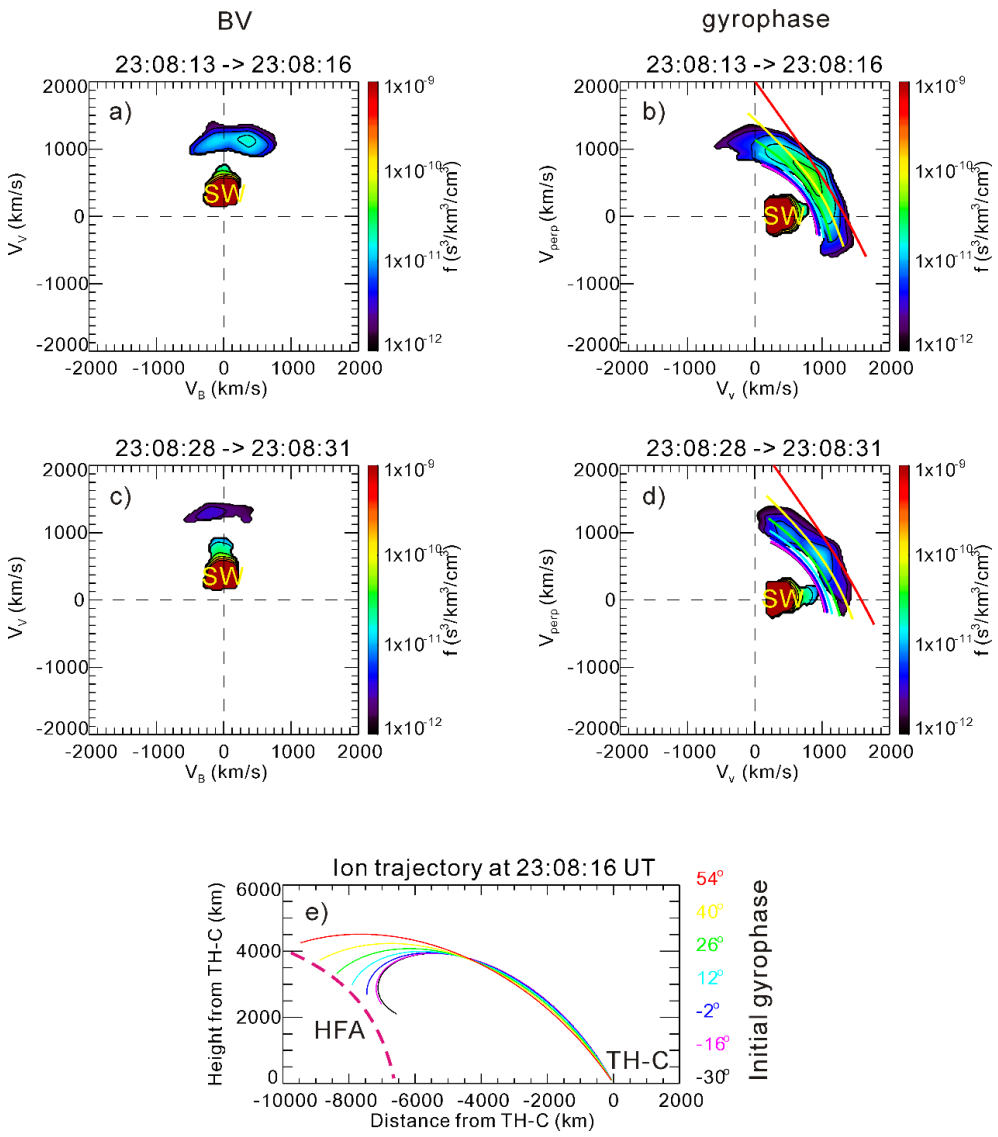

Figure 6.9. *Ion distributions at two observation times ((a, b) and (c, d) represented by two vertical dotted lines in Figure 6.8, respectively). (a) and (c) are in the BV cut (the X-axis is the magnetic field direction, and the XY plane contains the ion velocity vector with a positive projection along the +Y direction); (b) and (d) are in the cut perpendicular to the magnetic field direction at zero parallel speed (the X-axis is along the bulk velocity projection) to indicate the gyrovelocity phase. The gyrovelocity phase is ~0⁰ in the negative X direction and clockwise to ~180⁰ in the positive X direction. (e) is the ion trajectories observed by TH-C at a certain*

observation time (same as (a), (b)) with different initial gyrovelocity phase φ_s (represented by different colors from -30⁰ to 54⁰). The final gyrovelocity phase is set to be 135⁰ (roughly the average value in (b), (d)) as an example. The dashed magenta line indicates the boundary of the hot flow anomaly. These ions are not necessarily ejected at the same time. The colored lines in (b) and (d) are the calculated velocity-initial gyrovelocity phase relation based on our model. Different colors represent different initial gyrovelocity phase φ_s (same as (e)).

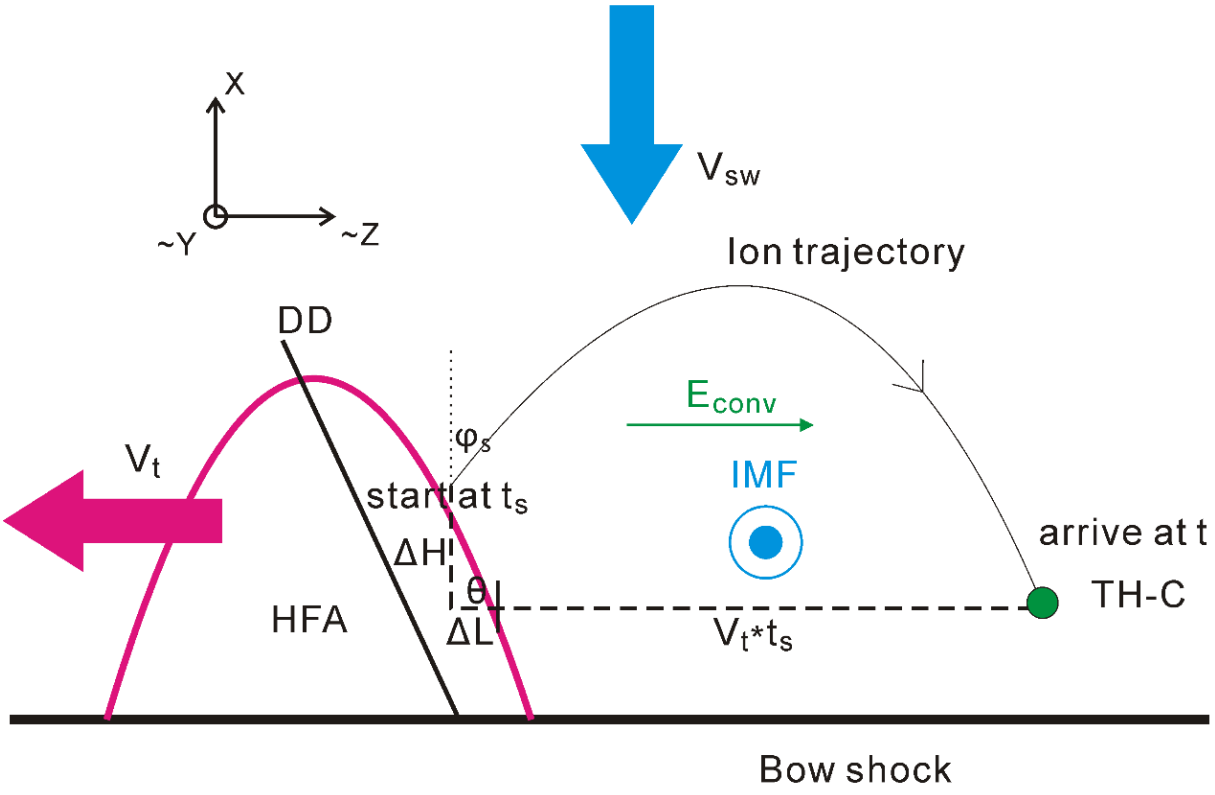

Figure 6.10. *Sketch of the geometry of our event and our model. The vertical direction is the bow shock normal direction, roughly the GSE-X direction. The hot flow anomaly (magenta) was moving away from TH-C (green dot) to the left (magenta arrow). The orientation and transit motion of the directional discontinuity (DD, black line) is based on observation, consistent with the fact that DD was moving away from TH-C. The IMF (blue) is pointing out of the plane. Ions from the hot flow anomaly gyrate towards TH-C across the convection electric field (green arrow). In this sketch, the initial gyrovelocity phase* φ_s *is the clockwise angle between the perpendicular speed and the GSE-X direction.* θ *indicates the slope of local hot flow anomaly boundary, i.e.,* $\tan\theta = \frac{\Delta H}{\Delta L}$.

6.4 Summary

From observations, I show that in a moderate subset of events (63 of 247 events), there is a several keV to tens of keV ion energy flux enhancement in foreshock transients' cores corresponding to earthward-moving ions. By analyzing ion distributions and the magnetic field direction at the foreshock bubble sheath, I reveal that those earthward high-speed ions are reflected and accelerated at the earthward-moving foreshock transient boundary through partial gyration along the convection electric field. I show that those energetic ions can leak out of the core into the surroundings, which is consistent with our observations. To further confirm the observational results, I use 3D global hybrid simulations showing similar ion energy flux enhancement up to several keV corresponding to earthward high-speed ions. By using particle tracing, I confirm that the ions are indeed reflected and accelerated by the earthward-moving boundary through partial gyration along an electric field. I also confirm that ions can leak from foreshock transients. Therefore, I conclude ions can be accelerated inside foreshock transients and that one acceleration mechanism is reflection at an earthward-moving boundary.

From observations, I show that energetic ions can leak from foreshock transients, increasing the ambient ion energy. In our statistical study (Chapter 4), it is impossible to distinguish leaked ions from background foreshock ions. Comparing the ion average energy and spectra in the foreshock transients to those in the background foreshock in search of such acceleration can produce ambiguous results. This suggests that there could be more ion acceleration events than previously thought.

Our observations demonstrate one dispersion mechanism of leaked ions: ions need larger gyroradii to reach the spacecraft when its distance to the hot flow anomaly increases. Because of

differing IMF direction and foreshock transient motion, some other mechanisms can also result in energy dispersion of leaked ions. For example, Liu et al. [2017b] show that due to $E \times B$ drift, faster field-aligned leaked ions can reach the spacecraft when its distance to the foreshock transient increases. Liu et al. [2018] show that because there is a start time of ion acceleration, leaked ions with faster parallel speed will reach the spacecraft first. In more general cases, however, there is no clear dispersion of leaked ions. To distinguish such leaked ions from background foreshock ions requires more efforts in the future.

D. Conclusions and Discussion

I will first summarize our major conclusions. Then I will discuss how foreshock transients can potentially affect the shock acceleration process based on our results. Last, I will introduce the future work that can be applied to further investigate the foreshock transients and their effects on shock acceleration.

D.1 Conclusions

Foreshock bubbles can disturb the magnetosphere and could accelerate particles contributing to the parent shock acceleration. Using THEMIS observations, I first present the formation and properties of foreshock bubbles. Rotational discontinuities are known to drive foreshock bubbles. I show that tangential discontinuities can also drive them, indicating that foreshock bubbles may be more common than previously thought. I also discuss a hypothetical formation process. From a statistical study, I determine that faster solar wind speed and lower IMF strength favor formation of foreshock transients, including foreshock bubbles, hot flow anomalies, and spontaneous hot flow anomalies. The spatial structure and evolution of a foreshock bubble are demonstrated using multi-point observations. From a case study, I show that foreshock bubbles can accelerate solar wind particles through shock drift acceleration and bring them towards the bow shock, suggesting that foreshock bubbles could provide a particle source for parent shock acceleration.

To further understand particle acceleration by foreshock bubbles and foreshock transients with similar characteristics, I apply a statistical study to reveal that almost all foreshock transients, including foreshock bubbles, hot flow anomalies, and spontaneous hot flow anomalies, can accelerate electrons, and some can accelerate ions, inside them. To further investigate how

foreshock transients accelerate particles, I use both observations and test particle simulations showing that Fermi acceleration is one of the electron acceleration mechanisms. From observations along with hybrid simulations, I demonstrate that betatron acceleration can accelerate bow shock-accelerated electrons to relativistic energy. Using similar methods, I show that ions can be accelerated by at least one bounce between the converging foreshock transient boundary and the bow shock. I also reveal that energetic ions inside foreshock transients can leak out, suggesting that there could be even more ion acceleration events in our statistical study.

D.2 Impacts on shock acceleration

This thesis implies that foreshock transients could play a very important role in shock acceleration, one of the most important acceleration mechanisms in the universe. Shock acceleration is still not fully understood, however. Diffusive shock acceleration (DSA) [e.g., Drury, 1983], the most widely accepted shock acceleration mechanism, can explain the observed power law spectra of accelerated particles. In diffusive shock acceleration, particles can bounce back and forth from two sides of the shock. Each reflection is in the frame of either upstream or downstream flow without energy changes through pitch-angle scattering by waves (especially Alfven waves). As the flow converges across the shock, particles can gain energy through first-order Fermi acceleration during bounces.

Although diffusive shock acceleration is the most widely accepted shock acceleration mechanism, there are some unsolved problems. For particles to participate in such an acceleration process, their energy should be large enough that they can be treated as nearly isotropic, especially for quasi-perpendicular shocks, which require a larger minimum energy threshold than quasi-parallel shocks [e.g., Lee et al., 2012]. The source of such energetic

particles is still unknown. This is one of the major problems of shock acceleration, the so-called "injection problem" [Jokipii, 1987]. Our study indicates that foreshock transients could be a source of energetic particles. Foreshock transients can accelerate particles through shock drift acceleration or Fermi acceleration [Liu et al., 2016a; Liu et al., 2017c; Liu et al., 2018] and then bring them to the parent shock to experience diffusive shock acceleration. Foreshock transients usually form in the quasi-parallel region; foreshock bubbles and hot flow anomalies, however, can sometimes form in the quasi-perpendicular region due to an IMF direction change caused by their driver discontinuity. Therefore, foreshock transients could provide a particle source for both quasi-parallel and quasi-perpendicular shocks.

Another problem of diffusive shock acceleration is that although quasi-parallel shocks require lower initial energy for particles participating in diffusive shock acceleration than quasi-perpendicular shocks, the particle acceleration is too slow to account for the observed energy [e.g., Burgess et al., 2012]. In the quasi-parallel region, particles can stream away along field lines very easily and need considerable time to be scattered back and bounce back and forth. Foreshock transients in the quasi-parallel region, however, can help reflect particles back, because they can form a compressional boundary with an enhanced field [e.g., Liu et al., 2018]. Therefore, foreshock transients could play a role in diffusive shock acceleration by increasing the efficiency of quasi-parallel shocks.

Shock drift acceleration in the quasi-parallel region can also be affected by foreshock transients. Although shock drift acceleration at quasi-parallel shocks is weaker than that at quasi-perpendicular shocks, a foreshock bubble in the quasi-parallel region can form its own quasi-perpendicular shock, which can result in more efficient shock drift acceleration [Liu et al.,

2016a]. Foreshock transients can also further accelerate particles that are shock drift accelerated at the parent quasi-parallel bow shock [Liu et al., 2018].

Foreshock transients can also help explain the inconsistency between electron acceleration theory and the observed electron energy at quasi-parallel shocks. Recent observations at Saturn's bow shock with high Mach number (implying characteristics similar to those of astrophysical shocks such as supernova-driven shocks) show that quasi-parallel shocks are more efficient in generating relativistic electrons than quasi-perpendicular shocks [Masters et al., 2013]. This is inconsistent with what people believe from shock theory. Our study may also help explain this inconsistency, as foreshock transients, especially foreshock bubbles, could help accelerate parent shock-accelerated electrons to relativistic energies through betatron acceleration [Liu et al., 2018 in preparation].

D.3 Future work

Although foreshock transients are very promising to help understand shock acceleration, further investigation of them is needed. Although we have revealed several foreshock-transient-related acceleration mechanisms from case studies, these mechanisms cannot cover all events. For example, the electron Fermi process in Liu et al. [2017c] ignored the background field, limiting the number of events we could explain. By including the background field, we will generalize our Fermi model and discover the model's observational characteristics, including leakage. In addition, we will apply statistical studies to investigate conditions that favor occurrence of identified acceleration mechanisms. For example, for ions to gain energy by bouncing between the bow shock and the boundary of foreshock transients, the foreshock transient boundary might need to be thick with strong magnetic field strength. Furthermore, our

statistical study shows that ion and electron acceleration by foreshock transients is positively correlated with solar wind speed. How solar wind speed affects the acceleration process needs further study, however.

Our conclusions about foreshock transients are drawn from observations at Earth's bow shock. We need to generalize the role of foreshock transients in shock acceleration. Foreshock transients have been observed at other planets [e.g., Collinson et al., 2015; Valek et al., 2017]. Observations of other planets, such as Mercury, Mars, Jupiter and Saturn using the MESSENGER, MAVEN, Galileo and Cassini spacecraft, respectively, could help determine whether similar acceleration processes occur there. We can then compare our observations with our hybrid simulations under corresponding conditions. We can also apply hybrid simulations at high Mach number to further understand the role of foreshock transients at astrophysical shocks.

Although foreshock transients have been shown to be important, their properties are still not fully understood. For example, how foreshock ions interact with solar wind discontinuities to form foreshock bubbles and hot flow anomalies is still poorly explored. Case studies investigating ion distribution evolution and hybrid simulations using particle tracing could be applied to further understand that process. Hybrid simulations could also be applied to discover the difference between tangential discontinuity-driven foreshock bubbles and tangential discontinuity-driven hot flow anomalies by varying solar wind conditions and tangential discontinuity properties. Additionally, from 2021 to 2023, conjunction studies between Cluster, THEMIS, and MMS all in the dayside/upstream region will provide the first comprehensive measurements of foreshock and foreshock transients. In the future, foreshock bubble and hot flow anomaly formation based on solar wind observations/upstream conditions may be predicted, and these predictions may contribute to space weather forecasting and shock studies.

Appendices

a. Data and methods

To study foreshock transients, we apply data from NASA's THEMIS mission. Our database consists of measurements by THEMIS mission probes in 2007, and TH-B & TH-C in 2008 and 2009 [Angelopoulos, 2008]. In the first two dayside seasons of that mission [Sibeck and Angelopoulos, 2008], TH-B had an ~30 R_E apogee upstream on the dayside, and TH-C had a lower apogee, ~20 R_E. We analyzed plasma data from the THEMIS electrostatic analyzer (ESA) [McFadden et al., 2008] and its solid state telescope (SST) [Angelopoulos, 2008] and magnetic field data from its fluxgate magnetometer [Auster et al., 2008]. We also used ACE, Wind, and Geotail spacecraft to monitor the solar wind.

To calculate the normal direction of rotational discontinuities and tangential discontinuities, we apply the three-spacecraft timing method [Horbury et al., 2001]. With three spacecraft, there are two independent equations: $\Delta x_{1i} \cdot n_x + \Delta y_{1i} \cdot n_y + \Delta z_{1i} \cdot n_z = (V_x \cdot n_x + V_y \cdot n_y + V_z \cdot n_z) \cdot \Delta t_{1i}$ (i = 2, 3), where V_x, V_y, and V_z are the three components of solar wind velocity, and Δx_{1i}, Δy_{1i}, Δz_{1i} and Δt_{1i} are the separations along three spatial directions and the time delay, respectively, between spacecraft 1 and spacecraft i = 2, 3. Using the constraint: $n_x^2 + n_y^2 + n_z^2 = 1$, the normal direction can thus be obtained. For tangential discontinuities, the cross-product method can also be used to calculate the normal, $\boldsymbol{n} = \boldsymbol{B_u} \times \boldsymbol{B_d} / |\boldsymbol{B_u} \times \boldsymbol{B_d}|$, where $\boldsymbol{B_u}$ and $\boldsymbol{B_d}$ are the upstream and downstream magnetic field.

To calculate the normal of shocks, we apply the coplanarity method, either magnetic mode $\boldsymbol{n} = (\boldsymbol{B_u} \times \boldsymbol{B_d}) \times \Delta\boldsymbol{B} / |(\boldsymbol{B_u} \times \boldsymbol{B_d}) \times \Delta\boldsymbol{B}|$, where $\Delta\boldsymbol{B} = (\boldsymbol{B_u} - \boldsymbol{B_d})$, or mixed mode $\boldsymbol{n} =$

$(\Delta \boldsymbol{B} \times \Delta \boldsymbol{V}) \times \Delta \boldsymbol{B} / |(\Delta \boldsymbol{B} \times \Delta \boldsymbol{V}) \times \Delta \boldsymbol{B}|$, where $\Delta \boldsymbol{V}$ is the upstream and downstream flow velocity difference.

The minimum variance analysis (MVA) method can also be used to determine the normal direction when there is large magnetic field variation in the other two directions [Sonnerup and Scheible, 1998]. Because the magnetic field is divergenceless, the change in the normal component of the field at discontinuities or shocks is zero. However, for ideal 1-D shocks or discontinuities, the magnetic field varies only in one direction. In this case, the MVA method cannot be used. If there is wave activity at the shock ramp resulting in magnetic fluctuations in another direction, this method could be used, and we would require that the minimum-to-intermediate eigenvalue ratio be less than 0.1 (meaning that the minimum variance is 10% or less of the variance along the intermediate direction).

b. Test particle simulation

To further confirm our observational results, we also apply test particle simulations and hybrid simulations. In the test particle simulations, a certain number of electrons is put into the electromagnetic fields designed based on observations and advanced in time. The electron equation of motion is $\frac{\mathrm{d}\mathbf{p}}{\mathrm{d}t} = -e(\mathbf{E} + \mathbf{v} \times \mathbf{B})$, where $\mathbf{v}$ is the electron velocity, $\mathbf{p} = \gamma m \mathbf{v}$ is the electron momentum, the relativistic factor is $\gamma = 1/\sqrt{1 - (v/c)^2}$, and the electron kinetic energy is $E = (\gamma - 1)mc^2$ (the relativistic effect is included in the test particle simulations to properly follow the high energy electrons produced). To fully resolve electron gyromotions in the magnetic fields, the time step needs to be much smaller than the gyro-period in the strongest magnetic field.

c. Hybrid simulation

In hybrid simulations, electrons are described by fluid equations and ions are advanced by the equation of particle motion. In addition to the particle ions, a cold, incompressible ion fluid is also included in the inner magnetosphere to represent the plasmasphere. The electric field is calculated from the electron momentum equation in which the electron flow velocity is derived from Ampere's Law. The magnetic field is advanced in time using Faraday's law. Quasi-neutrality is assumed in the simulation. A detailed description of this code can be found in Lin and Wang (2005)

Our simulation, which uses a spherical coordinate system (r, θ, ϕ), is carried out within a geocentric distance $4\ R_E < r < 25\ R_E$. The initial condition includes a dipole geomagnetic field at $r < 10\ R_E$ (plus a mirror dipole field) and the solar wind at $r > 10\ R_E$. A solar wind rotational discontinuity (RD) is imposed to generate foreshock transients. The magnetic field of the solar wind with the RD is described by $B_x = -B_n = -B_{\mathrm{IMF}} \cos\Delta\phi$, $B_y = -B_n \tan\phi$, $B_z = 0$, and $\phi = \Delta\phi \tanh[(x_{RD} - x)/w]$, where B_{IMF} is the magnitude of the interplanetary magnetic field (IMF), $B_n = B_{\mathrm{IMF}} \cos\Delta\phi$ is the normal component of the IMF, x_{RD} is the x position of the RD's center, V_{RD} is the RD's propagation speed, and w is the RD's initial half-width.

d. Event lists

Foreshock transients observed by multiple THEMIS spacecraft in 2007 are listed below [Liu et al., 2016b]:

Date	Available SC data	Description
2007-7-11/1738	cde	complicated evolution
2007-7-20/2319	cde	complicated evolution in the pristine solar wind

2007-7-27/1500	abcde	small FB? Sheath?
2007-8-03/0417	abcde	FB, but only TH-A observed the FB, bcde may at the start stage
2007-8-03/0537	abcde	two FBs?, only TH-A observed the FB, bcde sheath?
2007-8-03/0813	abcde	FB? bcde sheath
2007-8-08/1057	abcde	complicated evolution
2007-8-12/0434	abcd	FB? HFA? Two compressional boundaries?
2007-8-16/0124	abcd	small FB? Sheath?
2007-8-18/1845	abcd	small FB? Only TH-A observed the FB
2007-8-20/0642	abcd	FB? HFA? Two events? Two compressional boundaries?
2007-8-25/0142	abcde	complicated evolution, A in the sheath
2007-8-25/0154	abcde	complicated evolution, A in the sheath
2007-8-27/1923	abcde	HFA in the pristine solar wind, A observed the interaction between BS and HFA
2007-8-27/2027	abce	FB? HFA? Two compressional boundaries?
2007-8-27/2039	abce	FB only TH-A observed the event
2007-8-27/2057-2110	abce	Many outward moving sheath?
2007-8-27/2125	abce	HFA? A in the sheath
2007-8-28/0056	abce	very small HFA
2007-8-28/0131	abce	very small HFA
2007-8-28/0143	abce	FB? HFA? Two compressional boundaries?
2007-8-29/0714	abcde	small FB? Sheath?
2007-9-01/2123	be	HFA
2007-9-02/0438	abcde	HFA
2007-9-02/0545	abcde	HFA? FB? Two events? Two compressional boundaries?
2007-9-02/0817	abcde	HFA

2007-9-03/1250	bde	FB? Two events? Two compressional boundaries
2007-9-03/1316	bde	HFA
2007-9-03/1334	bde	HFA
2007-9-03/1339	bde	HFA? In the pristine solar wind
2007-9-07/0240	abc	HFA, a in the sheath
2007-9-07/0246	abc	HFA, a in the sheath
2007-9-07/0252	abc	HFA, a in the sheath
2007-9-07/1021	bc	HFA
2007-10-30/2207	ab	HFA

The 247 foreshock transients observed by TH-B and TH-C in 2008 and 2009 during fast survey mode and particle burst mode are listed as following [Liu et al., 2017a]:

TH-C

2008-06-21/00:03:20

2008-06-26/16:39:17

2008-06-26/18:23:37

2008-06-26/18:26:35

2008-06-26/18:50:26

2008-06-26/18:55:23

2008-06-26/19:27:15

2008-06-26/19:58:05

2008-06-26/20:02:06

2008-06-26/21:02:56

2008-06-26/21:12:30

2008-06-28/19:38:17

2008-06-28/19:40:49

2008-06-28/19:41:53

2008-06-28/20:33:40

2008-06-28/20:34:35

2008-06-28/20:36:22

2008-06-30/18:27:55

2008-06-30/18:28:18

2008-06-30/20:44:02

2008-06-30/21:45:11

2008-07-02/18:34:00

2008-07-04/18:42:25

2008-07-06/16:35:55

2008-07-08/16:29:06

2008-07-08/17:05:16

2008-07-08/17:14:08

2008-07-10/18:08:24

2008-07-14/12:53:34

2008-07-14/13:13:51

2008-07-14/13:14:46

2008-07-14/13:15:20

2008-07-14/13:15:39

2008-07-14/13:16:01

2008-07-14/14:01:23

2008-07-14/15:20:54

2008-07-14/17:24:07

2008-07-14/17:36:00

2008-07-14/20:03:17

2008-07-14/20:01:40

2008-07-14/21:19:23

2008-07-14/21:54:24

2008-07-14/21:55:51

2008-07-14/21:57:37

2008-07-14/22:28:23

2008-07-14/22:37:18

2008-07-14/23:00:21

2008-07-14/23:25:35

2008-07-16/18:13:13

2008-07-16/19:11:10

2008-07-16/22:00:00

2008-07-16/23:33:22

2008-07-18/16:47:30

2008-07-18/17:33:33

2008-07-18/17:39:12

2008-07-24/13:25:30

2008-07-24/16:04:12

2008-07-24/17:19:03

2008-07-24/18:05:47

2008-08-11/13:22:26

2008-08-11/18:30:00

2008-08-11/18:48:50

2008-08-11/19:22:58

2008-08-11/19:18:42

2008-08-11/22:30:23

2008-08-13/15:36:00

2008-08-13/19:11:08

2008-08-13/19:13:10

2008-08-13/19:50:20

2008-08-13/19:53:45

2008-08-13/21:10:50

2008-08-13/21:38:44

2008-08-13/22:21:26

2008-08-13/22:38:39

2008-08-13/23:15:24

2008-08-13/23:16:51

2008-08-13/23:17:52

2008-08-13/23:31:40

2008-08-15/16:52:10

2008-08-15/17:59:32

2008-08-19/13:23:50

2008-08-19/13:42:20

2008-08-19/19:10:00

2008-08-19/20:35:36

2008-08-19/20:43:24

2008-08-19/21:02:59

2008-08-19/21:46:02

2008-08-19/21:51:32

2008-08-19/22:07:55

2008-08-19/22:17:01

2008-08-19/22:30:34

2008-08-19/22:33:37

2008-08-19/22:34:45

2008-08-19/22:37:20

2008-08-19/22:40:43

2008-08-19/23:37:24

2008-08-21/19:57:45

2008-08-21/19:57:44

2008-08-21/20:24:54

2008-08-21/20:33:53

2008-08-21/20:59:12

2008-08-21/21:42:15

2008-08-21/21:50:13

2008-08-21/22:01:40

2008-08-21/22:20:04

2008-08-21/22:21:22

2008-08-21/23:23:59

2008-08-23/23:06:20

2008-08-25/13:20:12

2008-08-25/14:41:31

2008-08-25/20:45:02

2008-08-25/23:16:48

2008-08-25/23:21:45

2008-08-25/23:30:51

2008-08-25/23:34:03

2008-08-25/23:35:51

2008-08-27/17:59:23

2008-08-27/20:34:31

2008-08-27/21:04:06

2008-08-27/22:01:01

2008-09-02/20:35:40

2008-09-06/15:43:15

2008-09-06/19:41:04

2008-09-06/20:18:50

2008-09-06/20:24:10

2008-09-06/20:33:15

2008-09-06/21:45:30

2008-09-06/21:52:48

2008-09-08/14:26:38

2008-09-08/17:01:10

2008-09-08/17:23:16

2008-09-08/17:24:20

2008-09-08/18:43:35

2008-09-08/19:13:40

2008-09-08/19:59:24

2008-09-08/20:14:10

2008-09-08/20:16:02

2008-09-08/20:25:19

2008-09-08/20:26:35

2008-09-08/20:40:02

2008-09-10/13:23:30

2008-09-10/15:16:48

2008-09-10/15:23:39

2008-09-10/16:20:24

2008-09-10/16:26:10

2008-09-10/16:38:14

2008-09-10/17:40:12

2008-09-10/17:41:12

2008-09-10/18:16:02

2008-09-10/18:34:30

2008-09-10/18:35:03

2008-09-12/14:07:29

2008-09-12/14:22:00

2008-09-12/14:44:01

2008-09-12/14:46:12

2008-09-16/17:26:42

2008-09-16/17:46:13

2008-09-20/18:03:41

2008-09-24/14:09:16

2008-09-30/18:35:10

2008-10-03/16:13:38

2008-10-03/16:14:43

2008-10-03/16:16:01

2008-10-03/16:53:41

2008-10-04/13:05:13

2008-10-04/13:18:47

2008-10-04/14:28:27

2008-10-04/14:29:23

2008-10-04/14:30:10

2008-10-04/14:30:54

2008-10-04/14:32:43

2008-10-04/14:33:27

2008-10-04/14:40:21

2008-10-17/17:34:17

2008-10-20/11:43:38

2008-10-20/11:53:32

2008-10-20/14:07:20

2008-10-20/14:12:53

2008-10-20/14:30:13

2008-10-26/11:59:56

2008-10-26/12:13:29

2008-10-29/18:45:41

2008-10-29/18:56:50

2008-10-29/19:38:08

2008-10-30/08:47:52

2008-10-30/09:40:00

2008-10-30/09:44:44

2008-10-30/10:35:50

2008-10-30/10:48:56

2008-10-30/11:31:35

2008-10-30/11:36:32

2008-10-30/11:34:40

2008-11-07/13:26:07

2008-11-07/13:57:35

2008-11-08/22:37:45

2008-11-08/22:46:34

2008-11-08/23:05:53

2008-11-08/23:02:27

2008-11-08/23:37:56

2008-11-08/23:32:49

2009-07-13/16:03:47

2009-07-13/16:05:57

2009-07-14/06:49:07

2009-08-08/18:25:50

2009-08-10/17:17:01

2009-08-10/17:18:00

2009-08-28/18:15:46

2009-08-28/18:18:54

2009-09-05/15:48:00

2009-09-05/15:48:59

2009-09-05/15:57:47

2009-09-05/16:09:49

2009-09-05/16:23:30

2009-09-05/16:47:38

TH-B

2008-06-16/16:12:45

2008-06-16/16:35:05

2008-06-16/16:38:22

2008-06-16/17:23:35

2008-06-16/18:20:10

2008-06-16/18:31:31

2008-06-16/19:39:04

2008-09-04/21:53:14

2008-09-08/16:58:50

2008-09-08/17:14:48

2008-09-08/20:14:55

2008-09-08/20:35:19

2008-09-08/21:20:25

2008-09-08/21:50:48

2008-09-08/21:53:24

2008-09-08/22:00:37

2008-09-08/22:02:25

2008-09-08/22:07:15

2008-09-08/22:13:51

2008-09-08/22:23:23

2008-09-16/17:27:46

2008-09-16/17:45:35

2008-09-20/20:27:10

2008-09-24/19:42:14

2008-10-03/18:15:25

2008-10-03/18:20:06

2008-10-03/18:44:05

2009-06-27/15:38:28

2009-06-27/15:39:17

2009-07-13/09:34:00

2009-07-13/09:39:08

2009-07-29/21:57:28

2009-08-06/18:17:06

References

Angelopoulos, V. (2008), The THEMIS mission, Space Sci. Rev., 141, 5-34, doi: 10.1007/s11214-008-9336-1

Archer, M. O., D. L. Turner, J. P. Eastwood, T. S. Horbury, and S. J. Schwartz (2014), The role of pressure gradients in driving sunward magnetosheath flows and magnetopause motion, J. Geophys. Res. Space Physics, 119, 8117–8125, doi:10.1002/2014JA020342.

Archer, M. O., D. L. Turner, J. P. Eastwood, S. J. Schwartz, and T. S. Horbury (2015), Global impacts of a Foreshock Bubble: Magnetosheath, magnetopause and ground-based observations, Planet. Space Sci., 106, 56-65, doi:10.1016/j.pss.2014.11.026

Auster, H. U., et al. (2008), The THEMIS fluxgate magnetometer, Space Sci. Rev., 141, 235–264, doi:10.1007/s11214-008-9365-9.

Blanco-Cano, X., P. Kajdič, N. Omidi, and C. T. Russell (2011), Foreshock cavitons for different interplanetary magnetic field geometries: Simulations and observations, J. Geophys. Res., 116, A09101, doi:10.1029/2010JA016413.

Blandford R., D. Eichler (1987), Particle acceleration at astrophysical shocks: A theory of cosmic ray origin, Physics Reports, 154, 1, 1-75, ISSN 0370-1573, doi:10.1016/0370-1573(87)90134-7.

Burgess D. (1987), Shock drift acceleration at low energies. J. Geophys. Res. 92, 1119–1130, doi:10.1029/JA092iA02p01119.

Burgess, D., E. Möbius, M. Scholer (2012), Ion acceleration at the Earth's bow shock. Space Sci. Rev. 173(1–4), 5–47. doi:10.1007/s11214-012-9901-5

Chu, C., Zhang, H., Sibeck, D., Otto, A., Zong, Q., Omidi, N., McFadden, J. P., Fruehauff, D. and Angelopoulos, V. (2017), THEMIS Satellite Observations of Hot Flow Anomalies at Earth's Bow Shock, Annales Geophysicae, 35, 3, 443-451, doi: 10.5194/angeo-35-443-2017.

Collinson, G., et al. (2015), A hot flow anomaly at Mars, Geo-phys. Res. Lett., 42, 9121–9127,doi:10.1002/2015GL065079.

Drury L.O. (1983), An introduction to the theory of diffusive shock acceleration of energetic particles in tenuous plasmas. Rep. Prog. Phys. 46, 973–1027

Eastwood, J. P., E. A. Lucek, C. Mazelle, K. Meziane, Y. Narita, J. Pickett, and R. A. Treumann (2005), The Foreshock, Space. Sci. Rev., 118, 41–94, doi:10.1007/s11214-005-3824-3.

Facskó, G., Z. Németh, G. Erdős, A. Kis, and I. Dandouras (2009), A global study of hot flow anomalies using Cluster multi-spacecraft measurements, Ann. Geophys., 27, 2057–2076, doi:10.5194/angeo-27-2057-2009.

Forman M.A. and G.E.Morfill (1979), Time-dependent acceleration of solar wind plasma to MeV energies at corotating interplanetary shocks, in International Cosmic Ray Conference, vol. 5, p. 328

Fitzenreiter, R. J. (1995), The electron foreshock, Adv. Space Res., 15(8/9), (8/9)9 – (8/9)27.

Frey, S., Angelopoulos, V., Bester, M. et al. (2008), Orbit Design for the THEMIS Mission, Space Sci Rev, 141: 61., https://doi.org/10.1007/s11214-008-9441-1

Fuselier S.A. (1995), Ion distributions in the Earth's foreshock upstream from the bow shock. Adv. Space Res. 15, 43–52. doi:10.1016/0273-1177(94)00083-D

Gary, S. P. (1991), Electromagnetic ion/ion instabilities and their consequences in space plasmas: A review, Space Sci. Rev., 56, 373–415, doi:10.1007/BF00196632.

Gosling, J. T., Thomsen, M. F., Bame, S. J., Feldman, W. C., Paschmann, G. and Sckopke, N. (1982), Evidence for specularly reflected ions upstream from the quasi-parallel bow shock. Geophys. Res. Lett., 9: 1333–1336. doi:10.1029/GL009i012p01333

Helder, E. A., J. Vink, A.M. Bykov, Y. Ohira, J.C. Raymond, and R. Terrier (2012), Observational Signatures of Particle Acceleration in Supernova Remnants, Space Sci Rev, 173:369–431, DOI 10.1007/s11214-012-9919-8

Hess V.F. (1912), Über die Beobachtungen der durchdringenden Strahlung bei sieben Freiballonfahrten. Z. Phys. 13, 1084

Horbury, T. S., D. Burgess, M. Franz, and C. J. Owen (2001), Three spacecraft observations of solar wind discontinuities, Geophys. Res. Lett., 28, 677–680, doi:10.1029/2000GL000121

Jokipii J.R. (1987), Rate of energy gain and maximum energy in diffusive shock acceleration. Astrophys. J. 313, 842

Hudson, P. D. (1970), Discontinuities in an anisotropic plasma and their identification in the solar wind, Planet. Space Sci., 18, 1611–1622, doi:10.1016/0032-0633(70)90036-X.

Krymsky G.F. (1977), A regular mechanism for the acceleration of charged particles on the front of a shock wave. Dokl. Akad. Nauk SSSR 234, 1306,

Lee M. A., R.A. Mewaldt, J. Giacalone (2012), Shock Acceleration of Ions in the Heliosphere, Space Sci Rev, 173:247–281, DOI 10.1007/s11214-012-9932-y

Lin, Y., and X. Y. Wang (2005), Three-dimensional global hybrid simulation of dayside dynamics

associated with the quasi-parallel bow shock, J. Geophys. Res., 110, A12216, doi:10.1029/2005JA011243

Liu, Z., D. L. Turner, V. Angelopoulos, and N. Omidi (2015), THEMIS observations of tangential discontinuity-driven foreshock bubbles, Geophys. Res. Lett., 42, doi:10.1002/2015GL065842.

Liu, T. Z., H. Hietala, V. Angelopoulos, and D. L. Turner (2016a), Observations of a new foreshock region upstream of a foreshock bubble's shock, Geophys. Res. Lett., 43, doi:10.1002/2016GL068984.

Liu, T. Z., D. L. Turner, V. Angelopoulos, and N. Omidi (2016b), Multipoint observations of the structure and evolution of foreshock bubbles and their relation to hot flow anomalies, J. Geophys. Res. Space Physics, 121, doi:10.1002/2016JA022461.

Liu, T. Z., V. Angelopoulos, H. Hietala, and L. B. Wilson III (2017a), Statistical study of particle acceleration in the core of foreshock transients, J. Geophys. Res. Space Physics, 122, doi:10.1002/2017JA024043.

Liu, T. Z., V. Angelopoulos, and H. Hietala (2017b), Energetic ion leakage from foreshock transient cores, J. Geophys. Res. Space Physics, 122, doi:10.1002/2017JA024257.

Liu, T. Z., S. Lu, V. Angelopoulos, H. Hietala, and L. B. Wilson III (2017c), Fermi acceleration of electrons inside foreshock transient cores, J. Geophys. Res. Space Physics, 122, doi:10.1002/2017JA024480.

Liu, T. Z., Lu, S., Angelopoulos, V., Lin, Y., & Wang, X. Y. (2018). Ion acceleration inside foreshock transients. Journal of Geophysical Research: Space Physics, 123, 163–178.

https://doi.org/10.1002/2017JA024838

Liu, T. Z., Lu, S., Angelopoulos, V., Lin, Y., & Wang, X. Y. (2018). Ion acceleration inside foreshock transients. Journal of Geophysical Research: Space Physics, 123, 163–178. https://doi.org/10.1002/2017JA024838

Longair, M. S. (1981), High Energy Astrophysics (Cambridge: Cambridge University Press) Lust R 1955a 2. Naturf. 8a 277-84

Masters A., L. Stawarz, M. Fujimoto, S. J. Schwartz, N. Sergis, M. F. Thomsen, A. Retinò,H. Hasegawa, B. Zieger, G. R. Lewis, A. J. Coates, P. Canu, and M. K. Dougherty (2013), Electron acceleration to relativistic energies at a strong quasi-parallel shock wave, Nature Physics 9, 164–167, doi:10.1038/nphys2541

McFadden, J. P., C. W. Carlson, D. Larson, V. Angelopoulos, M. Ludlam, R. Abiad, B. Elliott, P. Turin, and M. Marckwordt (2008), The THEMIS ESA plasma instrument and in-flight calibration, Space Sci. Rev., 141, 277-302, doi:10.1007/s11214-008-9440-2.

Merka, J., A. Szabo, J. A. Slavin, and M. Peredo (2005), Three-dimensional position and shape of the bow shock and their variation with upstream Mach numbers and interplanetary magnetic field orientation, J. Geophys. Res., 110, A04202, doi:10.1029/2004JA010944.

Meziane K., R. P. Lin, G. K. Parks, D. E. Larson, S. D. Bale, G. M. Mason, J. R. Dwyer, and R. P. Lepping (1999), Evidence for acceleration of ions to ~ 1 Mev by adiabatic-like reflection at the quasi-perpendicular Earth's bow shock, Geophys. Res. Lett., 26, 2925–2928, doi:10.1029/1999GL900603.

Neugebauer, M., D. R. Clay, B. E. Goldstein, B. T. Tsurutani, and R. D. Zwickl (1984), A

reexamination of rotational and tangential discontinuities in the solar wind, J. Geophys. Res., 89(A7), 5395–5408, doi:10.1029/JA089iA07p05395.

Omidi, N., and D. G. Sibeck (2007), Formation of hot flow anomalies and solitary shocks, J. Geophys. Res., 112, A10203, doi:10.1029/2006JA011663.

Omidi, N., J. P. Eastwood, and D. G. Sibeck (2010), Foreshock bubbles and their global magnetospheric impacts, J. Geophys. Res., 115, A06204, doi:10.1029/2009JA014828.

Omidi, N., H. Zhang, D. Sibeck, and D. Turner (2013), Spontaneous hot flow anomalies at quasi-parallel shocks: 2. Hybrid simulations, J. Geophys. Res. Space Physics, 118, 173–180, doi: 10.1029/2012JA018099

Parker, E.N. (1965), The passage of energetic charged particles through interplanetary space. Planet. Space Sci. 13, 9

Raymond J.C., S. Krucker, R.P. Lin, V. Petrosian (2012), Observational aspects of particle acceleration in large solar flares. Space Sci. Rev. 173, 197–221. doi:10.1007/s11214-012-9897-x

Schwartz, S. J., C. P. Chaloner, P. J. Christiansen, A. J. Coates, D. S. Hall, D. Johnstones, M. P. Gough, A. J. Norris, R. P. Rijnbeek, D. J. Southwood and J. C. Woolliscroft (1985), An active current sheet in the solar wind, Nature, 318, 269-271, doi:10.1038/318269a0.

Schwartz, S. J., D. Burgess, W. P. Wilkinson, R. L. Kessel, M. Dunlop, and H. Luehr (1992), Observations of short large-amplitude magnetic structures at a quasi-parallel shock, J. Geophys. Res., 97, 4209–4227, doi:10.1029/91JA02581.

Schwartz, S. J. (1998), Shock and discontinuity normal, Mach numbers, and related parameters, from Analysis Methods for Multi-Spacecraft Data, edited by G. Paschmann and P. W. Daly, 249–

270.

Schwartz, S. J., G. Paschmann, N. Sckopke, T. M. Bauer, M. Dunlop, A. N. Fazakerley, and M. F. Thomsen (2000), Conditions for the formation of hot flow anomalies at Earth's bow shock, J. Geophys. Res., 105(A6), 12,639–12,650, doi:10.1029/1999JA000320.

Sibeck, D. G., et al. (1999), Comprehensive study of the magnetospheric response to a hot flow anomaly, J. Geophys. Res., 104(A3), 4577–4593, doi:10.1029/1998JA900021.

Sibeck, D. G., T. D. Phan, R. P. Lin, R. P. Lepping, and A. Szabo (2002), Wind 556 observations of foreshock cavities: A case study, J. Geophys. Res., 107, 1271, 557 doi:10.1029/2001JA007539.

Sibeck, D.G. and Angelopoulos, V. (2008), THEMIS science objectives and mission phases, Space Sci. Rev., doi: 10.1007/s11214-008-9393-5.

Smith, E. J., and M. E. Burton (1988), Shock analysis: Three useful new relations, J. Geophys. Res., 93(A4), 2730–2734, doi:10.1029/JA093iA04p02730.

Sonnerup B.U.Ö. (1969), Acceleration of particles reflected at a shock front. J. Geophys. Res. 74, 1301–1304. doi:10.1029/JA074i005p01301

Sonnerup, B. U. O., and M. Scheible (1998), Minimum and maximum variance analysis, in Analysis Methods for Multi-Spacecraft Data, ISSI Sci. Rep. SR-001, edited by G. Paschmann and P. W. Daly, pp. 185–220, Eur. Space Agency Publ. Dif., Noordwijk, Netherlands.

Thomsen, M. F., J. T. Gosling, S. J. Bame, K. B. Quest, C. T. Russell, and S. A. Fuselier (1988), On the origin of hot diamagnetic cavities near the Earth's bow shock, J. Geophys. Res., 93, 11311–11325, doi:10.1029/JA093iA10p11311

Treumann, R. A. (2009), Fundamentals of collisionless shocks for astrophysical application, 1. Non-relativistic shocks, Astron Astrophys Rev, 17:409–535, DOI 10.1007/s00159-009-0024-2

Turner, D. L., S. Eriksson, T. D. Phan, V. Angelopoulos, W. Tu, W. Liu, X. Li, W.-L. Teh, J. P. McFadden, and K.-H. Glassmeier (2011), Multispacecraft observations of a foreshock-induced magnetopause disturbance exhibiting distinct plasma flows and an intense density compression, J. Geophys. Res., 116, A04230, doi:10.1029/2010JA015668.

Turner D. L., N. Omidi, D. G. Sibeck, and V. Angelopoulos (2013), First observations of foreshock bubbles upstream of Earth's bow shock: Characteristics and comparisons to HFAs, J. Geophys. Res., VOL. 118, 1552–1570, doi:10.1002/jgra.50198.

Valek, P. W., et al. (2017), Hot flow anomaly observed at Jupiter's bow shock, Geophys. Res. Lett., 44, 8107–8112, doi:10.1002/2017GL073175

Vasquez, B. J., V. I. Abramenko, D. K. Haggerty, and C. W. Smith (2007), Numerous small magnetic field discontinuities of Bartels rotation 2286 and the potential role of Alfvénic turbulence, J. Geophys. Res., 112, A11102, doi:10.1029/2007JA012504.

Wang, S., Q.-G. Zong, and H. Zhang (2013), Hot flow anomaly formation and evolution: Cluster observations, J. Geophys. Res. Space Physics, 118, 4360–4380, doi:10.1002/jgra.50424.

Wilson, L. B. III, A. Koval, D. G. Sibeck, A. Szabo, C. A. Cattell, J. C. Kasper, B. A. Maruca, M. Pulupa, C. S. Salem, and M. Wilber (2013), Shocklets, SLAMS, and field-aligned ion beams in the terrestrial foreshock, J. Geophys. Res. Space Physics, 118, 957–966, doi:10.1029/2012JA018186.

Wilson, L. B. (2016). Low frequency waves at and upstream of collisionless shocks. Washington

DC American Geophysical Union Geophysical Monograph Series, 216, 269–291. https://doi.org/10.1002/9781119055006.ch16

Wilson, L. B. III, D. G. Sibeck, D. L. Turner, A. Osmane, D. Caprioli, and V. Angelopoulos (2016), Relativistic Electrons Produced by Foreshock Disturbances Observed Upstream of Earth's Bow Shock, Phys. Rev. Lett. 117, 215101, DOI: 10.1103/PhysRevLett.117.215101

Winske, D., and M. M. Leroy (1984), Diffuse ions produced by electromagnetic ion beam instabilities, J. Geophys. Res., 89, 2673–2688, doi:10.1029/JA089iA05p02673.

Zhang, H., D. G. Sibeck, Q.-G. Zong, S. P. Gary, J. P. McFadden, D. Larson, K.-H. Glassmeier, and V. Angelopoulos (2010), Time History of Events and Macroscale Interactions during Substorms observations of a series of hot flow anomaly events, J. Geophys. Res., 115, A12235, doi:10.1029/2009JA015180.

Zhang H., D. G. Sibeck, Q.-G. Zong, N. Omidi, D. Turner, and L. B. N. Clausen (2013), Spontaneous hot flow anomalies at quasi-parallel shocks: 1. Observations, J. Geophys. Res., VOL. 118, 3357–3363, doi:10.1002/jgra.50376